TESI DI DOTTORATO

UNIVERSITÀ DEGLI STUDI DI NAPOLI FEDERICO II

DIPARTIMENTO DI INGEGNERIA BIOMEDICA, ELETTRONICA
E DELLE TELECOMUNICAZIONI

DOTTORATO DI RICERCA IN
INGEGNERIA ELETTRONICA E DELLE TELECOMUNICAZIONI

Fractal Models for SAR Images

IVANA ZINNO

Il Coordinatore del Corso di Dottorato
Ch.mo Prof. Niccolò Rinaldi

Il Tutore
Ch.mo Prof. Daniele Riccio

ANNO ACCADEMICO 2010/2011

To my parents,
to whom I owe my way of thinking.

Contents

Introduction

The problem

Earth's observation and other Solar System's planets exploration are issues of great relevance nowadays, since matters as environmental study, natural disasters' prediction and monitoring, rational exploitation of natural resources become, day after day, more and more important.

Concerning these activities, microwave remote sensing is an excellent instrument as it allows a continuous and wide coverage monitoring, independent of climatic and light conditions, providing rapidly available data. Modern radars from satellites supply us with high-resolution images of the Earth; moreover, they are also unveiling details of other planets and moons in the solar systems that were never monitored before by any other remote sensing tool.

Hence, analysis of microwave images of natural areas is a topic of increasing interest, since the large amount of disposable SAR images does not find a counterpart of methods and applications for the relevant information extraction.

The scenario of new generation sensors suggests developing new techniques to analyze radar images of natural surfaces. As a matter of fact, by means of low-resolution images it was only possible to identify large scale features of an observed scene (e.g., presence of mountains and shape of reliefs); conversely, high-resolution images advise the possibility of extracting value added information of natural areas, presenting a much more precise physical meaning, thus providing physical-based information that cannot be trivially deduced from the input data. This task can be very useful for a wide range of applications, e.g. prevention and monitoring of environmental catastrophes [1], [2], geodynamic processes interpretation, land classification (extraction of geomorphologic features, land use etc.) [3], rural planning, and so on.

In this thesis the fundamental issue of recovering value added information from the analysis of single amplitude-only SAR images of natural scenes is dealt with; thus, the provided method is conceived

for supporting almost real-time applications in Earth monitoring and analysis from any interplanetary mission.
As the information can be properly defined only in the context of the application at issue, and a SAR image is essentially a representation of the local scattering properties of the scenario observed by the sensor, most of information is carried by the knowledge of electromagnetic theory and SAR operating manner.
In this work an analytical method for the estimation of surface roughness fractal parameters, based on the power spectral density behavior of SAR images along the range direction, is proposed [4]. Such a method uses both reliable electromagnetic-based scattering models and radar models to get the value added information from the SAR images.

Background

In the existing literature there is a general lack of algorithms allowing the estimation of meaningful geomorphologic parameters of natural surfaces from their radar image. This is due to the absence of a reliable direct model for microwave imaging of natural surfaces. A candidate direct model should originate automatic inverse procedures, that should not require supervision of a SAR expert. In addition the inverse procedure should be general-purpose, i.e. applicable to any type of SAR images, thus coping with the new generation of SAR sensors (e.g. Cosmo-SkyMed, TerraSAR-X) that exhibits extremely varied characteristics in terms of resolutions, configurations and operational modes (strip-map, spot-light, scansar); therefore, the available images can be each very different, making the information extraction procedure not immediate nor trivial.
The few existing approaches to the problem cannot be assumed reliable for a general-purpose application [5]. More specifically, most of the works published on the subject that propose a theoretical approach, suffer from an inadequate choice of the scattering functions used to describe the electromagnetic phenomenon and do not take into account the SAR filtering [6]-[9]. Alternatively, works adopting empirical approaches to retrieve significant parameters of the observed surface starting from the texture of the relevant radar image, do not found on a physical analytical model of SAR images to be used

for inversion purposes, thus leading these works to lose in generality and applicability, requiring supervision on behalf of an expert [10], [11].

Objectives

In this thesis both the *forward problem* and the *inverse problem* of modeling a SAR image via the imaged surface parameters and then extracting them from a single amplitude image, are dealt with.

The first main objective of this work is to provide, for natural surfaces, a radar imaging model, which is stochastic and analytical. As a matter of fact, the SAR image of any natural area can be seen as the image of an element of the ensemble (a particular realization) of the stochastic process describing the observed surface: this viewpoint is convenient because we are mainly interested in the knowledge of compact statistical parameters of a natural surface, i.e. the parameters of the stochastic process to which the surface belongs as an element of the ensemble, rather than in its complete deterministic behavior, which is specific of the particular realization of the stochastic process of interest. In other words, for many applications involving spatial scales not very large with respect to the image resolution, it is more interesting to know some compact parameters (dimensional numbers) describing the surface roughness (e.g., fractal dimension and topothesy, or standard deviation and correlation length) more than its deterministic point-by-point behavior (i.e., a function of two independent variables). To accomplish this task, it is necessary to evaluate the statistical characterization of the acquired image and relate it to that of the observed surface. In this thesis the second order statistics of the image are evaluated in closed form, thus providing the basis for the enforcement of inversion techniques, leading to the estimation of the surface parameters directly from the radar image.

A reliable radar image modeling requires appropriate descriptions for both the observed surface and the backscattered field. Fractal models are widely recognized as the best ones to qualitatively and quantitatively describe the geometry of natural surfaces with a minimum number of independent parameters [14]-[16]. In addition to these geometrical models, fractal scattering models have been developed in order to properly represent the interaction between the

electromagnetic signal and the fractal surface [17]-[19]. Therefore, a completely fractal approach for both geometrical and electromagnetic issues, is adopted in this thesis.
The second main goal consists in the implementation of a SAR image processing, able to work on a single amplitude SAR image in a completely automatic way, that generates maps of the point by point fractal parameters of the SAR image. The rational of the processing operation founds on the inversion of the developed theoretical model.
The obtained fractal maps are suitable for a wide range of applications and interpretations. Urban areas and man-made structures can be automatically distinguished from natural zones. Concerning the latter, fractal parameters allow, as an example, the interpretation and identification of geodynamic processes leading to the formation of volcanic complexes, rather than the separation between rocky formations holding different nature and so on. Moreover, the presented fractal processing can be used for change detection and classification purposes.

Organization of the thesis

In Chapter 1, fundamental concepts about SAR imaging are introduced. Firstly, SAR operating principles are described, in concise way, in order to supply the know-how about the SAR image formation. Then, significant properties of SAR images are introduced and an overall view of the existing sensors constellations is provided.
The second chapter is directed towards the introduction of fractals. The basic properties and parameters of fractal objects are firstly presented; then, the two fractal models used in this work for describing and synthesizing natural surfaces are discussed, respectively the fractional Brownian motion (fBm) and the Weierstrass-Mandelbrot (WM) function [14]-[16]. In particular the fBm model describes a natural surfaces via only two independent parameters strictly related to the surface roughness: the fractal dimension D and the increment standard deviation s [m^{D-2}].
In Section 3 the developed imaging model is presented. At first, the relation linking the SAR image to the radar reflectivity and to the electromagnetic backscattered field is investigated: the reflectivity, in the small slope regime for the surface, is linearly dependent only on

the ground range partial derivative of the surface. Hence, the evaluation of the analytical expression of the range derivative process is in order. Then, the power spectral densities of this topographic derivative process of two cuts of the surface directed respectively along azimuth and ground range directions are calculated in closed form. Then, exploiting the results obtained in the previous sections, the complete statistical characterization of the SAR image in terms of the surface fractal parameters is provided. In particular, it is shown that the power spectral density (PSD) of the ground range cut of the amplitude SAR image exhibits, in an appropriate range of spatial frequencies, a power law behavior [20], while that of the azimuth cut has a more involved expression. So the complete imaging model, absolutely general, independent of the specific choice for the scattering function is provided. Finally, the electromagnetic problem is faced introducing an appropriate scattering model, the fractal Small Perturbation Method (SPM), and evaluating the scattering coefficient of the SAR image PSDs in the SPM fractal case.

In Chapter 4 a complete experimental setup directed towards the validation of the theoretical framework presented in the previous section is presented. The fundamental issue is to compare the theoretically evaluated PSDs of a range and an azimuth cut of the SAR image of a natural surface with the corresponding PSDs estimated directly from a SAR image. To this aim, a completely fractal elaboration chain is worked out: a canonical fractal surface of controlled fractal parameters is generated to provide the input to a SAR simulator that generate the corresponding simulated SAR image [21]. Moreover, key considerations about the spectral estimation techniques are supplied.

In Chapter 5 the fractal parameters estimation from single SAR images is investigated. A large numerical setup regarding the fractal dimension estimation via linear regression techniques is performed. Then, preliminary results on the retrieving of the relative standard increment deviation are given, both from a theoretical and a numerical point of view. Finally, an algorithm providing the fractal dimension map of a single SAR image is presented. Also in this case a wide numerical setup, implemented using simulated SAR images for validation purposes, is provided.

The application of the presented fractal processing to actual (single-amplitude) SAR images is shown in Chapter 6. In particular, four

study cases are presented in order to give an idea of the different applications that can be carried out. The automatic separation of urban areas from rural ones - via fractal dimension estimation -is performed using a COSMO-SkyMed spotlight image of a zone in Abruzzo (Italy). Then a fractal dimension analysis of a volcanic area, provided also with the comparison with the ground truth, is presented concerning the Somma - Vesuvius volcanic complex (Campania, Italy) exploiting a TerraSAR-X stripmap image. Furthermore, a fractal-based analysis for the seismic damage estimation in urban areas is performed working on CosmoSky-Med spotlight pre and post earthquake images is shown. Finally, preliminary results on the application of the fractal processing for the relative standard increment deviation s [m^{1-H}] retrieving are shown making use of COSMO-SkyMed stripmap images of Burkina Faso (Africa).

References

[1] G. Di Martino, A. Iodice, D. Riccio, and G. Ruello, “A novel approach for disaster monitoring: fractal models and tools,” *IEEE Trans. Geosci. Remote Sens.*, vol. 45, no. 6, pp. 1559–1570, Jun. 2007.

[2] Voigt, S.; Kemper, T.; Riedlinger, T.; Kiefl, R.; Scholte, K.; Mehl, H.; , "Satellite Image Analysis for Disaster and Crisis-Management Support," *Geoscience and Remote Sensing, IEEE Transactions on* , vol.45, no.6, pp.1520-1528, June 2007.

[3] S. Aksoy, H. G. Akcay, and T. Wassenaar, “Automatic mapping of linear woody vegetation features in agricultural landscapes using very high resolution imagery,” *IEEE Trans. Geosci. Remote Sens.*, vol. 48, no. 1, pp. 511–522, Jan. 2010.

[4] G. Di Martino, D. Riccio and I. Zinno, "SAR Imaging of Fractal Surfaces", IEEE Trans. Geosci. Remote Sens., in print, available on IEEE Early Access.

[5] Campbell, B.A., "Scale-dependent surface roughness behavior and its impact on empirical models for radar backscatter", *IEEE Trans. Geosci. Remote Sens.*, 47, 3480-3488, Oct. 2009.

[6] A. Pentland, “Fractal-based description of natural scene,” *IEEE Trans. Pattern Anal. Mach. Intell.*, vol. PAMI-6, no. 6, pp. 661–674, Nov. 1984.

[7] P. Kube and A. Pentland, “On the imaging of fractal surfaces,” *IEEE Trans. Pattern Anal. Mach. Intell.*, vol. 10, no. 5, pp. 704–707, Sep. 1988.

[8] G. Korvin, “Is the optical image of a non-Lambertian fractal surface fractal?” *IEEE Geosci. Remote Sens. Lett.*, vol. 2, no. 4, pp. 380–383, Oct. 2005.

[9] L.M. Kaplan, “Extended Fractal Analysis for Texture Classification and Segmentation,” *IEEE Trans. Image Processing*, vol. 8, no. 11, pp. 1572-1585, Nov. 1999.

[10] P. Addesso, S. Marano, R. Restaino, and M. Tesauro, “Correlation properties of signals backscattered from fractal profiles,” *IEEE Trans. Geosci. Remote Sens.*, vol. 45, no. 9, pp. 2859–2868, Sep. 2007.

[11] Yen-Ching Chang; Shyang Chang; , "A fast estimation algorithm on the Hurst parameter of discrete-time fractional Brownian motion," *Signal Processing, IEEE Transactions on* , vol.50, no.3, pp.554-559, Mar 2002.

[12] W. Dierking, “Quantitative roughness characterization of geological surfaces and implications for radar signature analysis,” *IEEE Trans. Geosci. Remote Sens.*, vol. 37, no. 5, pp. 2397 - 2412, Sep. 1999.

[13] Pesquet-Popescu, B.; Vehel, J.L.; , "Stochastic fractal models for image processing," *IEEE Signal Processing Magazine*, vol.19, no.5, pp. 48- 62, Sep 2002.

[14] B.B. Mandelbrot, *The Fractal Geometry of Nature*. New York: Freeman, 1983.

[15] K. Falconer, *Fractal Geometry*. Chichester, U.K.: Wiley, 1989.

[16] J.S. Feder, *Fractals*. New York: Plenum, 1988.

[17] G. Franceschetti, A. Iodice, and D. Riccio, “Fractal models for scattering from natural surfaces,” in *Scattering*, R. Pike and P. Sabatier, Eds. London, U.K.: Academic, Sep. 2001, pp. 467–485.

[18] G. Franceschetti, D. Riccio, *Scattering, Natural Surfaces and Fractals*. Academic Press, Burlington (MA), USA, 2007.

[19] G. Franceschetti, A. Iodice, M. Migliaccio, D. Riccio, "Scattering from natural rough surfaces modeled by fractional Brownian motion two-dimensional processes", *IEEE Trans. Antennas Prop.*, vol. 47, no. 9, pp. 1405-1415, Sep. 1999.

[20] G. Di Martino, A. Iodice, D. Riccio, G. Ruello, "Imaging of Fractal Profiles", *IEEE Trans. Geosci. Remote Sens.*, vol. 48, no. 8, pp. 3280 - 3289, Aug. 2010.

[21] G. Franceschetti, M. Migliaccio, D. Riccio, G. Schirinzi, "SARAS: a SAR Raw Signal Simulator", *IEEE Trans. Geosci. Remote Sens.*, vol. 30, no. 1, pp. 110-123, Jan.1992.

Chapter 1

SAR images: fundamentals

SAR (Synthetic Aperture Radar) is essentially a complex system whose purpose is simply to measure the local interaction between the Earth's surface and an incident wave, thus providing very high quality SAR images of this interaction.
As a matter of fact, nowadays, a large amount of SAR images exhibiting the most various characteristics are available. Conversely, there is lack of methods and applications allowing precise and value added information extraction from these data.
According to the viewpoint, information can only be defined in the context of an application. Since the SAR image is simply a representation of the local scattering properties of the Earth scenarios, all the information is carried by our knowledge of electromagnetic theory. As such, the most basic description of information in SAR images may be considered to be in terms of solutions of Maxwell's equations for the propagation geometry and the scattering scene. However, both on theoretical and practical grounds, this viewpoint provides only a partial contribution to our understanding of the information available. From the point of view of electromagnetic theory, two approaches are relevant [2]. The first of these is the *Forward Problem*, in which the properties of the scattering medium and the incoming wave are specified and used to predict the scattered field. Solutions to this problem are currently available only by imposing considerable restrictions on the scattering medium, for example, by assuming that all length scales in the medium are large (or small) relative to the wavelength, or that only surface (not volume) scattering is occurring (or vice versa), or that occultation (shadowing) effects can be ignored. Nonetheless, progress in solving the *Forward Problem* has led to scattering models becoming increasingly important in SAR image interpretation [3]-[6].

Even within the context of electromagnetic theory, the Forward Problem is not the only issue when dealing with information in SAR images. Far more important is the *Inverse Problem*: what properties of an unknown scene can be inferred from the observed backscattered signal?

Methods to solve the *Inverse Problem* mathematically are, naturally, couched in terms of the same models as the *Forward Problem*, with all the same limitations, and are normally difficult. However, the real source of the difficulty in the Inverse Problem is not the mathematics but that there is rarely enough information to provide a unique solution. In other words, the number of parameters needed to characterize the target in the scattering model exceeds the number of independent measurements available at the sensor.

The approaches that describe information in SAR images through electromagnetic theory have the apparent advantage that they map the observed signal onto physical properties of the scene, such as dielectric constant, geometrical factors (e.g., size, height, and roughness), and polarization. In doing so, they provide a link between observations and measurable quantities on the ground.

In this chapter the fundamental concepts concerning SAR images are introduced. Being the problem definitely extensive, the main objective, in this context, is to provide a basic knowledge of the SAR operation and to supply an overall view of the problem of extracting information from SAR images. In Section 1.1, the physical principles of SAR image formation and the quantities at stake when dealing with SAR images are introduced. In section 1.2 some significant phenomena regarding SAR images are described. Finally, in section 1.3 an overview of the existing SAR system is provided, showing the variety of imaging radar systems, and consequently of SAR images, currently available.

1.1 Principles of SAR image formation

The basic geometry of a SAR system is shown in Figure 1.1. A platform moving with velocity $\underline{v}$ at altitude h carries a side-looking radar antenna that illuminates the Earth's surface with pulses of

electromagnetic radiation. The direction of travel of the platform is known as the azimuth direction; distance from the radar track is measured in the range direction.

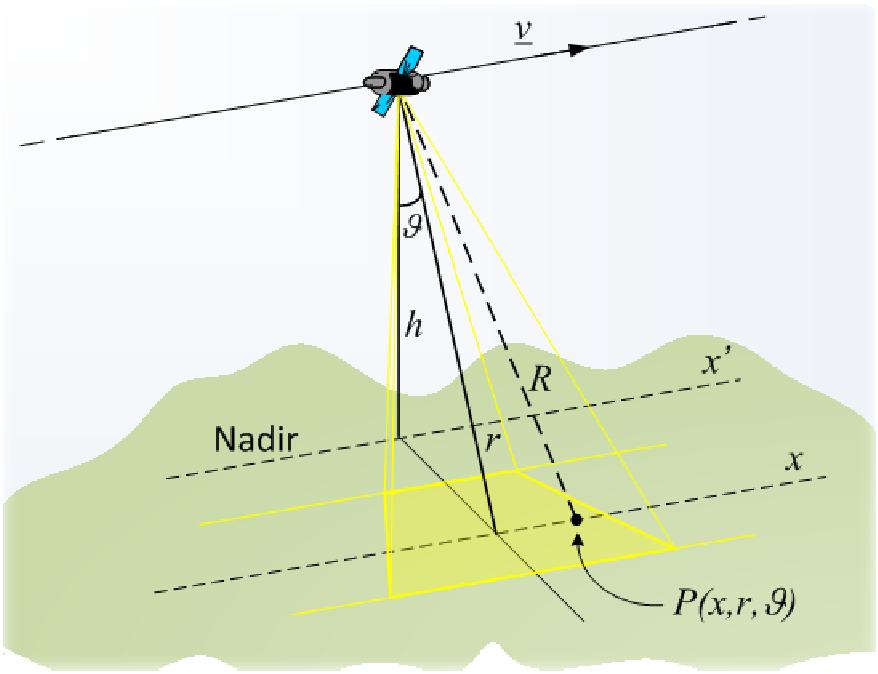

Fig. 1.1: Geometry of SAR acquisition system

The SAR system can work according to different operational modes of acquisition, among them, in this section, the stripmap configuration is considered. In this case, the antenna points along a fixed direction with respect to the platform flight path and its footprint defines an illuminated strip on the observed surface as the sensor moves [1].
The SAR raw signal can be evaluated as the superposition of the elementary returns from the illuminated surface weighted via its reflectivity function, $\gamma(\cdot)$:

$$h(x',r') = \iint dxdr\gamma(x,r)g(x'-x,r'-r;r) \qquad (1.1)$$

and the unit impulse response of the SAR system $g(\cdot)$, in the case of a stripmap acquisition mode and of a transmitted chirped pulse, can be expressed as:

$$g(x'-x,r'-r;r) = \exp\left[-j\frac{4\pi}{\lambda}\Delta R\right]\exp\left[-j\frac{4\pi}{\lambda}\frac{\Delta f/f}{c\tau}\times (r'-r-\Delta R)^2\right]w^2\left(\frac{x'-x}{X}\right)\mathrm{rect}\left[\frac{(r'-r-\Delta r)}{c\tau/2}\right] \quad (1.2)$$

where, referring to Fig. 1:

- P is the generic scattering point on the observed surface and its coordinates (x,r,θ) are given in a cylindrical reference system for which the azimuth direction coincides with the sensor flight path; $\theta(x,r)$ is the local incidence angle, which depends on the local geometry of the surface; R is the antenna-to-target distance and $\Delta R = R - r$;
- c is the speed of light, f and λ are respectively the carrier frequency and the corresponding wavelength, Δf is the chirp bandwidth and τ its duration time;
- $w(\cdot)$ is the antenna illumination function, $X = \lambda R_0/L_x$ is the real antenna azimuth footprint (we assume that $w(\cdot)$ is negligible when the absolute value of its argument is larger than 1/2, and that it is an even function), where L_x is the azimuth dimension of the real antenna and R_0 is the distance from the line of flight to the centre of the scene.

The evaluation of the Transfer Function of the SAR system is now in order. The Fourier Transform (FT) of Eq. (1.1) can be expressed as [1]:

$$H(\xi,\eta) = \iint \gamma(x,r)G(\xi,\eta,r)\exp[-j\xi x]\exp[-j\eta r]\,dxdr \quad (1.3)$$

where $G(\cdot)$ is the TF of the SAR system in the stripmap acquisition mode, given by the following FT:

$$G(\xi,\eta;r) = \iint g(x-x',r-r';r)\exp\left[-j\xi(x'-x)\right]\times \exp[-j\eta(r'-r)]\,dx'dr' \quad (1.4)$$

It is worth noting that, if the *r*-dependence in Eq. (1.4) can be neglected, Eq. (1.1) becomes a two-dimensional convolution, leading to the following simplified expression for Eq. (1.3):

$$H(\xi,\eta) = \iint \gamma(x,r)\exp(-j\xi x)\exp(-i\eta r)\,G(\xi,\eta)dxdr = \Gamma(\xi,\eta)G(\xi,\eta) \qquad (1.5)$$

The FT in Eq. (1.4) is susceptible of asymptotic evaluation by applying the stationary phase method because of the presence of the fast varying phase terms, thus leading to the following expression:

$$G(\xi,\eta,r) = \exp\left[j\frac{\eta^2}{4b}\right]\exp\left[j\frac{\xi^2\left(\frac{r}{R_0}\right)}{4a\left(1+\frac{\eta\lambda}{4\pi}\right)}\right]\times rect\left[\frac{\eta}{2bc\tau/2}\right]w^2\left(\frac{\xi}{2aX}\right) \qquad (1.6)$$

wherein

$$a = \frac{2\pi}{\lambda R_0} \qquad (1.7)$$

$$b = \frac{2\pi(\Delta f/f)}{\lambda c\tau} \qquad (1.8)$$

In order to provide the final SAR image, the raw signal must be elaborated. The main goal of the SAR processor is to adequately combine all the received backscattered contributions, which in the raw signal are spread out over all the extension $[X, c\tau/2]$, to achieve the best resolution.

The standard SAR processing, in the hypothesis that the *r*-dependence in Eq. (1.4) can be neglected, consists in a de-convolution performed on $h(x',r')$ to compensate for the convolution factor $g(x',r',r_0)$ and obtain an estimation of the reflectivity function. This operation can be

efficiently implemented in the Fourier domain by a simple multiplication:

$$\hat{\Gamma}(\xi,\eta) = \Gamma(\xi,\eta) \cdot \mathrm{G}(\xi,\eta) \cdot \mathrm{G}^{*}(\xi,\eta) \tag{1.9}$$

where * stands for the conjugation operator. Combining Eq. (1.9) with Eq. (1.6) in case of a space-invariant processing it turns out:

$$\hat{\gamma}(x',r') = \iint \gamma(x,r) \exp\left(-j\frac{4\pi}{\lambda}r\right) \mathrm{sinc}\left[\frac{\pi}{\Delta x}(x'-x)\right] \mathrm{sinc}\left[\frac{\pi}{\Delta r}(r'-r)\right] dx\, dr \tag{1.10}$$

where Δx and Δr are the geometrical resolution of the final image in azimuth – slant range, respectively, and are equal to:

$$\Delta x = \frac{L}{2} \tag{1.11}$$

$$\Delta r = \frac{c}{\Delta f} \tag{1.12}$$

Hence, the SAR image can be seen as a convolution between the reflectivity function and two sinc functions, one in the azimuth and one in the range direction, whose main lobes present a -3dB width equal to the geometric resolutions of the sensor as defined in Eq. (1.11) and Eq. (1.12), respectively. Moreover, this elaboration is easily performed in the Fourier domain: as a matter of fact, the availability of efficient FFT codes determines a strong decrease in the computational complexity with respect to the required convolution in the spatial domain.

The described space-invariant processing is called *narrow focusing*, it is a type of simplified focusing as it determines that only the centre of the scene is perfectly focused. To achieve optimum focusing performance (*wide focusing*), in the general space-variant case, the FT of the reflectivity function requires to be computed on a deformed grid. Efficient processing codes in the Fourier domain have been developed to assure wide focusing of the data. Further detailed

information concerning these algorithms are beyond the scope of this thesis but are widely discussed in the referred literature [1].
As regards this work, the key result is presented in Eq. (1.10) which clearly shows how the SAR image is essentially equal to a sinc-convolved version of the reflectivity.

1.2 Fundamental properties of SAR images

The basic quantity measured by a single-frequency single-polarization SAR at each pixel of the image is a pair of voltages in the in-phase and quadrature channels [2]. As seen in the previous section, these measured values represent the effects of the scene on the transmitted wave, but not in a direct way. First, the finite bandwidth of the system in both range and azimuth implies that measured values are weighted averages from a region determined by the point spread function of the SAR. Second, numerous weightings need to be applied in the processing to convert the measured voltages to "geophysical" units corresponding to the complex reflectivity, RCS, or backscattering coefficient of the scene. With these provisos, the measurements made by the SAR are fundamentally determined by electromagnetic scattering processes.
Among the methods that can be adopted for dealing with a SAR image, the approaches that describe SAR images information through electromagnetic theory have the apparent advantage that they map the observed signal onto physical properties of the scene, such as dielectric constant, geometrical factors (e.g., size, height, and roughness), and polarization. In doing so, they provide a link between observations and measurable quantities on the ground.
However, some intrinsic phenomena of SAR images, depending on electromagnetic and imaging questions, must be taken into account.
SAR images hold noiselike quality characteristics (typical of coherent imaging systems), known as *speckle*. (It must be stressed that speckle is noiselike, but it is not noise; it is a real electromagnetic measurement, which is exploited, for example, in SAR interferometry.)

In distributed targets we can think of each resolution cell as containing a number of discrete scatterers. As the wave interacts with the target, each scatterer contributes a backscattered wave with a phase and amplitude change, so the total returned modulation of the incident wave is:

$$Ae^{i\Phi} = \sum_{k=1}^{N} A_k e^{j\Phi_k} \tag{1.13}$$

This summation is over the number of scatterers illuminated by the beam. The individual scattering amplitudes A_k and phases Φ_k are unobservable because the individual scatterers are on much smaller scales than the resolution of the SAR, and there are normally many such scatterers per resolution cell.

An immediate conclusion from (1.13) is that the observed signal will be affected by interference effects as a consequence of the phase differences between scatterers. In fact, speckle can be understood as an interference phenomenon in which the principal source of the noiselike quality of the observed data is the distribution of the phase terms Φ_k. Hence scatterers at different parts of the resolution cell will contribute very different phases to the return (1.13) even if their scattering behavior is identical.

As a result, we can in practice think of the phase Φ_k as being uniformly distributed in $[-\pi, \pi]$ and independent of the amplitude A_k. The sum (1.13) then looks like a random walk in the complex plane, where each step of length A_k is in a completely random direction [7].

Another SAR images intrinsic phenomenon is that of the geometric distortion due to the range imaging mode. Up to now the *slant range* direction has been considered. In many applications regarding the land analysis, i.e. when dealing with SAR images of natural surfaces) it is convenient to deal with the *ground range* direction (see Fig. 1.1). It is obvious that a constant slant range resolution Δr does not correspond to a similarly constant ground range resolution, say Δy. The relation between the slant and ground range resolution depends on the incidence angle θ (the angle between the illumination direction and the normal to the illuminated object):

$$\Delta y = \frac{\Delta r}{\sin \theta} \tag{1.14}$$

According to the width relation between the incidence angle θ and the slope of the imaged surface, α, three types of geometric distortion can occur:

- *foreshortening*: $-\theta < \alpha < \theta$. It correspond to a dilatation or compression of the resolution cell (pixel) on the ground depending on the conditions $0 < \alpha < \theta$ or $-\theta < \alpha < 0$, respectively;
- *layover*: $\alpha \geq \theta$. It causes an inversion of the image geometry. In other words peaks of hills or mountains with a steep slope commute with their bases in the slant range, thus causing an extremely severe image distortion. A particular case is represented by the situation $\alpha = \theta$ corresponding to the compression of the area with this slope into a single pixel.
- *shadow*: $\alpha \leq \theta - \pi/2$. In this case the region does not produce any backscattered signal, and no significant contribution to the image is generated by these areas.

1.3 Systems and developments

Over the years a lots of systems have been built and operated by different nations. Each one presents different specifications in terms of resolutions and working frequencies. Consequently, a large amount of SAR data, holding various characteristics, is currently available. Table 1.1 shows some systems to give an impression of the variety.

TABLE 1.1
Some orbital and airborne SAR systems showing the variety of imaging radar systems

Shuttle missions	SIR-A	1981	40m × 40m	L
	SIR-B	1984	25m × 17m	L
	SIR-C	1994	10m × 30m	L, C, X
	X-SAR/SRTM	2000	25m × 25m	C, X
Satellite based	Lacrosse	1988	< 1m × 1m	X
	ERS-1	1991	26m × 28m	C
	J-ERS_1	1992	18m × 18m	L
	RADARSAT	1995	10m × 9m	C
	ENVISAT	2002	25m × 25m	C
	TerraSAR-X	2006	< 1m × 1m	X
	Radarsat II	2005	3m × 3m	C
	SAR-Lupe	2005	< 1m × 1m	X
	IGS-2b	2008	30cm ×30cm	X
Airborne SAR	DOSAR	1989	< 1m × 1m	S, C, X, Ka
	CARABAS II	1997	3m × 3m	VHF
	PAMIR	2003	10cm × 10cm	Ku
	Lynx	1999	10cm × 10cm	Ku
	MISAR	2003	0.5m ×0.5 m	Ka
	RAMSES	1994	10cm × 10cm	P, L,S, C, X; Ku, Ka, W
	MEMPHIS	1997	20cm × 20cm	Ka, W
	E-SAR	1994	1.5m × 1.5m	P,L,S,C,X

References

[1] G.Franceschetti and R.Lanari; Synthetic Aperture Radar Processing, CRC PRESS, New York, 1999.

[2] C. Oliver, S. Quegan, *Understanding Synthetic Aperture Radar Images*, Scitech Publishing Inc., Reileigh (USA), 2004

[3] Ulaby, F. T., R. K. Moore, and A. K. Fung, Microwave Remote Sensing: Active and Passive, Vol. 3, Norwood, MA: Artech House, 1986.

[4] Tsang, L., J. A. Kong, and R. T. Shin, Theory of Microwave Remote Sensing, New York: Wiley-Interscience, 1985.

[5] Fung A. K., Microwave Scattering and Emission Models and Their Applications, Norwood MA: Artech House, 1994.

[6] G. Franceschetti, D. Riccio, Scattering, *Natural Surfaces and Fractals*. Academic Press, Burlington (MA), USA, 2007

[7] Goodman, J. W, "Statistical Properties of Laser Speckle Patterns," Laser Speckle and Related Phenomena, J. C. Dainty (ed.), New York: Springer-Verlag, 1984, pp. 9-75

Chapter 2

Fractal models for natural surfaces

In this chapter the fundamentals of fractal geometry are presented. This is finalized to introduce quantities and symbols adopted in the thesis and to present main concepts and mathematical background relevant to model natural surfaces roughness.
The pioneer of the fractal geometry was the polish mathematician Benoit B. Mandelbrot (1924 - 2010) who, in the middle of the seventies, provided a mathematical instrument for adequately describing the complexity and the irregularity of natural objects [1]-[4].
The term *fractal* (from latin *fractus*, i.e. "fragmented") indicates a large category of objects having fractional geometric dimension.
The basic idea of the fractal conception, easily comprehensible from an intuitive point of view, is that of an object for which the same motif recurs on scale smaller and smaller. Hence, fractal geometry is invoked for sets that hold a detailed structure on any arbitrary scale, they are too irregular to be represented according to classical geometry, they hold some self-similarity or self affine properties, they are defined in very simple ways, often recursively, and hold a somehow defined fractal dimension larger than its topological one. These preliminary concepts are introduced and discussed in Section 2.1 and 2.2.
Concerning natural surfaces both stochastic and deterministic fractal description can be used. In section 2.3 and 2.4 the *fractional Brownian motion* (fBm) and the *Weierstrass Mandelbrot* (WM) function are respectively presented. The former is a regular stochastic process, the latter is a predictable process that allows us to model deterministic as well as random surfaces.
Section 2.5 provides a connection between fBm processes and WM functions, thus showing that, independently of the mathematical employed model, the fractal surface have a common rational.
Another strength point in favor fractal models is the parameters estimation. As a matter of fact, use of geometric models requires their

parameters evaluation; in spite of the fact that classical-parameters evaluation relies on simple techniques, the values estimated on natural surfaces suffer of ambiguity and are not stable. Conversely, in spite of the fact that fractal-parameters evaluation may rely on involved techniques, the values estimated on natural surfaces are stable and not ambiguous. This is a further point in favor of the fractal description, which seems to have a perfect match with nature.

2.1 Fractal dimension

A fundamental concept of the fractal geometry is the *Hausdorff-Besicovitch* (HB) *Dimension*, i.e the fractal dimension [1]-[5]. The definition of the fractal dimension is based on the concept of the *Hausdorff measure*. Let U be any nonempty subset of a n-dimensional Euclidean space, R^n: the diameter |U| of U is the greatest distance between two points belonging to U.
A countable (or finite) collection of sets $\{U_i\}$ covers a set F if $F \subset \bigcup_i U_i$; furthermore, $\{U_i\}$ is said to be a δ-cover of F, if $0 < |U_i| \leq \delta, \forall i$.
The *s-dimensional Hausdorff measure* $H^S(F)$ of F is defined as

$$H^s(F) = \lim_{\delta \to 0} H_\delta^s(F), \qquad \delta > 0, s > 0 \tag{2.1}$$

where

$$M_\delta^s(F) = \inf\left\{\sum_{i=1}^{\infty} |U_i|^s : \{U_i\} \text{è } una\ copertura\ fi\ F\right\} \tag{2.2}$$

and $\inf\{\cdot\}$ is the lower bound. The superscript s in Equation (2.2) is a symbol in $H_\delta^s$and an exponent in $|U_i|^s$.
It can be shown that the Hausdorff measure generalizes, within a multiplicative constant, the Lebesgue measure as used, for instance, to define the number of points (R^0), the length (R^1), the area (R^2), and the volume (R^3) of Euclidean sets in R^n for n = 0, 1, 2, and 3, respectively.

It is observed that the Hausdorff measure, as defined by means of the limit in Equation (2.1), diverges for s smaller than a certain threshold D, and equals zero for s greater than D. The critical value $s = D$ for which $H^s(F)$ changes from ∞ to 0 is defined as the HB *dimension* of F. In this thesis, the HB dimension of F is used as the *fractal dimension* for the surfaces under study.
the Hausdorff dimension D is not forced to be an integer number; if this is the case, $s = n$ is an integer and the Hausdorff measure generalizes, within a multiplicative constant, the Lebesgue measure. It appears that Euclidean dimensions are recovered when the Hausdorff measure coincides with integer values of D.
The subset F of R^n, with $n > 1$, is *fractal* if its fractal dimension D is greater than its topological dimension, defined as equal to $n - 1$.
Considering, for instance, the case $n = 3$, a surface in a three-dimensional space is fractal if its fractal dimension D is greater than 2 and smaller than 3.
For natural surfaces, the fractal dimension is directly related to the surface roughness in an intuitive way: an almost-smooth fractal surface has a fractal dimension slightly greater than 2, because is tends to flatten over a classically modeled surface; conversely, an extremely rough surface has a fractal dimension that approaches 3, because it tends to fill in a classical volume.
If the surface is represented via a mathematical function, then continuity is always verified, whereas derivability of such a mathematical fractal is never reached at any point and scale. In turn, the fractal dimension is a continuous parameter that quantifies the intermediate behavior held by any fractal surface between the two- and three-dimensional Euclidean limiting cases.

2.2 Scaling properties

Fractal sets exhibit some form of scale invariance to scaling transformations. The self-affine property quantifies such a scaling invariance, so that the surface roughness at different scales is related through a precise relationship [5], [6].
Self-affinity generalizes the self-similarity property.

Aset is *self-similar* if it is invariant with respect to any transformation in which all the coordinates are scaled by the same factor.
A set is *self-affine* if it is invariant with respect to any transformation in which the coordinates are scaled by factors that are in a prescribed relation; in such a case, the set fractal dimension is linked to the relation among the scaling factors.

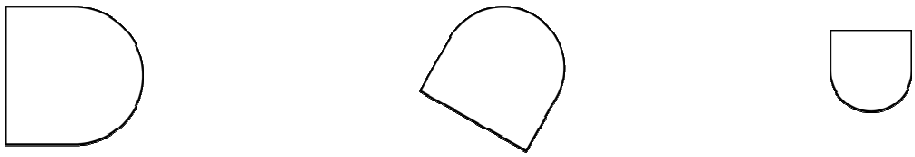

Fig. 2.1 Example of similarity transformations

Fig. 2.2 Example of affinity transformations

Self-similarity and self-affinity hold in the statistical sense if invariance to corresponding coordinates scaling holds for the statistical distribution used to describe the set.
The *s*-dimensional Hausdorff measure (*s* is not forced to be an integer for fractal sets) scales with a factor γ^s if coordinates are scaled by γ.
Note that the self-affine behavior is not sufficient to assess that a function can represent a fractal, because other smooth non-fractal functions may exhibit this property and are not fractals.
However, within some limitations, self-affinity may provide a rationale to conceive fractal sets and understand how they differ from the Euclidean ones.
Anyhow, whereas fractal sets hold their self-affinity at any arbitrary observation scale, natural surfaces hold this relevant property only within inner- and outer- characteristic scales. In other words, natural surfaces exhibit fractal characteristics only on a possibly wide but limited range of scale lengths; these scale lengths represent the surface range of fractalness. Sets that exhibit an infinite range of fractalness

are defined as *mathematical fractals*. Conversely, sets that exhibit a finite range of fractalness are defined as *physical fractals* [5].
In the following sections, it is shown how to define the spectral content of the fractal models. Observation scales correspond to surface-spectrum wavelengths: natural surfaces exhibit power-density spectra that are fractal only inside a finite bandwidth. This concept is further exploited if the *observable* natural surfaces are introduced—that is, if the description of the surface is related to a specific application.
Consider a surface to be explored: in particular, the height profile is of interest. Any actual instruments would sense, with a finite resolution, a limited length range of the observed surface. This can be equivalently stated assuming that the sensor is equipped with a band-pass filter: spatial scales and spectral bandwidth may be equally used to imply a finite exploration of the surface geometric properties. Each surface scale calls for a corresponding surface wave number; then range of fractalness calls for a corresponding fractalness bandwidth. It is concluded that a natural surface can be rigorously described by means of the corresponding mathematical fractal, provided that reference is made to range of scales, or bandwidth, within which the surface properties coincide with those of the mathematical fractal.

2.3 Fractal models for natural surfaces description

A natural surface can be represented by means of either a stochastic or a deterministic fractal set. The choice between these two very different representations relies on the applications to be made.
In this section a stochastic and a deterministic model for the natural surfaces description are presented: the *fractional Brownian motion* (fBm) process and the *Weierstrass-Mandelbrot* (WM) function, respectively.
The former is a regular stochastic process that provides an analytical expression of the probability density function of surface increments; the latter is a predictable stochastic process allowing the modeling of

both deterministic and stochastic surfaces and providing an analytical description of the surface.
Being the fBm a regular process, it is possible to reconstruct only the statistics of the fBm random process from one sample function. Conversely, the WM function is a predictable process, so that it is possible to predict an entire WM sample function from its knowledge on a domain subset.
These properties are fundamental for the selection of the analysis and synthesis procedures of natural surfaces: the former consist of estimation of the fractal parameters from fractal-surface realizations; the latter are related to generation of fractal surfaces with prescribed fractal parameters.

2.3.1 Fractional Brownian Motion process

The fBm process is defined in terms of the corresponding increment process. The stochastic process $z(x,y)$ describes an isotropic fBm surface if, for every x, y, x', y', all belonging to R, the increment process $z(x,y) - z(x',y')$ satisfies the following relation:

$$Pr\{z(x,y) - z(x',y') < \bar{\zeta}\} = \frac{1}{\sqrt{2\pi}s\tau^H}\int_{-\infty}^{\bar{\zeta}} exp\left(-\frac{\zeta^2}{2s^2\tau^{2H}}\right)d\zeta, \tag{2.3}$$

$$\tau = \sqrt{(x-x')^2 + (y-y')^2}$$

wherein H is the *Hurst coefficient* and s is the incremental standard deviation of surface, measured in [$m^{(1-H)}$], i.e. the standard deviation evaluated for increments at unitary distance.
In order to fully define an fBm process, the value of z at a given point should be specified: it is set $z(0) = 0$ so that the surface is self-affine. In the surface modeling and in the scattering problem, this condition is encompassed in the reference-system choice.
It can be demonstrated that a process satisfying Equation (2.3) exists if $0 < H < 1$, and that with probability 1, an fBm sample surface has a fractal dimension:

$$D = 3 - H \tag{2.4}$$

Inspection of Equation (2.3) shows that if $\tau \to 0$, then $z(x, y) - z(x', y') \to 0$, thus proving that any sample function z is continuous with respect to x and y.
The incremental standard deviation s is related to a characteristic length of the fBm surface, the *topothesy*, T:

$$s = T^{(1-H)} \tag{2.5}$$

The *topothesy* is the distance (measured in [m]) over which chords joining points on the surface have a surface-slope mean-square deviation equal to unity.
Then, as far as the number of parameters is concerned, the fBm process is a two-parameter regular random process. Definition of the fBm process has been done according to H and s in Equation (2.3). Other linked parameters, such as the fractal dimension D (see Equation (2.4)), can be used. The choice of the two independent parameters used to describe the process distribution is dictated by the use to be made of the stochastic process and by the mathematical- or physical-parameters interpretation.
Examples of fBm sample surfaces, and corresponding plots, are reported in the following discussion to show the influence of the fractal parameters on the surface appearance.
First, the effect of H is displayed by depicting in Figure 2.3, 2.4, 2.5 the fractal surfaces plots for values of H equal to 0.9, 0.55, 0.2 and setting $s = 0.01\ [\mathrm{m}^{1-H}]$. These graphs show that the higher the H, the smoother the surface appears, thus visually confirming (see Equation (2.4)) a direct relationship existing between the fractal dimension D and an intuitive concept of “roughness.”

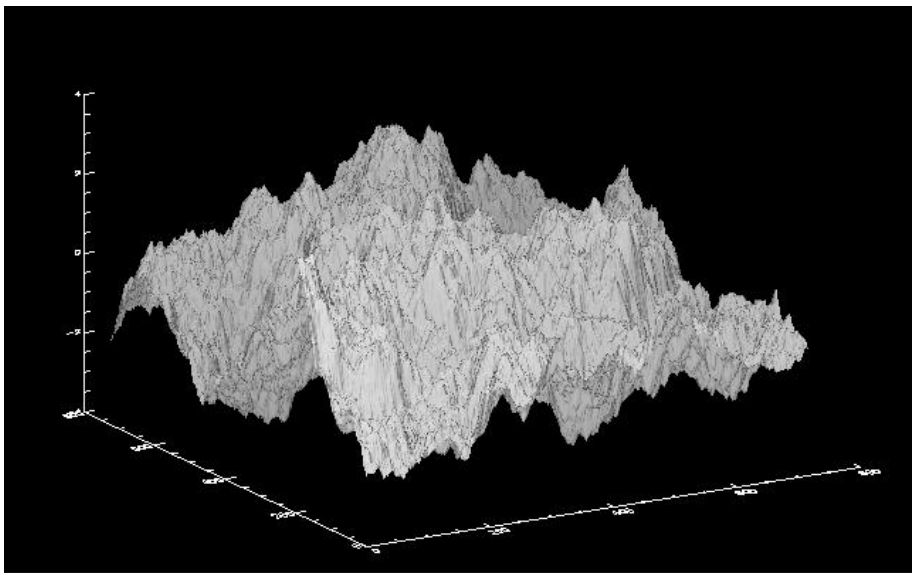

Fig. 2.3 Fractal surface with H=0.9, s=0.01[m$^{0.1}$]

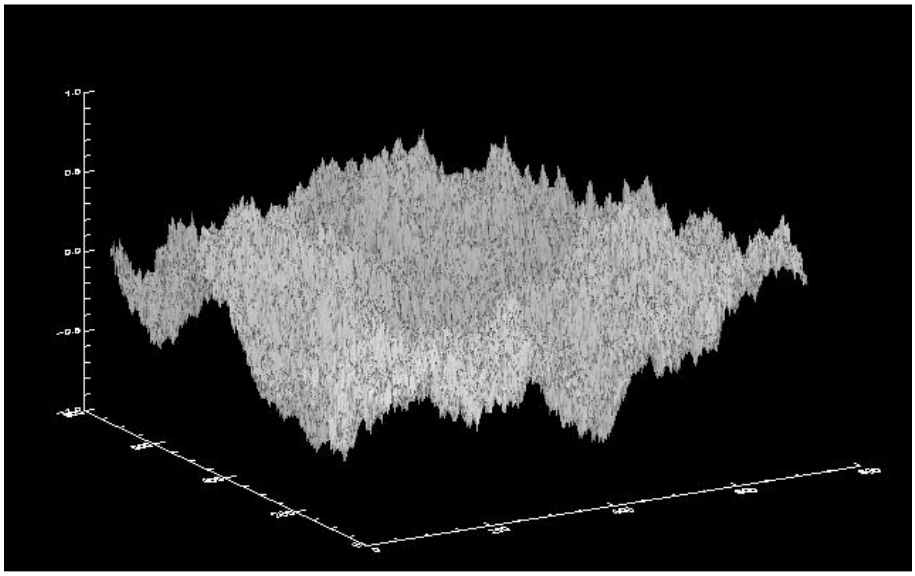

Fig. 2.4 Fractal surface with H=0.55, s=0.01[m$^{0.45}$]

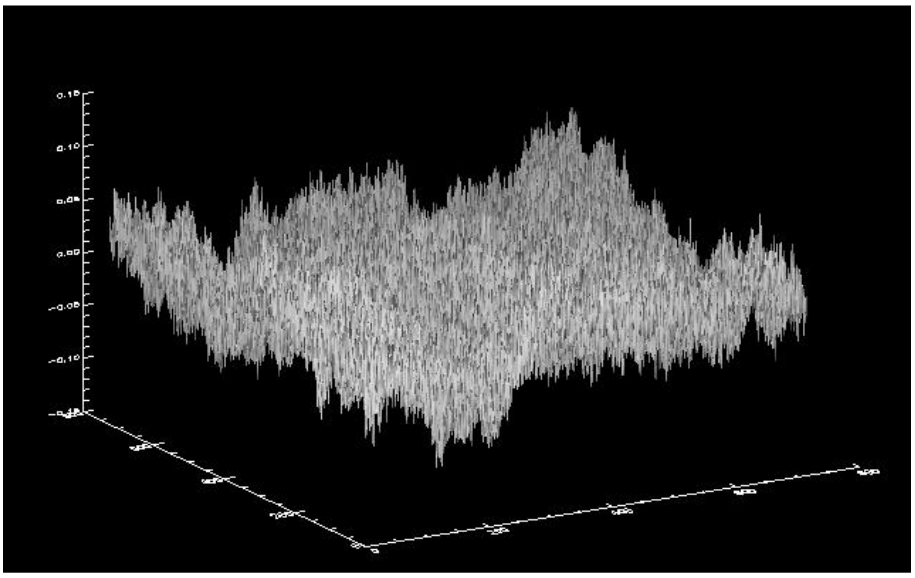

Fig. 2.5 Fractal surface with H=0.2, s=0.01[m$^{0.8}$]

The dual case is analyzed by changing s and leaving H fixed to a constant value. In Figure 2.6, 2.7, 2.8, the cases corresponding to s assuming values equal to 0.01, 0.1, 0.7 [m^{1-H}] and H=0.9 are depicted.

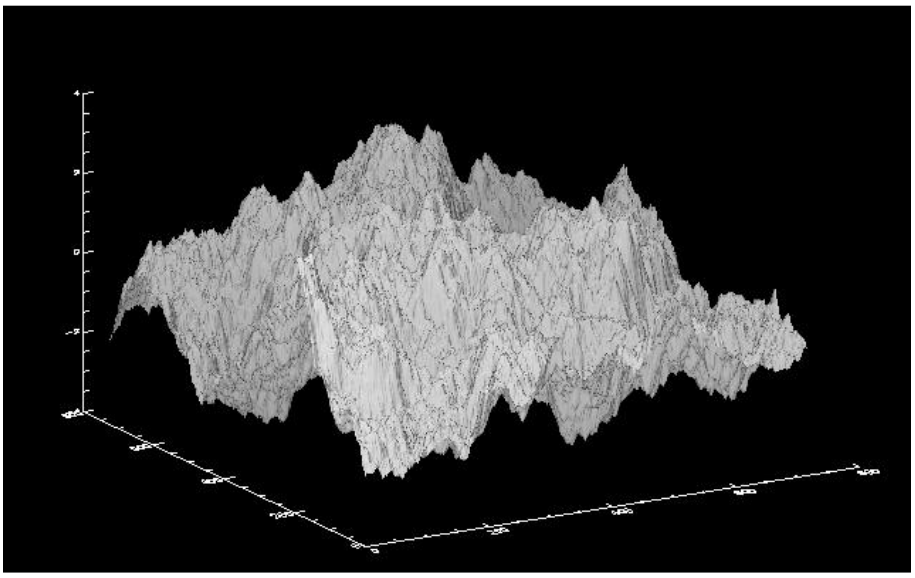

Fig. 2.6 Fractal surface with s=0.01[m$^{0.1}$], H=0.9

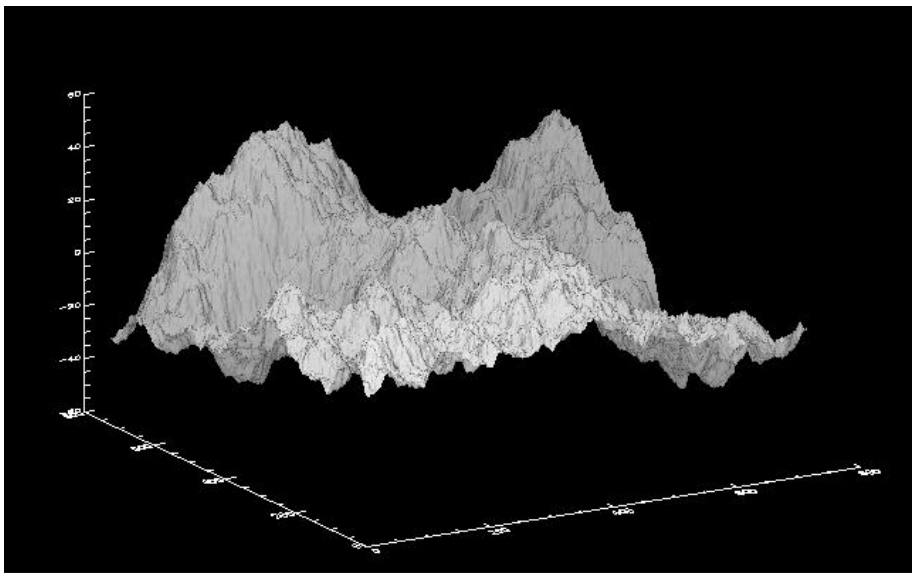

Fig. 2.7 Fractal surface with s=0.1[m$^{0.1}$], H=0.9

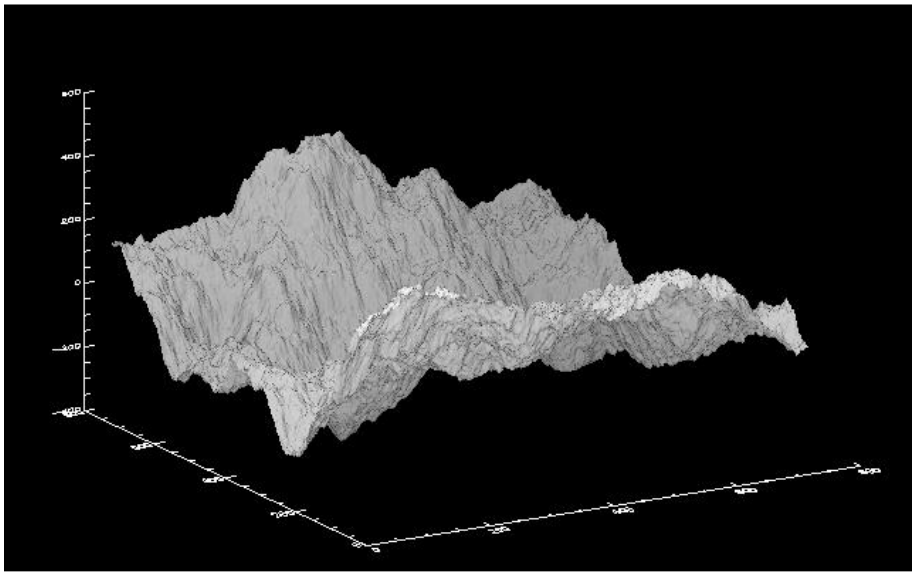

Fig. 2.7 Fractal surface with s=0.7[m$^{0.1}$], H=0.9

The pictures show that the higher s, the rougher the surface appears, thus visually confirming a relationship existing between the standard increment deviation s and an intuitive concept of "roughness." More

specifically, visual inspection of the figure shows that an increase of the topothesy corresponds to a scaling of the graphs along the vertical axis, thus equally affecting all the space undulations.
It can be demonstrated that the second-order characterization of the fBm surface is not complete [1], [2]. Conversely the fBm increments' pdf holds a gaussian behavior.

By definition, fBm surfaces have increments that are self-affine in the statistical sense. Letting $\mathbf{r} = x\hat{\mathbf{x}} + y\hat{\mathbf{y}}$, $\mathbf{r}' = x\hat{\mathbf{x}}' + y\hat{\mathbf{y}}'$, $\Delta z(\tau) = z(\boldsymbol{r}) - z(\boldsymbol{r}')$, it turns out:

$$\forall \gamma > 0, \qquad \Delta z(\gamma\tau) \doteq \gamma^H \Delta z(\tau) \tag{2.6}$$

where the symbol $\doteq$ means "exhibits the same statistics as."
The fBm is a stochastic process with wide-sense stationary increments, but the process itself do not hold the stationarity property. Taking into account that $z(0) = 0$, the autocorrelation of the fBm process is computed as follows:

$$\begin{aligned} R(\boldsymbol{r}, \boldsymbol{r}') &= \langle z(\boldsymbol{r}), z(\boldsymbol{r}') \rangle = \frac{1}{2}\langle z^2(\boldsymbol{r}) + z^2(\boldsymbol{r}') - [z(\boldsymbol{r}) - z(\boldsymbol{r}')]^2 \rangle \\ &= \frac{1}{2}\langle [z(\boldsymbol{r}) - z(0)]^2 + [z(\boldsymbol{r}') - z(0)]^2 - [z(\boldsymbol{r}) - z(\boldsymbol{r}')]^2 \rangle \\ &= \frac{T^{2(1-H)}}{2}(|r|^{2H} + |r'|^{2H} - |r' - r|^{2H}) \end{aligned} \tag{2.7}$$

because each quadratic factor has a Gaussian distribution, and its expected value coincides with its variance (see Equation (2.3)). Hence, the fBm process is nonstationary because its autocorrelation is not dependent only on the space lag $\boldsymbol{r} - \boldsymbol{r}'$ and particular attention must be paid in defining and evaluating its spectrum.
Conversely, according to Equation (2.3) the fBm process of the increments over a fixed horizontal distance τ is a stationary isotropic zero-mean Gaussian process:

$$\Delta z(\tau) \triangleq N(0, s^2\tau^{2H}) = N\left(0, T^{2(1-H)}\tau^{2H}\right) \tag{2.8}$$

Therefore, evaluation of the structure function $Q(\tau)$ of an fBm process is straightforward, because, according to the definition given in Chapter 2, the structure function coincides with the variance of the process increments:

$$Q(\tau) = s^2\tau^{2H} = T^{2(1-H)}\tau^{2H} \tag{2.9}$$

It can be shown that the power-density spectrum can be expressed in terms of the autocorrelation function as:

$$W(\boldsymbol{k}) = \int_{-\infty}^{\infty} d\boldsymbol{\tau}\, e^{-i\boldsymbol{k}\cdot\boldsymbol{\tau}} \left[\lim_{q\to\infty} \left(\frac{1}{2q}\right)^n rect\left(\frac{\boldsymbol{\tau}}{4q}\right) \int_{-\infty}^{\infty} R\left(\boldsymbol{r}+\frac{\tau}{2}, \boldsymbol{r}-\frac{\tau}{2}\right) rect\left(\frac{\boldsymbol{r}}{2q-|\boldsymbol{\tau}|}\right) d\boldsymbol{r} \right] \tag{2.10}$$

This equation holds for stationary as well as nonstationary stochastic processes.
Equation (2.10) can be simplified by considering the limit $q \to \infty$. The $\mathrm{rect}[\boldsymbol{\tau}/4q]$ states that each component of the variable $\boldsymbol{\tau}$ cannot exceed in module $2q$: when $q \to \infty$ it follows that $\mathrm{rect}[\boldsymbol{\tau}/4q] \to 1$. In addition, the $\mathrm{rect}[\boldsymbol{r}/(2q - |\boldsymbol{\tau}|)]$ can be asymptotically $(q \to \infty)$ replaced by $\mathrm{rect}[\boldsymbol{r}/2q]$: as a matter of fact, this implies to extend, for each component, the integration interval of $R(\cdot)$ of a length $|\boldsymbol{\tau}|$; being in that interval the autocorrelation limited, this extracontribution divided by $(2q)^n$ vanishes for $q \to \infty$.
In conclusion:

$$W(\boldsymbol{k}) = \int_{-\infty}^{\infty} d\boldsymbol{\tau}\, e^{-i\boldsymbol{k}\cdot\boldsymbol{\tau}} \left[\lim_{q\to\infty} \left(\frac{1}{2q}\right)^n \int_{-q}^{q} R\left(\boldsymbol{r}+\frac{\tau}{2}, \boldsymbol{r}-\frac{\tau}{2}\right) d\boldsymbol{r} \right] \tag{2.11}$$

Thus, the power spectrum can be expressed as follows:

$$W(\boldsymbol{k}) = \int_{-\infty}^{\infty} d\boldsymbol{\tau}\, e^{-i\boldsymbol{k}\cdot\boldsymbol{\tau}} \bar{R}(\boldsymbol{\tau}) \tag{2.12}$$

wherein $\bar{R}(\boldsymbol{\tau})$ is the autocorrelation function averaged over the spatial variable **r** (the term in square brackets in Equation (2.11)) .

Equations (2.11) and (2.12) are referred to as the Wiener-Khinchin theorem, referring to stationary as well as nonstationary processes. Substitution of Equation (2.7) in Equation (2.11) leads to:

$$W(\boldsymbol{k}) = \int_{-\infty}^{\infty} d\boldsymbol{\tau}\, e^{-i\boldsymbol{k}\cdot\boldsymbol{\tau}} \left[\lim_{q\to\infty} \left(\frac{1}{2q}\right)^{n} \frac{T^{2(1-H)}}{2} \int_{-q}^{q} \left(\left|\boldsymbol{r} + \frac{\boldsymbol{\tau}}{2}\right|^{2H} + \left|\boldsymbol{r} - \frac{\boldsymbol{\tau}}{2}\right|^{2H} - |\boldsymbol{\tau}|^{2H} \right) d\boldsymbol{r} \right] \tag{2.13}$$

Exchanging the integration limits, it turns out that:

$$W(\boldsymbol{k}) = \lim_{q\to\infty} \left(\frac{1}{2q}\right)^{n} \frac{T^{2(1-H)}}{2} \int_{-q}^{q} d\boldsymbol{r} \int_{-\infty}^{\infty} d\boldsymbol{\tau} \left(\left|\boldsymbol{r} + \frac{\boldsymbol{\tau}}{2}\right|^{2H} + \left|\boldsymbol{r} - \frac{\boldsymbol{\tau}}{2}\right|^{2H} - |\boldsymbol{\tau}|^{2H} \right) e^{-i\boldsymbol{k}\cdot\boldsymbol{\tau}} \tag{2.14}$$

Computation of the FT of τ^{2H} requires resorting to generalized FTs:

$$\int_{-\infty}^{\infty} |\boldsymbol{\tau}|^{2H} e^{-i\boldsymbol{k}\cdot\boldsymbol{\tau}} d\boldsymbol{\tau} = 2^{2+2H}\pi \frac{\Gamma(1+H)}{\Gamma(-H)} \frac{1}{k^{2+2H}} = -2^{2+2H}\Gamma^{2}(1+H) sen(\pi H) \frac{1}{k^{2+2H}} \tag{2.15}$$

Equation (2.15) exhibits a singularity in the origin. But, the generalized FT is intended to be used after multiplication by a function of an appropriate set (essentially a filter), thus rendering it of physical interest. Application of the multiplication and shift rules to this generalized two-dimensional FT provides:

$$\int_{-\infty}^{\infty} \left|\frac{\boldsymbol{\tau}}{2} \pm \boldsymbol{r}\right|^{2H} e^{-i\boldsymbol{k}\cdot\boldsymbol{\tau}} d\boldsymbol{\tau} = 2^{2} e^{\pm 2i\boldsymbol{k}\cdot\boldsymbol{r}} \int_{-\infty}^{\infty} |\tau|^{2H} e^{-i2\boldsymbol{k}\cdot\boldsymbol{\tau}} d\boldsymbol{\tau} = = -2^{2}\Gamma^{2}(1+H)\, sen(\pi H) \frac{1}{k^{2+2H}} e^{\pm 2i\boldsymbol{k}\cdot\boldsymbol{r}} \tag{2.16}$$

Substituting in Equation (2.14) it turns out:

$$W(\boldsymbol{k}) = \frac{T^{2(1-H)}}{2} 2^{2+2H}\Gamma^2(1 + H)sen(\pi H)\frac{1}{k^{2+2H}} \lim_{q\to\infty}\left(\frac{1}{2q}\right)^2 \int_{-q}^{q} d\boldsymbol{r}[1 - 2^{1-2H}\cos(2\boldsymbol{k}\cdot\boldsymbol{r})] \quad (2.17)$$

Evaluating the integral in Equation (2.17) leads to

$$W(\boldsymbol{k}) = \frac{T^{2(1-H)}}{2} 2^{2+2H}\Gamma^2(1 + H)sen(\pi H)\frac{1}{k^{2+2H}} \left[1 - 2^{1-2H} \lim_{q\to\infty}\left(\frac{1}{2q}\right)^2 \frac{sen(2qk_x)\, sen(2qk_y)}{k_x k_y}\right] \quad (2.18)$$

In the limit $q \to \infty$ the sinusoidal term in brackets vanishes, and the power-density spectrum of the two-dimensional fBm exhibits an appropriate power-law behavior [5], [7], [8]:

$$W(\boldsymbol{k}) = S_0 \boldsymbol{k}^{-\alpha} \quad (2.19)$$

characterized by two spectral parameters - the *spectral amplitude*, S_0 measured in $[\mathrm{m}^{2-2H}]$, and the *spectral slope*, α - that depend on the fractal parameters introduced in the space domain:

$$S_0 = 2^{2H+1}\Gamma^2(1 + H)sen(\pi H)T^{2(1-H)} = 2^{2H+1}\Gamma^2(1 + H)sen(\pi H)s^2 \quad (2.20)$$

$$\alpha = 2 + 2H = 8 - 2D \quad (2.21)$$

From the constraint on the Hurst exponent, $0 < H < 1$, it turns out that $2 < \alpha < 4$, which defines the range of allowed values for the spectral slope α. Equations (2.20) and (2.21) state the relation between fractal parameters in the spectral domain, S_0 and α, and their mates H (or D) and T (or s) in the space domain.

Only two fBm parameters are independent. These two independent parameters can be selected, according to the corresponding constraints, in the spatial domain or, alternatively, in the spectral

domain; each one of the introduced pairs of fractal parameters describes the surface roughness from a different viewpoint.

A surface satisfying Equation (2.3) for every τ is self-affine on all scales, so that it has details on any arbitrarily small scale: it is continuous, but not differentiable at any point.
This poses problems when using Maxwell differential equations or when considering a sensor monitoring the surface. For these reasons physical fBm surfaces must be introduced. This is possible because no actual natural surface holds property (2.3) at any scale, and some properties of fBm mathematical surfaces may be relaxed.
I has been stated that natural surfaces exhibit a fractal behavior only on a wide but limited range of scales.
Let us consider the limitation to the range of fractalness imposed by the sensor applied to monitor the surface. The range of scales of interest for a scattering problem is limited on one side by the finite linear size l of the illuminated surface, or by the sensor resolution if processing of the received signal is implemented; and on the other side by the fact that surface variations on scales much smaller than the incident wavelength λ do not affect the scattered field. In most cases—in particular in remote sensing of natural surfaces at microwave frequencies—these limitations due to the employed sensor fall between the limits of intrinsic validity for the surface-shape fractal model.
Accordingly, in electromagnetic scattering, *physical* fBm surfaces are considered; an efficient approach on surface modeling relies on considering surfaces that satisfy Equation (2.3) only for $\tau_m < \tau < \tau_M$ with τ_M of the order of l and τ_m usually taken of the order of $\lambda/10$. If $\tau_m \ll \tau_M$, then such surfaces satisfy Equation (3.25) only in a wide but limited range of spatial frequencies $k_m < \tau < k_M$, with $k_m \simeq 1/\tau_M$ and $k_M \simeq 1/\tau_m$.
That is why these surfaces are also referred to as *band-limited* fBm; they are stationary, at least in a wide sense, and regular.

2.3.2 Weierstrass-Mandelbrot Function

Among several possible representations of the WM function, the most suitable one for modeling natural surfaces is a real function of two

independent space variables x and y. A convenient choice is provided by the non-normalized WM function $z(x,y)$, amenable to represent deterministic as well as random surfaces [5], [9].
Consider the superposition of an infinite number of sinusoidal tones:

$$z(x,y) = B \sum_{p=-\infty}^{\infty} C_p \nu^{-Hp} sin\left[k_0 \nu^p \left(x\, cos\Psi_p + y\, sen\Psi_p\right) + \Phi_p\right] \tag{2.22}$$

wherein B [m] is the overall amplitude scaling factor; p is the tone index; $k_0[\mathrm{m}^{-1}]$ is the wavenumber of the fundamental component (corresponding to $p = 0$); $\nu > 1$ is the seed of the geometric progression that accounts for spectral separation of successive tones; $0 < H < 1$ is the Hurst exponent; and C_p, Ψ_p, Φ_p are deterministic or random coefficients that account for amplitude, direction, and phase of each tone, respectively.
Equation (2.22) exhibits a non-integer fractal dimension D as soon as ν is irrational, and the Hurst exponent is related to the fractal dimension $D = 3 - H$ as in Equation (2.4).
For random coefficients C_ps, the usual choice for their pdf is Gaussian with zero mean and unitary variance.
The coefficients Ψ_ps, in the random case, are uniformly distributed in $[-\pi, \pi)$ so that the WM function is isotropic in the statistical sense.
The random coefficients Φ_ps are usually chosen uniformly distributed in $[-\pi, \pi)$, and the *zero set* of the WM function – that is, the set of points of intersection with the plane $z = 0$ – is nondeterministic.
In the case of a random WM function, the random coefficients, C_p, Ψ_p, Φ_p, are usually assumed to be mutually independent.
The WM function holds the self-affine behavior only for the discrete values of $\gamma = \nu^n$ unless $\nu \to 1$: in this case, the WM function approaches the self-affine behavior for every scaling factor γ.
Physical WM functions can be obtained just limiting the summation to P tones, thus obtaining *band-limited* WM surfaces:

$$z(x,y) = B\sum_{p=0}^{P-1} C_p \nu^{-Hp} sin\left[k_0 \nu^p \left(x\, cos\Psi_p + y\, sen\Psi_p\right) + \Phi_p\right] \quad (2.23)$$

As in the case of fBm, use of band-limited WM surfaces is physically justified by the fact that surface fractality is held on a wide but limited range of scales, and any scattering measurement is limited to a finite set of scales. Let (X,Y) be the antenna footprint over the surface. The lowest spatial frequency of the surface, $k_0/2\pi$ is linked to the footprint diameter $\sqrt{X^2+Y^2}$, possibly through an appropriate safety factor $\chi_1 \in (0,1]$, whereas its upper spatial frequency $k_0\nu^{p-1}/2\pi$ is related to the electromagnetic wavelength λ through an appropriate safety factor $\chi_2 \in (0,1]$, usually set equal to 0.1. Accordingly, we can set:

$$k_m = k_0 = \frac{2\pi\chi_1}{\sqrt{X^2+Y^2}} \quad (2.24)$$

and

$$k_M = k_0 \nu^{(P-1)} = \frac{2\pi}{\chi_2 \lambda} \quad (2.25)$$

Definitions (2.24) and (2.25) can be combined to provide the number of tones, $P \in N$, in terms of the sensor wavelength and footprint:

$$P = \left\lceil \frac{\ln\left(\sqrt{X^2+Y^2}\,/\chi_1\chi_2\lambda\right)}{\ln\nu} \right\rceil + 1 \quad (2.26)$$

where $\lceil\cdot\rceil$ stands for the ceiling function, defined so as to take the upper integer of its argument.

It can be easily checked that the band-limited WM Surface (2.23) is stationary.

2.3.3 Connection between fBm and WM models

The connection between these two fractal models is appropriately found by comparing the spectral behavior of these two stochastic processes. The two representations cannot be equivalent in any respect because the independent parameters characterizing the fBm are two, for instance H and S_0, whereas in the WM, four independent parameters are considered, B, H, ν, H_0. However, it can be shown[5] that from the spectral point of view, the physical WM process is an appropriately sampled version of a band-limited fBm one.
The relation between Wm and fBm models' parameters is:

$$B^2 = \frac{S_0}{2\pi H} {k_0}^{-2H} (\nu^H - \nu^{-H}) \tag{2.27}$$

Whenever $\nu \to 1$, the spacing between successive tones of the WM functions tends to vanish, and the spectrum tends to become continuous, closely approximating that of the fBm process.
It is concluded that both an fBm and a WM model possesses the same Hurst parameter, and hence, at least in the limit $\nu \to 1$, hold a self-affine behavior and the same fractal dimension. Moreover, if B and k_0 are selected according to Equation (2.27), then the power content of the WM function and the equivalent fBm process are equal on appropriate spectral intervals; in the limit of $\nu \to 1$, this last result is valid on any spectral interval.
The established link between WM functions and corresponding fBm processes generates a handy procedure to realize samples of band-limited fBm processes by using physical WM functions. It is not trivial to obtain realizations of fBm ensemble functions characterized by H and S_0 parameters. The alternative, simpler way consists of evaluating, via Equation (2.27), the B parameter for a corresponding WM function, whose ensemble elements are certainly easier to evaluate via Equation (2.23). In this equation, the H value is equal to the Hurst coefficient of the fBm process, selection of the ν value states how closely the WM discrete spectrum represents the corresponding fBm continuous one, and selection of k_0 and P values are related to the process band limitation.

References

[1] B.B. Mandelbrot, The Fractal Geometry of Nature. New York: Freeman, 1983

[2] Falconer, K. Fractal Geometry. Chichester, England: JohnWiley, 1990

[3] Feder, J. S. 1988. Fractals. New York: Plenum Press.

[4] Turcotte D.L. 1997 - Fractals and Chaos in Geology and Geophysics (second edition) Cambridge University Press (pp:1-385)

[5] G. Franceschetti, D. Riccio, Scattering, *Natural Surfaces and Fractals*. Academic Press, Burlington (MA), USA, 2007

[6] B.B. Mandelbrot, *Gaussian Self-Affinity and Fractals*. Springer Verlag, New York, 2001.

[7] P. Flandrin, 1989, "On the spectrum of Fractional Brownian Motion". IEEE *Trans. Inform. Theory* 35, 197-199

[8] B. B. Mandelbrot, J. W. Van Ness, "Fractional Brownian motions, fractional noises and applications", *SIAM Rev.*, vol. 10, no. 4, pp. 422-437, Oct. 1968.

[9] Berry, M. V., and Z. V. Lewis. 1980. "On the Weierstrass-Mandelbrot Fractal Function." Proc R Soc London, Sect A 370:459–484.

Chapter 3

Imaging Model

In this chapter the overall imaging model that links a SAR image to the fractal parameters of the natural scene observed by the sensor is presented [1]. Consistently with the fractal stochastic description adopted for the remote sensed surface, the imaging process is expected to be a stochastic process and its second order stochastic characterization is evaluated as a function of the fractal parameters describing the surface. The analysis is performed both in the spatial domain and in the (spatial) frequency one. Indeed, as in following is discussed in details, in imaging theory (and in particular for a SAR sensor which is characterized by different spatial resolutions along azimuth and range), a meaningful role is played by the power density spectra of cuts (along azimuth and ground range) of the image that are here evaluated in closed form.

The complete SAR imaging model is obtained passing through sound radar, electromagnetic and geometrical models.

In Section 3.1 the SAR image autocorrelation is introduced showing its dependence on the reflectivity autocorrelation. Hence, in Section 3.2, the stochastic characterization of the reflectivity is evaluated, splitting the overall model in three fundamental steps: the analytical dependence of the reflectivity on the scene's topography, i.e. on the surface's slope(subsection 3.2.1); the evaluation of the fBm derivative process (subsection 3.2.2) and the stochastic characterization of the last one (subsection 3.2.3).

In section 3.3 the stochastic characterization of the SAR image, for an arbitrary scattering function adopted for describing the electromagnetic scattering from the surface, is presented.

Finally, in section 3.4, the application of the fractal *Small Perturbation Method* (SPM) – used for representing the electromagnetic interaction between the fractal surface and the

transmitted signal – to the previously obtained results is performed. Thus, the second order characterization of the SAR image of a fractal surface, in closed form, is obtained.

3.1 SAR image autocorrelation

The direct imaging model links the morphological features (topography at a wide range of scales) and the dielectric properties of a surface (inputs) to the relevant SAR image (output).
In this section the direct imaging model for a SAR sensor is presented. The overall model is split into two major elements. The first element links the SAR image to the scene reflectivity; the second element links the reflectivity to the scene parameters via a scattering model. In this section a continuous representation for the SAR image is assumed for the first part of the following analysis: this (formal) choice is done to emphasize the model behavior and to stress the meaning of the obtained results. Then, the sampled counterpart of actual (bandlimited) SAR images is discussed.
In order to attain an analytical direct model for the first element, a linear relationship is considered for the SAR image, *i*, that is a filtered version of the reflectivity function depending on the resolutions of the sensor (cf. Eq (1.10); hereafter, only for the sake of a more intuitive comprehension, the symbol $\hat{\gamma}$ that stands for the 'estimated reflectivity' is replaced by i, i.e. 'image'), [1], [2]:

$$i(x',r') = \iint \gamma(x,r)\mathrm{sinc}\left[\frac{\pi}{\Delta x}(x'-x)\right] \times \mathrm{sinc}\left[\frac{\pi}{\Delta r}(r'-r)\right] dxdr \qquad (3.1)$$

where *x* and *r*, as well as *x'* and *r'*, represent azimuth and slant-range, respectively; $\gamma(x,r)$ is the two-dimensional reflectivity pattern of the scene, and includes the phase factor $\exp(-j\frac{4\pi}{\lambda}r)$; λ is the electromagnetic wavelength, and Δx and Δr are the azimuth and slant-range SAR geometric resolutions, respectively.

Equation (3.1) is computed by employing the slant-range coordinate. It is convenient to reconsider it by means of its ground-range counterpart, *y*. Let us define the reflectivity map in the cylindrical coordinate system (*x ,r, θ*). Assuming that the local incidence angle coincides with the sensor look angle, θ_0, the ground range coordinate and the ground range resolution can be calculated by simple trigonometric computations: $y = r * \sin\theta_0$ and $\Delta y = \Delta r / \sin\theta_0$ (see Fig. 3.1 and Eq. (1.14)), [2].

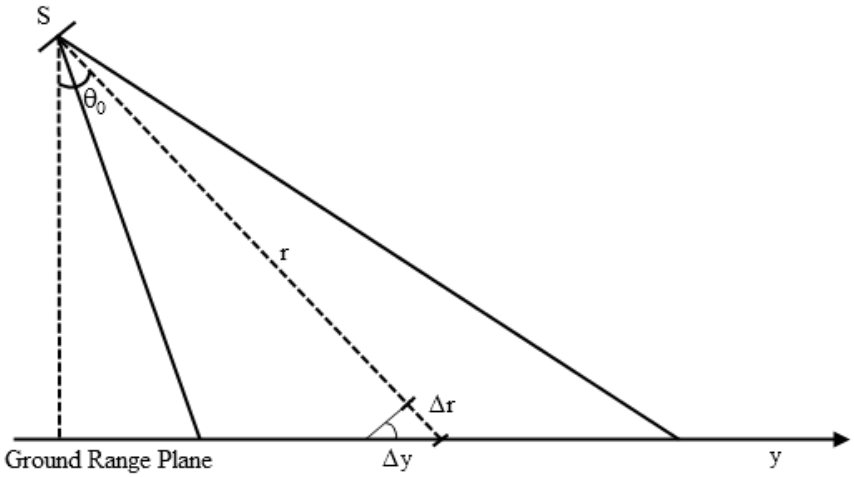

Fig.3.1: Slant range vs. ground range resolutions.

Hence, in order to provide the statistical characterization of the SAR image, it is convenient to rewrite the analytical link in terms of both the image and reflectivity autocorrelation functions [1]:

$$R_i(\tau_x', \tau_y') = \langle i(x', y') i^*(x' + \tau_x', y' + \tau_y') \rangle =$$
$$= \langle \frac{1}{\sin^2\theta_0} \iint \gamma\left(x, \frac{y}{\sin\theta_0}\right) \operatorname{sinc}\left[\frac{\pi}{\Delta x}(x' - x)\right]$$
$$\operatorname{sinc}\left[\frac{\pi}{\Delta y \sin^2\theta_0}(y' - y)\right] dx dy \iint \gamma^*\left(\bar{x}, \frac{\bar{y}}{\sin\theta_0}\right)$$
$$\operatorname{sinc}\left[\frac{\pi}{\Delta x}(x' + \tau_x' - \bar{x})\right] \operatorname{sinc}\left[\frac{\pi}{\Delta y \sin^2\theta_0}(y' + \tau_y' - \bar{y})\right] d\bar{x} d\bar{y} \rangle =$$
$$= \frac{1}{\sin^2\theta_0} \iint dx d\tau_x \iint dy d\tau_y \, R_\gamma\left(\tau_x, \frac{\tau_y}{\sin\theta_0}\right) \operatorname{sinc}\left[\frac{\pi}{\Delta x}(x' - x)\right]$$

$$\operatorname{sinc}\left[\frac{\pi}{\Delta x}(x' - x + \tau_x' - \tau_x)\right]\operatorname{sinc}\left[\frac{\pi(y' - y)}{\Delta y \sin^2\theta_0}\right] \operatorname{sinc}\left[\frac{\pi\left(y' - y + \tau_y' - \tau_y\right)}{\Delta y \sin^2\theta_0}\right]. \quad (3.2)$$

where the substitutions $\bar{x} = \tau_x + x$ and $\bar{y} = \tau_y + y$ have been considered and the stationarity of γ (that will be proved in the next section) has been supposed.
Assuming:

$$\int d\xi \operatorname{sinc}[a(\xi' - \xi)]\operatorname{sinc}\left[a\left(\xi' - \xi + \tau_\xi' - \tau_\xi\right)\right] = R_{sinc}\left[a(\tau_\xi - \tau_\xi')\right], \quad (3.3)$$

where, in order to obtain the expression at the second member, a substitution of variable has been performed. Hence we get:

$$R_i(\tau_x', \tau_y') = \frac{1}{\sin^2\theta_0}\iint d\tau_x\, d\tau_y\, R_\gamma\left(\tau_x, \frac{\tau_y}{\sin\theta_0}\right) R_{sinc}\left[\frac{\pi}{\Delta x}(\tau_x - \tau_x')\right] R_{sinc}\left[\frac{\pi}{\Delta y \sin^2\theta_0}(\tau_y - \tau_y')\right] \quad (3.4)$$

Equation (3.4) provides the link, expressed in azimuth/ground-range coordinates, between the autocorrelation of the SAR image and the autocorrelation of the continuous reflectivity function.
Some considerations are now in order:

- the image autocorrelation function is expressed by means of convolution integrals, so it is convenient to work in the wavenumber domain;
- in this way, since we demonstrate in the next section that the reflectivity is wide sense stationary, the Fourier transform of Eq. (3.4), which is the SAR image PSD, can be expressed as the reflectivity PSD (S_γ) multiplied by the Fourier transforms of R_{sinc};
- the Fourier transforms of R_{sinc} functions in Eq. (3.4) are rectangular functions that depend on the sensor resolutions: so we can directly consider a version of S_γ filtered by means of the aforementioned

rectangular functions (see Section 3.3).

3.2 Stochastic characterization of the reflectivity

In this section the evaluation of the stochastic characterization of the second element of the imaging model, the reflectivity pattern, is performed. The rationale of such an evaluation consists in three sound logical steps.
In subsection 3.2.1 the dependence of the reflectivity on the scene's topography is analyzed. This dependence is expressed through the local incidence angle, relating the reflectivity function to the slopes, and so equivalently to the partial derivatives, of the observed surface. Then, in subsection 3.2.2, the calculation of fBm ([3]-[5]) derivative process is performed, taking into account that the sensor operates a sort of "low-pass filtering" of the surface via the resolutions. Finally, in subsection 3.2.3 the closed form evaluation of the autocorrelation of the reflectivity process and of the Power Spectral Densities of cuts – along the range and azimuth directions – of the reflectivity of the SAR image are presented.

3.2.1 Dependence of the reflectivity on the scene's topography

The second element of the imaging model, the reflectivity pattern γ, taking into account the scattering mechanism relevant to the surface, deserves a specific comment. The rationale to get Eq. (3.1) is based on a linear model postulating superposition of radar returns (reflectivity) for each point of the surface. However, the scattering process is not a point-wise one; it could be seen as a point-wise phenomenon only under some very specific conditions, e.g., Geometrical Optics, whose approximations do not generally hold for microwave images. Actually, in SAR images the radar returns pertaining to the same resolution cell are merged as dictated by the SAR impulse response, whereas those from different resolution cells are separated. Therefore,

it is convenient to consider the contributions backscattered from different resolution cells as independent from each other, and the reflectivity pattern evaluation can be performed separately for each resolution cell.

Accordingly, the reflectivity pattern is expressed in terms of the Radar Cross Section (RCS) σ, as [2]:

$$|\gamma|^2 = \frac{\sigma}{\Delta x \Delta y} = \sigma^0, \tag{3.5}$$

wherein σ^0, the backscattering coefficient or Normalized Radar Cross Section (NRCS), represents the value of σ normalized to the SAR resolution area.

Whatever the electromagnetic model used to evaluate the backscattering coefficient is, some general results can be obtained. The backscattering coefficient expression is linked to the surface slope via the local incidence angle θ, i.e. the angle between the observation direction and the normal to the local mean plane approximating the considered surface within the resolution cell [3], [6]. Then:

$$|\gamma| = \sqrt{\sigma^0} = f(\theta(p, q)), \tag{3.6}$$

where the function f takes a different form depending on the selected solution to the scattering problem. Let q and p be the partial derivatives of the surface height $z(x, y)$ along the two directions elected by the SAR sensor, azimuth and ground-range, respectively x and y:

$$q(x, y) = \frac{\partial z(x, y)}{\partial x}, \tag{3.7}$$

$$p(x, y) = \frac{\partial z(x, y)}{\partial y}, \tag{3.8}$$

The local incidence angle can be formally expressed as a function of the partial derivatives p and q [1], in fact its cosine can be evaluated as the scalar product between the propagation unit vector and the surface normal unit vector, i.e.:

$$\theta = \cos^{-1}\left(\frac{p\ \sin\theta_0 + \cos\theta_0}{\sqrt{p^2+q^2+1}}\right). \tag{3.9}$$

In the hypothesis of a small slope regime for the surface, a McLaurin series expansion of the function $f(\theta(p,q))$ in Eq. (3.6) with respect to p and q can be performed: to the first order, we obtain a linear function of the partial derivative p only; as a matter of fact, from Eq. (3.9), it is clear that the derivative of θ with respect to q is proportional to q itself, implying that the linear term in q of the McLaurin expansion is zero.
Therefore, the modulus of the reflectivity function $|\gamma(x,y)|$, is, in a first order approximation, linearly linked only to the partial derivative p of the surface [1]:

$$|\gamma(x,y)| = f(\theta(p,q)) = a_0 + a_1 p(x,y) + o(p,q), \tag{3.10}$$

$$a_0 = f\big(\theta(p=0,q=0)\big) \quad a_1 = \left.\frac{\partial f(\theta(p,q))}{\partial p}\right|_{\substack{p=0\\q=0}}, \tag{3.11}$$

a_0 and a_1 being the coefficients of the McLaurin series expansion, whose expressions depend on the specific scattering model that is adopted. In particular, these coefficients are function of the look angle of the sensor, which is then an important parameter for the determination of the validity limits of the proposed linear model. Finally, we note that the obtained result highlights a key property of SAR - and, more in general, of side-looking radars - imaging behavior, showing a clear mathematical definition of a preferential imaging direction due to their particular acquisition geometry.
The result in Equation (3.10) is valid independently of the selected scattering function $f(\theta(p,q))$, hence it holds for whatever electromagnetic model (which can be evaluated analytically in closed form) is chosen and it presents reasonably a general validity, given the small slope regime for the observed surface. In Section 3.4, the coefficients of the McLaurin series expansion, a_0 and a_1 are evaluated in closed form for a specific scattering function, the fractal SPM one [3], [7], [8].

The above reported analysis can be assumed as a clear and valid foundation to assess the statistical characterization of the image. Usually, this characterization must be derived from a single amplitude SAR image and we cannot set aside the speckle phenomenon, the multiplicative noise affecting SAR images: for the sake of a theoretical analysis, we can consider the speckle as part of the reflectivity. As a matter of fact, radar single-look images hold small scale spatial properties (corresponding to high wavenumber spectral properties) dominated by the speckle effect. On the subject, some hints are provided in Chapter 5. Now a comment about the bandwidths of the reflectivity and of the SAR acquisition system is in order.
Due to the scattering mechanism, the reflectivity function holds a finite (spatial frequency) bandwidth: the minimum wavenumber being related to the (inverse of the) size of the illuminated area, the maximum one being related to the (inverse of the) electromagnetic wavelength. Due to the role played by the SAR system, the SAR image holds a different but still finite bandwidth: the minimum wavenumber being related to the (inverse of the) size of the considered area, the maximum one being related to the (inverse of the) SAR resolution. Therefore, the image autocorrelation function depends on the SAR resolutions: the analytical relationship between the reflectivity function (sampled according to SAR resolutions) and the parameters of the observed surface is explored. Hence, it is necessary to work with a two scale model for the surface description: the observed surface is locally approximated by square plane facets with dimension equal to that of the resolution cells; over these plane facets a microscopic roughness is superimposed so that the electromagnetic field backscattered from each resolution cell can be evaluated. Hence, the individual returns from each resolution cell are dictated by the microscopic scale (below resolution cell) roughness, while the overall image texture is related to the macroscopic scale (above resolution cell) roughness.

3.2.2 The fBm derivative process

In the previous section it has been shown that the stochastic characterization of the SAR image reflectivity involves use of the partial derivatives of the sensed surface.

As widely discussed in chapter 2, that fractal geometry is the best candidate to describe the irregularity and the roughness of natural scenes. Among the introduced fractal models, in order to describe the natural surfaces observed by the sensor, the regular stochastic fBm process is used [cf. Section 2.3.1].

In Section 2.3.1, the power spectral density (PSD) of the two-dimensional fBm process has been given in Eq. (2.19), (2.20), (2.21). In this section, since for the SAR image the spectrum evaluation is performed on one-dimensional cuts − thus highlighting the different spectral behaviors in azimuth and range directions – the power spectral density of a one-dimensional fBm profile is also shown.

An arbitrary one-dimensional cut of an isotropic fBm surface leads to an fBm profile described by the corresponding one-dimensional fBm process holding the same fractal parameters H and s.

The PSD of a topographic one-dimensional fBm profile is then introduced [9]:

$$W(k) = S_0' k^{-\alpha'}, \tag{3.12}$$

wherein k is the wavenumber and S_0' and α' are the spectral parameters in the one-dimensional case:

$$S_0' = \frac{\pi H}{\cos(\pi H)} \frac{1}{\Gamma(1-2H)} s^2, \tag{3.13}$$

$$\alpha' = 1 + 2H = 5 - 2D. \tag{3.14}$$

Note that the spectra of natural surfaces present a power-law behavior over a wide range of spatial scales [10]-[12].

The formal derivative of an fBm profile is defined as fractional Gaussian noise (fGn) [8], [9], and its power spectral density is proportional to that of the fBm profile multiplied by k^2 [13], [14]:

$$W_{fGn}(k) \propto \frac{1}{|k|^{2H-1}} \tag{3.15}$$

However, SAR images present a finite spatial extent and are discretized according to a non-zero lag sampling. Hence, application

to SAR images requires the definition of bandlimited stochastic processes, whose analytical form depends on the specific bandlimiting procedure applied. In order to get a closed form expression for the SAR image power spectrum, it is mandatory to consider the role of the resolution cell; this is convenient also because it allows working with a two-scale model for the surface. In this context, we want to study the canonical case of a fractal surface, with the same fractal parameters, at all the scales of interest for the sensor. In fact, a SAR sensor discriminates between scales lower and greater than the resolution cell size. Therefore, in our case the surface description within the resolution cell is introduced as a microscopic fractal roughness superimposed to a plane facet (having the dimension of the resolution cell) approximating the scene of interest; the macroscopic surface description at the resolution cell scale, which is related to the applied bandlimiting procedure, is then required in order to evaluate the PSD of interest.

Actually, to cope with the non-differentiability of the fBm process, a smoothed version of the original fBm process can be introduced [14]; this is a filtered version of the original surface, obtained by multiplying it by a differentiable test function, φ: the test function support is, for the time being, set equal to $[0, \varepsilon_x] \times [0, \varepsilon_y]$, ε_x and ε_y being related to the SAR resolutions in azimuth and ground range, respectively. Thus, we set:

$$\varphi(x,y) = \begin{cases} \frac{1}{\varepsilon_x \varepsilon_y} & if\ (x,y) \in [0,\varepsilon_x] \times [0,\varepsilon_y] \\ 0 & otherwise \end{cases} \tag{3.16}$$

$$z_\varphi(x,y) = \iint_{-\infty}^{\infty} z(x',y')\varphi(x-x',y-y')dx'dy' = \frac{1}{\varepsilon_x \varepsilon_y}\int_{x-\varepsilon_x}^{x}\int_{y-\varepsilon_y}^{y} z(x',y')dx'dy'. \tag{3.17}$$

A comment on the relevance of the partial derivatives of the observed surface in imaging theory is in order. These are of clear physical meaning, providing information on the asymmetry in the SAR data structure with respect to the x and y directions, intuitively consistent with the existence of a preferential direction of sight of SAR sensors.

In fact, as stated in the previous section, the reflectivity function, in a first order approximation, depends only on the partial derivative of the surface with respect to the ground range coordinate, as can be seen from Eq. (3.10). Moreover, the functional $z_\varphi(x,y)$ presented in Eq. (3.17) can be seen as a distribution [14]. Hence, for the fBm surface the partial derivative with respect to the ground range direction, $z_p(x,y;\varepsilon_y)$, can be defined using the theory of distributions, i.e. moving the derivation from the process $z(x,y)$ to the test function $\varphi(x,y)$ [15], thus obtaining:

$$
\begin{aligned}
z_p(x,y;\varepsilon_y,\varepsilon_x) &\triangleq \frac{\partial z(x,y)}{\partial y} \\
&= \iint_{-\infty}^{\infty} z(x',y')\frac{\partial \varphi}{\partial y}(x-x',y-y')dx'dy' = \\
&= \frac{1}{\varepsilon_x\varepsilon_y}\int_{x-\varepsilon_x}^{x}\int_{-\infty}^{\infty} z(x',y')\left[\delta(y-y')-\delta(y-\varepsilon_y-y')\right]dy'dx' = \\
&= \frac{1}{\varepsilon_x\varepsilon_y}\int_{x-\varepsilon_x}^{x}\left[z(x',y)-z(x',y-\varepsilon_y)\right]\,dx'
\end{aligned}
\tag{3.18}
$$

Hence, $z_p(x,y;\varepsilon_y)$ is linearly related to the fBm increment process and it is, for this reason, wide sense stationary.

3.2.3 Stochastic characterization of the fBm derivative process

Taking into account of the results presented in the previous section, it can be deduced that the autocorrelation function of the partial derivative process $z_p(x,y)$ can be evaluated starting from the correlation between two increments of the fBm original process:

$$
\begin{aligned}
R_{z_p}(\tau_x,\tau_y;\varepsilon_y) &= \langle z_p(x,y;\varepsilon_y)z_p(x+\tau_x,y+\tau_y;\varepsilon_y)\rangle = \\
&= \langle \frac{1}{(\varepsilon_x\varepsilon_y)^2}\int_{x-\varepsilon_x}^{x}\left[z(x',y)-z(x',y-\varepsilon_y)\right]\,dx'
\end{aligned}
$$

$$\int_{x-\varepsilon_x}^{x} \left[z\left(x''+\tau_x, y+\tau_y\right) - z\left(x''+\tau_x, y+\tau_y-\varepsilon_y\right)\right] dx''\rangle =$$

$$= \frac{1}{\left(\varepsilon_x\varepsilon_y\right)^2} \int_{x-\varepsilon_x}^{x}\int_{x-\varepsilon_x}^{x} \langle\left[z(x',y)z\left(x''+\tau_x, y+\tau_y\right) - z(x',y) \times\right.$$
$$z\left(x''+\tau_x, y+\tau_y-\varepsilon_y\right) - z\left(x', y-\varepsilon_y\right)z\left(x''+\tau_x, y+\tau_y\right)$$
$$\left.+z\left(x', y-\varepsilon_y\right)z\left(x''+\tau_x, y+\tau_y-\varepsilon_y\right)\right]\rangle\, dx'\, dx'' \quad (3.19)$$

wherein τ_x and τ_y are space lags in the azimuth and ground-range direction, respectively:

$$\tau_x = \sqrt{(x-x')^2} \;\; ; \quad \tau_y = \sqrt{(y-y')^2} \quad (3.20)$$

Considering that the autocorrelation of an fBm is given by Eq.(2.7) given in section 2.3.1, substituting that equation in Eq.(3.19) it turns out:

$$R_{z_p}\left(\tau_x, \tau_y; \varepsilon_y\right) = s^2 \frac{1}{\left(\varepsilon_x\varepsilon_y\right)^2} \int_{x-\varepsilon_x}^{x}\int_{x-\varepsilon_x}^{x} \left[\left|\tau_x^2 + (\tau_y+\varepsilon_y)^2\right|^H\right.$$
$$\left.+\left|\tau_x^2 + (\tau_y-\varepsilon_y)^2\right|^H - 2\left|\tau_x^2+\tau_y^2\right|^H\right] dx'dx'' =$$
$$= \varepsilon_y^{-2}\left[\left|\tau_x^2 + \left(\tau_y+\varepsilon_y\right)^2\right|^H + \left|\tau_x^2 + \left(\tau_y-\varepsilon_y\right)^2\right|^H\right.$$
$$\left.-2\left|\tau_x^2+\tau_y^2\right|^H\right]. \quad (3.21)$$

The autocorrelation function in Eq. (3.21) allows the evaluation of the two-dimensional power spectrum. However, in imaging theory (and in particular for a SAR sensor which is characterized by different spatial resolutions along azimuth and range), a more meaningful role is played by the power density spectra of cuts (along azimuth and ground range) of the image. Analytical expressions for these spectra are here analytically evaluated via a Fourier Transform of the azimuth and ground range cuts of the two-dimensional autocorrelation function reported in Eq. (3.21): as a matter of fact Eq. (3.21) shows that z_p is

wide sense stationary and the Wiener-Kintchine theorem can be applied.

- For a ground-range cut, from Eq. (3.21) we get:

$$R_p(\tau_y;\varepsilon_y) = R_{z_p}(\tau_x = 0, \tau_y;\varepsilon_y) = \\ = \frac{1}{2} s^2 {\varepsilon_y}^{2H-2} \left[\left(\frac{|\tau_y|}{\varepsilon_y} + 1 \right)^{2H} - 2 \left| \frac{\tau_y}{\varepsilon_y} \right|^{2H} + \left(\frac{|\tau_y|}{\varepsilon_y} - 1 \right)^{2H} \right] \quad (3.22)$$

leading to [16], [17]:

$$W_p(k_y;\varepsilon_y) = 2s^2 {\varepsilon_y}^{-1+2H} \Gamma(1+2H) \sin(\pi H) \times \\ \left[1 - \cos(|k_y|\varepsilon_y)\right] \frac{1}{(|k_y|\varepsilon_y)^{1+2H}} . \quad (3.23)$$

In this case, the autocorrelation function, R_p, and the PSD, W_p, of the derivative process match exactly with those introduced for a one-dimensional profile [17].
Moreover, it is interesting and useful, to evaluate $\widetilde{W}_p$ defined as the limit of W_p for $k_y\varepsilon_y \to 0$:

$$\widetilde{W}_p(k_y) = s^2 \Gamma(1+2H) \sin(\pi H) \frac{1}{|k_y|^{2H-1}}. \quad (3.24)$$

In Eq. (3.24) $\widetilde{W}_p(k_y)$ provides an asymptotic evaluation and is amenable to meaningful interpretation and application: for every k_y it is analytically obtained by reducing the support of the test function; alternatively, for every ε_y, i.e., for actual radar resolutions, it approximates the low spatial wavenumbers regime of the estimated PSD.

- For the azimuth cut, from Eq. (3.21) we get:

$$R_p(\tau_x;\varepsilon_y) = R_{z_p}(\tau_x, \tau_y = 0;\varepsilon_y) = \\ = s^2 {\varepsilon_y}^{-2} \left[\left| \tau_x^2 + \varepsilon_y^2 \right|^H - |\tau_x|^{2H} \right]. \quad (3.25)$$

Evaluation of the corresponding PSD requires resorting to generalized Fourier Transforms; for the first term of Eq. (3.25) we get [1], [16]:

$$\int_{-\infty}^{\infty} \left|{\tau_x}^2 + {\varepsilon_y}^2\right|^H e^{-ik_x\tau_x} d\tau_x = \\ = \frac{2^{\left(\frac{3}{2}+H\right)}\sqrt{\pi}{\varepsilon_y}^{\left(\frac{1}{2}+H\right)} \mathrm{K}_{H+\frac{1}{2}}\left(|k_x|\varepsilon_y\right) \frac{1}{|k_x|^{\frac{1}{2}+H}}}{\Gamma(-H)}, \quad (3.26)$$

and for the second term we obtain [16], [17]:

$$\int_{-\infty}^{\infty} |\tau_x|^{2H} e^{-ik_x\tau_x} = 2\,\Gamma(1+2H)\sin(\pi H)\frac{1}{|k_x|^{1+2H}}. \quad (3.27)$$

Thus, we can evaluate in closed form the PSD of $z_p(x,y)$ for an azimuth cut of the surface:

$$W_p\left(k_x;\varepsilon_y\right) = s^2{\varepsilon_y}^{-1+2H}\left[\frac{2^{\left(\frac{3}{2}+H\right)}\sqrt{\pi}\mathrm{K}_{H+\frac{1}{2}}\left(|k_x|\varepsilon_y\right)\frac{1}{\left(|k_x|\varepsilon_y\right)^{\frac{1}{2}+H}}}{\Gamma(-H)}\right. \\ \left. +2\,\Gamma(1+2H)\,\sin(\pi H)\frac{1}{\left(|k_x|\varepsilon_y\right)^{1+2H}}\right] \quad (3.28)$$

where $\mathrm{K}_\nu(\cdot)$ is the modified Bessel function of second type of fractional order ν.

In order to point out the asymptotical spectral behavior of the aforementioned spectrum, we can express the function $\mathrm{K}_{H+\frac{1}{2}}\left(|k_x|\varepsilon_y\right)$ through a power series expansion around the value $k_x = 0$ stopped to the first order [16]:

$$K_{H+\frac{1}{2}}(|k_x|\varepsilon_y) = 2^{-\frac{3}{2}-H}(|k_x|\varepsilon_y)^{\frac{1}{2}+H}\left[1+\frac{(|k_x|\varepsilon_y)^2}{(6+4H)}\right]\Gamma\left(-\frac{1}{2}-H\right) + 2^{-\frac{1}{2}+H}(|k_x|\varepsilon_y)^{-\frac{1}{2}-H}\left[1+\frac{(|k_x|\varepsilon_y)^2}{(2-4H)}\right]\Gamma\left(\frac{1}{2}+H\right). \quad (3.29)$$

Therefore, substituting Eq. (3.29) in Eq. (3.28) we obtain the following expression of the spectrum:

$$\widetilde{W}_p(k_x;\varepsilon_y) = s^2{\varepsilon_y}^{2H-1}\left\{\frac{\sqrt{\pi}\Gamma\left(-\frac{1}{2}-H\right)}{\Gamma(-H)}+\frac{\sqrt{\pi}\Gamma\left(-\frac{1}{2}-H\right)}{2(2H)\Gamma(-H)}\times (|k_x|\varepsilon_y)^2+\frac{\sqrt{\pi}\,2^{1+2H}\Gamma\left(\frac{1}{2}+H\right)}{(1-2H)\Gamma(-H)}\frac{1}{\left(|k_x|\varepsilon_y\right)^{2H-1}}+\left[\sqrt{\pi}\,2^{1+2H}\times \frac{\Gamma\left(\frac{1}{2}+H\right)}{\Gamma(-H)}+2\Gamma(1+2H)\sin(\pi H)\right]\frac{1}{\left(|k_x|\varepsilon_y\right)^{2H+1}}\right\}. \quad 3.29)$$

Expression (3.24) can be simplified by considering that [16]:

$$\frac{\sqrt{\pi}\Gamma\left(\frac{1}{2}+H\right)}{\Gamma(-H)} = -2^{-2H}\Gamma(1+2H)\sin(\pi H), \quad (3.30)$$

so Eq. (3.29) can be written as:

$$\widetilde{W}_p(k_x;\varepsilon_y) = s^2{\varepsilon_y}^{2H-1}\left\{\frac{\sqrt{\pi}\Gamma\left(-\frac{1}{2}-H\right)}{\Gamma(-H)}+\frac{\sqrt{\pi}\Gamma\left(-\frac{1}{2}-H\right)}{4H\Gamma(-H)}\times\right.$$

$$(|k_x|\varepsilon_y)^2 - \frac{2\Gamma(1+2H)\sin(\pi H)}{2-4H}\frac{1}{\left(|k_x|\varepsilon_y\right)^{2H-1}}\Bigg\}. \quad (3.31)$$

The introduced formulas deserve some significant considerations. First of all, differently from the case of the ground-range cut, the spectrum of the partial derivative process for the azimuth cut does not show a power law behavior, not even asymptotically.
Owing to the radar preferential direction of sight, in the case of a range profile we are considering the derivative along the same direction of the performed cut; this implies that the spectrum of the derivative process inherits the correlation properties of successive increments of the fBm profile. Conversely, for an azimuth profile such considerations are not valid anymore: in this case we are considering the derivative in the ground range direction whereas the profile originates from an azimuth cut of the surface, so the properties of the derivative process is not directly linked to the profile behavior.

3.3 Electromagnetic model: the Small Perturbation Method

In order to evaluate the reflectivity pattern γ, an appropriate scattering model is necessary, taking into account the specific geometrical characterization used for the observed scene. Hence, we must consider the interaction between the electromagnetic field and the fractal surface by means of an appropriate fractal scattering model tailored to the case at hand. The candidate scattering model should lead to a closed form solution for the reflectivity function (and for the backscattering coefficient). For rough surfaces only approximate solutions are available, each solution being valid under appropriate roughness and illumination conditions [3],[7],[8]. In this paper we use the SPM which provides the simplest expression for the NRCS and shows a range of validity adequate to SAR applications.

3.3.1 Small Perturbation Method

The Small Perturbation Method (SPM) suggests a perturbative approach for the evaluation of the field scattered from an fBm surface. This method is based on the fulfillment of some conditions.
The first condition is set on the surface profile: surface heights variations must be small with respect to the incident field wavelength. The second condition enforces a bound on the surface slopes that must be much smaller than 1 [3].
The SPM expression of the scattered power density is:

$$\langle |E_{pq}|^2 \rangle = \frac{2^{H+1}\Gamma^2(1+H)\sin(\pi H)}{(\pi \mathrm{k} r)^2(\sin^2\theta_i + \sin^2\theta_s - 2\sin\theta_i \sin\theta_s \cos\phi_s)^{\frac{2H+2}{2}}} \times$$

$$A\cos^2\theta_s \cos^2\theta_i |E_i|^2 |\beta_{pq}|^2 (kT)^{2(1-H)}, \qquad (3.32)$$

where θ_i and θ_s are respectively the incidence and scattering angle, φ_s is the angle between the x-axes and the projection of the radius between the center of the scene and the receiver on the *x-y* plane, *k* is the electromagnetic wavenumber and β_{pq} is a coefficient that depends on polarization, incidence and scattering angles, and the relative complex dielectric constant, ε_r, of the scattering medium. *H* and *T* are respectively the Hurst coefficient and the topothesy of the illuminated fractal surface.
In the backscattering case, Eq.(3.32) turns into:

$$\sigma^0_{pp} = 4\mathrm{k}^4 \cos^4\theta |\beta_{pp}|^2 \frac{S_0}{\pi(2k\, sen\theta)^\alpha} \qquad (3.33)$$

with S_0 and α being the spectral amplitude and the spectral slope of the illuminated fractal surface defined in Eq. (2.20) and Eq. (2.21) and $\theta = \theta_i = \theta_s$.
In Eq. (3.33) it must be k > k_{min} defined in (2.24) and $\theta_{min} < \theta < \theta_{max}$, where:

$$\theta_{min} = sen^{-1}\left(\frac{k_{min}}{2\mathrm{k}}\right) \tag{3.34}$$

$$\theta_{max} = \begin{cases} sen^{-1}\left(\frac{k_{min}}{2k}\right) & se\ k_{max} < 2k \\ \frac{\pi}{2} & se\ k_{max} \geq 2k \end{cases} \tag{3.35}$$

Indeed, if $k_{min} \ll k \ll k_{max}$ (cf. Eq. 2.25), Eq. (3.4) holds for any incidence angle, except at near vertical incidence. Expressions of β_{pp} for the backscattering case are the following:

$$\beta_{hh} = \frac{cos\theta - (\varepsilon_r - sen^2\theta)^{1/2}}{cos\theta + (\varepsilon_r - sen^2\theta)^{1/2}} \tag{3.36}$$

$$\beta_{vv} = (\varepsilon_r - 1)\frac{sen^2\theta - \varepsilon_r(1 + sen^2\theta)}{\left[\varepsilon_r\, cos\theta + (\varepsilon_r - sen^2\theta)^{1/2}\right]^2} \tag{3.37}$$

$$\beta_{hv} = \beta_{vh} = 0 \tag{3.38}$$

The analysis of Eq. (3.33) leads to some interesting considerations. First of all, we note that the backscattering coefficient is proportional to the spectral parameter S_0, hence to s^2, see Eq. (2.20). Furthermore, the backscattering coefficient is explicitly frequency-dependent, $\sigma_{pp}^0 \propto \mathrm{k}^{4-\alpha}$, in addition to the frequency dependence of surface electromagnetic parameters. This frequency dependence becomes weaker as α increases, and it disappear when α reaches its maximum value, 4 (i.e. H=1, D=2).

An approximate evaluation of the validity limits for the SPM model is given by the following inequality:

$$\mathrm{k}^2\sigma^2 \cong 2^{2H+1}\pi^2\frac{\Gamma(1+H)}{\Gamma(1-H)}\left(\frac{T}{\lambda}\right)^2\left(\frac{\tau_{max}}{T}\right)^{2H} \ll 1 \tag{3.39}$$

where σ is the variance of the surface height.

3.3.2 Evaluation of the SAR image reflectivity coefficients for the SPM model

In this section the evaluation of the SAR image reflectivity coefficients a_0, a_1, defined in Eq. (3.11), is performed. The results presented in Section 3.2.1 are exploited, in order to obtain an expression of the reflectivity function as a function of the partial derivatives of the surface. In particular, substituting the expression of $\cos\theta$ provided in Eq. (3.9) and the corresponding expression of $\sin\theta$, into Eq. (3.33) and, taking into account that the term $|\beta_{pp}|^2$ can be considered constant with θ in the angular interval of interest in the co-polarized case, the NRCS can be then expressed as

$$\sigma^0 = A_0 \left(\frac{(\cos\theta_0 + p\,\sin\theta_0)^2}{p^2+q^2+1} \right)^2 \times \left(\frac{(\sin\theta_0 - p\,\cos\theta_0)^2 + q^2}{p^2+q^2+1} \right)^{-(1+H)}, \quad (3.40)$$

wherein

$$A_0 = \frac{S_0 \kappa^{1-2H} |\beta_{pp}|^2}{2^{2H}}. \quad (3.41)$$

Therefore $|\gamma(x,y)|$, which is related to σ^0 by Eq. (2.5), can be evaluated as:

$$|\gamma(x,y)| = f\big(\theta(p,q)\big) = \sqrt{A_0} \left(\frac{(\cos\theta_0 + p\,\sin\theta_0)^2}{p^2+q^2+1} \right) \times \left(\frac{(\sin\theta_0 - p\,\cos\theta_0)^2 + q^2}{p^2+q^2+1} \right)^{\frac{-(1+H)}{2}}. \quad (3.42)$$

Performing the McLaurin series expansion of the expression in Eq. (3.42) we obtain the coefficients a_0 and a_1 (see Eq. 3.10) relevant to the SPM scattering function:

$$|\gamma(x,y)| \cong a_0 + a_1 p = \sqrt{A_0}\{\cos^2\theta_0 \sin^{-(1+H)}\theta_0 + \cos\theta_0 \sin^{-H}\theta_0[2 + (1+H)\cos^2\theta_0 \sin^{-2}\theta_0]p\}, \quad (3.43)$$

wherein p is characterized in Section 3.2.3. Therefore, in the case of interest, the coefficients a_0 and a_1, and in turn the validity limits of the proposed model, depend on the considered look angle and on the fractal parameters of the observed surface.

3.4 Stochastic characterization of the SAR image

Exploiting the results obtained in the previous sections, the complete statistical characterization of a SAR image is presented in this section. According to the theoretical results presented in the previous sections, provided that the slopes of the surface are sufficiently low, the image is linearly dependent on the partial derivative process $z_{p,}$ whose expression is given in Eq. (3.18). Hence the image inherits the same statistical characterization of the process $z_p(x,y)$, i.e. it is Gaussian distributed with $\mu = a_0$ and $\sigma = a_1 s \Delta y^{\mathrm{H}-1}$, as we can deduce combining Eq. (3.10) and (3.18).

A discussion is now in order on the role of ε_x and ε_y, defining the support of the kernel φ mentioned in the previous section, which formally determines the effective bandwidth of the imaging system whenever applied to the fractal surfaces. As far as the bandwidth is concerned, our model implies dealing with two, somehow implicit, band-limiting procedures that can be conveniently formalized as two filtering steps that we now explicitly discuss. First of all, the electromagnetic field impinging on the rough surface performs a low-pass filtering on the surface according to the electromagnetic wavelength, λ. Then, the obtained smoothed process is filtered according to the sensor impulse response Eq. (3.1), and spatial scales lower than the resolution one are discarded. In our case, assuming x and y as coordinates, in azimuth and ground-range directions, respectively, and Δx and Δy as the corresponding sensor resolutions, we can consider, being $\Delta x, \Delta y >> \lambda$, directly the second filtering step

and we can take ε_x and ε_y coincident with the azimuth and ground-range resolutions.

Considering the expression of the SAR image autocorrelation function (see Eq. (3.2)), and applying the Wiener-Kintchine theorem, we can now provide the power density spectra for a range, $W_i(k_y)$, and an azimuth, $W_i(k_x)$, cut of the image in closed form:

$$W_i(k_y) = a_1^2 W_p(k_y;\, \Delta y)\mathrm{rect}\left[\frac{\Delta y \sin^2\theta_0\, k_y}{\pi}\right] \tag{3.44}$$

$$W_i(k_x) = a_1^2 W_p(k_x;\, \Delta y)\mathrm{rect}\left[\frac{\Delta x k_x}{\pi}\right] \tag{3.45}$$

Recalling that for the closed form expression obtained in the previous section for the power density spectra $W_p(k_y;\, \Delta y)$ and $W_p(k_x;\, \Delta y)$ in Eqs. (3.23), (3.28) and for their asymptotic formulations in Eqs. (3.24), (3.31) a meaningful dependence on the fractal parameters of the observed surface was found, we can now draw some significant considerations. As a matter of fact, image range cuts – in an appropriate range of frequencies, i.e. $k_y \Delta y \ll 2\pi$ – exhibit spectra with a linear behavior in a log-log plane, as shown in Eq. (3.24), thus allowing implementation of linear regression techniques to retrieve the fractal parameters of the observed scene directly from the corresponding radar image. In particular, by comparing Eq. (3.24) with the expression of the PSD of a one-dimensional cut of the surface in Eq. (3.12), we infer that, in the log-log plane, the slope of the range spectrum of a SAR image is equal to that of the imaged surface whereas the surface Hurst coefficient is decreased by one. Conversely, for azimuth cuts, as we infer from Eq. (3.31), also for very low frequencies, the above discussion does not hold any longer; the azimuth image spectrum is quite involved and the retrieving techniques should be non linear ones.

For a visual inspection of the obtained theoretical results, in Figs. 3.2-3.5 the azimuth (dash-dot line) and range (continuous line) spectra of an image are shown in a log(k) - log(|W(k)|) plane, where the same values of s=0.1 m^{1-H} and a_1=1 and different H values (marked in the captions) are considered; for comparison purposes, also the behavior

of the spectrum of a cut of the original surface relevant to Eq. (3.12) (dashed line) is reported in the same graphs. In order to compare the spectra behaviors wavenumbers are normalized to the value of the considered resolution.

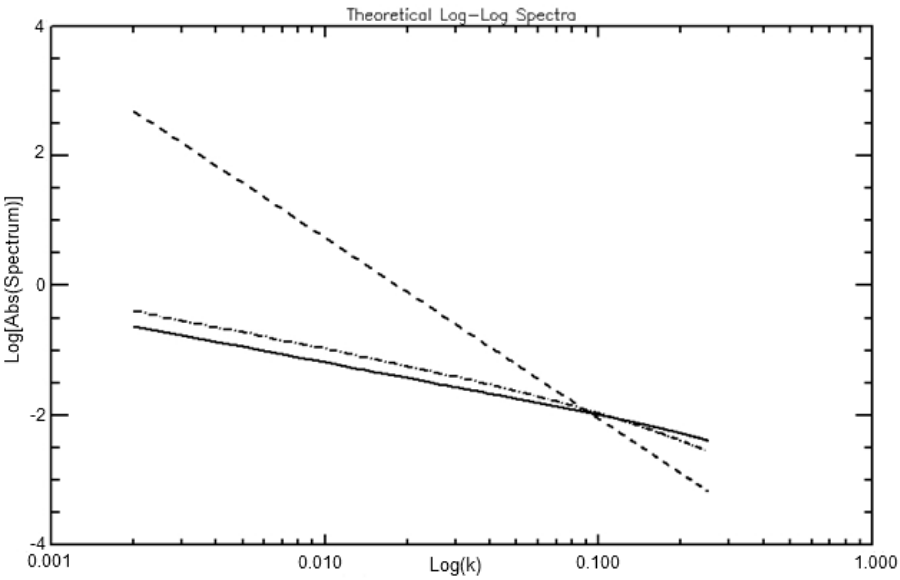

Fig. 3.2 Theoretical log-log plots of range (continuous line) and azimuth (dash-dot line) image cuts PSD; the dashed line represents the surface cut PSD. All the graphs are relevant to H=0.9.

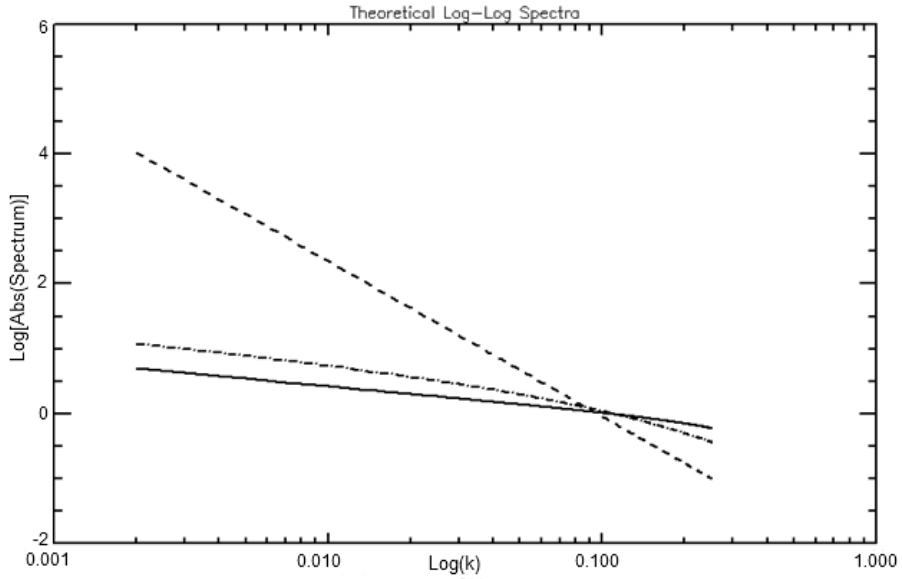

Fig. 2.3: Theoretical log-log plots of *range* (continuous line) and *azimuth* (dash-dot line) image cuts PSD; the dashed line represents the surface cut PSD. All the graphs are relevant to H=0.7.

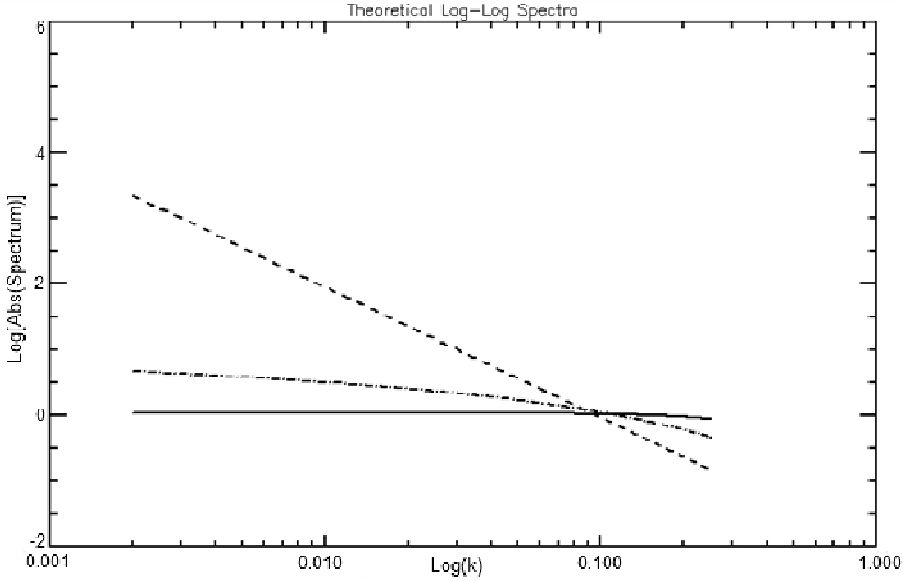

Fig. 3.4: Theoretical log-log plots of *range* (continuous line) and *azimuth* (dash-dot line) image cuts PSD; the dashed line represents the surface cut PSD. All the graphs are relevant to H=0.5.

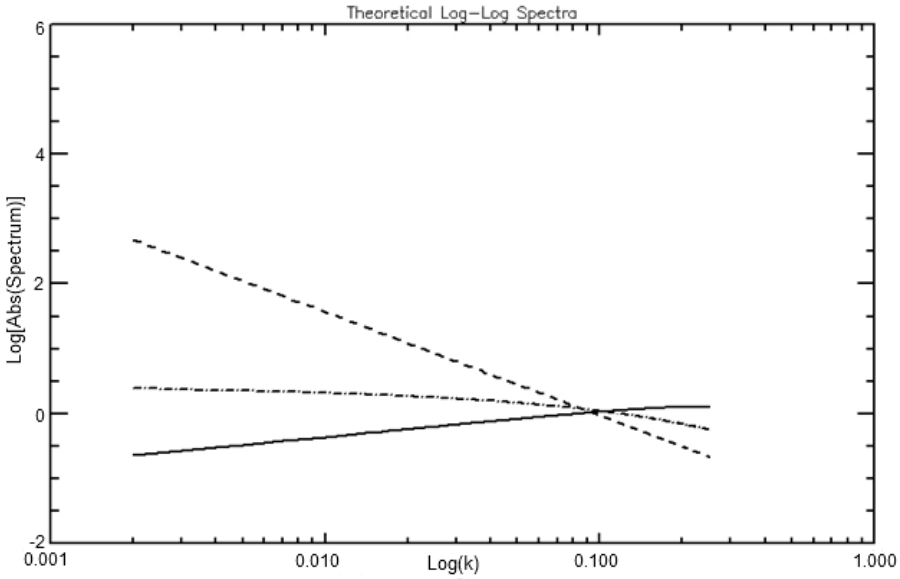

Fig. 3.5: Theoretical log-log plots of *range* (continuous line) and *azimuth* (dash-dot line) image cuts PSD; the dashed line represents the surface cut PSD. All the graphs are relevant to H=0.3.

The provided figures show clearly the difference in the behaviors of range and azimuth image cuts PSDs. The behavior of the range cut PSD is linear in the log(k) - log(|S(k)|) plane for sufficiently low spatial frequencies, presenting a slope equal to that of the range cut PSD (dashed lines) decreased by two (compare Eq. (3.24) and (3.12)). Conversely, the plot of the azimuth cut PSD presents a more complex behavior that is, actually, not at all a power-law one.

References

[1] G. Di Martino, D. Riccio and I. Zinno, "SAR Imaging of Fractal Surfaces", IEEE Trans. Geosci. Remote Sens., in print, available on IEEE Early Access.

[2] G. Franceschetti, R. Lanari, *Synthetic Aperture Radar Processing.* CRC Press, New York, 1999.

[3] G. Franceschetti, D. Riccio, *Scattering, Natural Surfaces and Fractals*. Academic Press, Burlington (MA), USA, 2007.

[4] B.B. Mandelbrot, The Fractal Geometry of Nature. New York: Freeman, 1983

[5] Falconer, K. Fractal Geometry. Chichester, England: JohnWiley, 1990

[6] P. Kube and A. Pentland, “On the imaging of fractal surfaces,” *IEEE Trans. Pattern Anal. Mach. Intell.*, vol. 10, no. 5, pp. 704–707, Sep. 1988.

[7] G. Franceschetti, A. Iodice, and D. Riccio, “Fractal models for scattering from natural surfaces,” in *Scattering*, R. Pike and P. Sabatier, Eds. London, U.K.: Academic, Sep. 2001, pp. 467–485.

[8] G. Franceschetti, A. Iodice, M. Migliaccio, D. Riccio, "Scattering from natural rough surfaces modeled by fractional Brownian motion two-dimensional processes", *IEEE Trans. Antennas Prop.*, vol. 47, no. 9, pp. 1405-1415, Sep. 1999.

[9] P. Flandrin, “On the spectrum of Fractional Brownian Motion”. *IEEE Trans. Inform. Theory*, 35, 197-199, Jan. 1989.

[10] T. Austin, A. W. England, G. H. Wakefield, “Special problems in the estimation of power-law spectra as applied to topographical modeling”, *IEEE Trans. Geosci. Remote Sens.*, vol. 32, no. 4, pp. 928-939, July 1994.

[11] M. K. Shepard, B. A. Campbell, M. H. Bulmer, T. G. Farr, L. R. Gaddis, and J. J. Plaut, "The roughness of natural terrain: A planetary

and remote sensing perspective", *J. Geophys. Res.*, 106, 32,777–32,795, Dec. 2001.

[12] Gaddis, L.R., Mouginis-Mark, P.J. and Hayashi, J.N., "Lava flow surface textures: SIR-B radar image texture, field observations, and terrain measurements" *Photogrammetric Eng. Remote Sens.*, 56, 211-224, Feb. 1990.

[13] B. B. Mandelbrot, J. W. Van Ness, “Fractional Brownian motions, fractional noises and applications”, *SIAM Rev.*, vol. 10, no. 4, pp. 422-437, Oct. 1968.

[14] B.B. Mandelbrot, *Gaussian Self-Affinity and Fractals*. Springer Verlag, New York, 2001.

[15] I. M. Gelfand and G. E. Shilov, *Generalized Functions*. Burlington, MA: Academic, 1964.

[16] I. S. Gradshteyn and I.M. Ryzhik, *Table of Integrals, Series and Products.* New York: Academic, 1980.

[17] G. Di Martino, A. Iodice, D. Riccio, G. Ruello, "Imaging of Fractal Profiles", *IEEE Trans. Geosci. Remote Sens.*, vol. 48, no. 8, pp. 3280 - 3289, Aug. 2010.

Chapter 4

Theoretical Framework Validation

In this chapter a complete experimental setup directed towards the validation of the theoretical framework presented in the previous section is shown. The fundamental issue is to compare the theoretically evaluated PSDs of a range and an azimuth cut of the SAR image of a natural surface (respectively Eq. (3.44) and (3.45)) with the corresponding PSDs estimated directly from a SAR image. To this aim, SAR images of fractal surfaces having controlled and known fractal parameters have been generated. First, fBm surfaces [1] have been synthesized using the corresponding Weierstrass Mandelbrot function [2], then, the latter are used as input for the SARAS (SAR image simulator [3]) that provides, after choosing the specific sensor to simulate, the corresponding SAR image of the input fractal surface.

4.1 Generation of simulated SAR images of fractal surfaces

In order to synthesize a band-limited fBm surface of known and controlled parameter, a WM function can be used as widely discussed in section 2.3.3 [4]. As a matter of fact, calculating, via Equation (2.27), the B parameter for the corresponding WM function and evaluating the WM ensemble via Eq. (2.23), the obtained WM function holds an H value equal to the Hurst coefficient of the corresponding fBm process. Furthermore, the ν value of Eq. (2.23) is set equal to 1.013 (the more ν approaches to 1, the better the WM function approximates the fBm process). k_0 is evaluated via Eq. (2.24)

with a safety factor χ_1 equal to 0.1 and the surface is generated with 1424 tones.

In Fig. 4.1 and 4.2 fBm surfaces of parameters H=0.8, s=0.1 $m^{0.2}$ and H=0.7, s=$0.5^{0.3}$ synthesized via Weierstrass-Mandelbrot functions are shown.

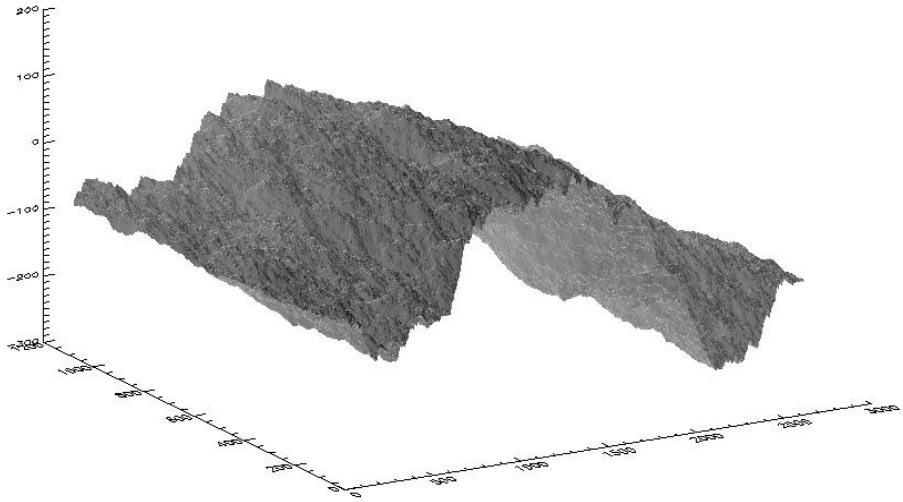

Fig. 4.1: Fractal surface of parameter s=0.1 $m^{0.2}$, H=0.8 synthesized via a Weierstrass-Mandelbrot function.

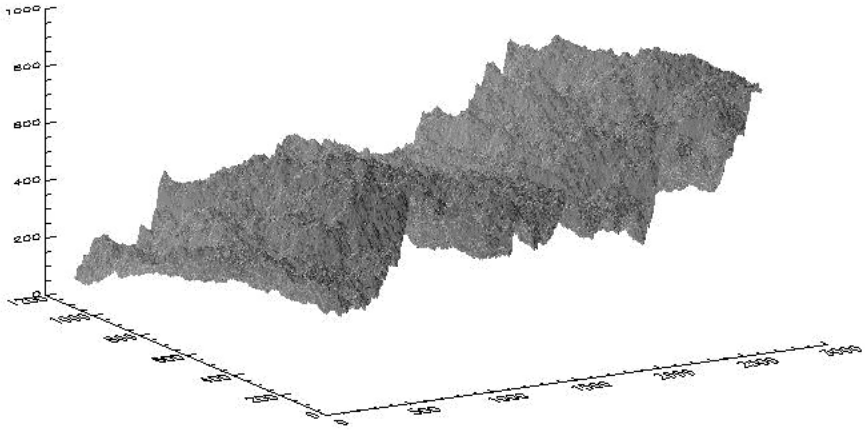

Fig. 4.2: Fractal surface of parameter s=0.5$m^{0.3}$, H=0.7 synthesized via a Weierstrass-Mandelbrot function.

The so obtained surfaces are used as input Digital Elevation Model (DEM) to SARAS, a SAR image advanced simulator [3]. SARAS

allows choosing the type of sensor to simulate and the scattering function to adopt. It is worth to note that, in this case, it is assumed that the observed surface shows the same user-defined fractal parameters at all the scales of interest (i.e., both at macroscopic and microscopic scales). Envisat images ($\Delta x = 3.986,\ \Delta y = 19.928$) are simulated, thus allowing the analysis of the case of extremely different resolutions in azimuth and range directions and, as anticipated in Section 3.3, the SPM fractal scattering model,[4], [5], consistent with the fractal model of the surface with a VV polarization is chosen. Note that use of an HH polarization does not significantly change the obtained results, as previously stated in Section 3.3.2.
The Envisat simulated images relevant to the fBm surfaces depicted in Fig. 4.1 and 4.2 are shown in Fig. 4.3 and 4.4, respectively.

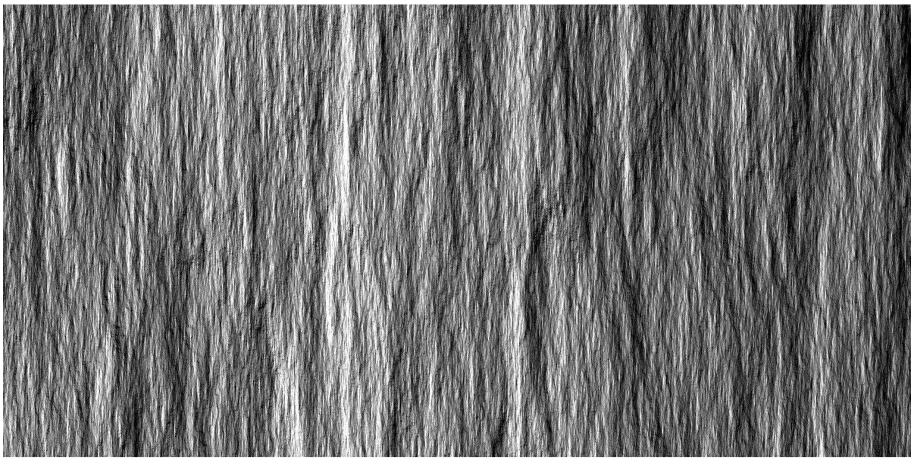

Fig. 4.3: Simulated Envisat image relevant to the fBm surface in Fig. 4.1

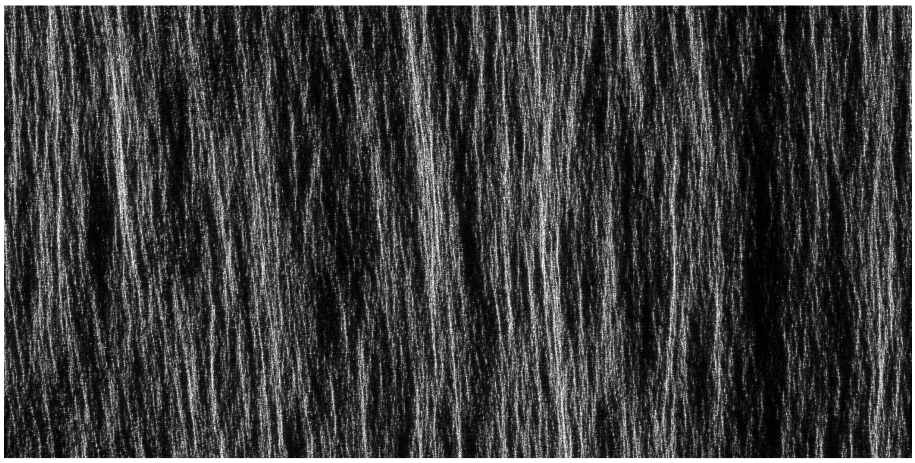

Fig. 4.4: Simulated Envisat image relevant to the fBm surface in Fig. 4.2

4.2 Spectral estimation for a SAR image

The spectrum estimation problem is not a trivial one: as a matter of fact, power law spectra introduce unique difficulties in spectral estimation as they greatly suffer leakage effects and high variance problems, which can give rise to deep modifications of the original spectral slope. Moreover, concerning the spectrum estimation relevant to a finite data segment, in order to reduce the variance, the use of a large number of samples allowing the evaluation of average spectra would be desirable. This condition cannot be satisfied in the practical cases of fractal parameters estimation from actual SAR images, as spectra relevant to small homogeneous areas of the image must be considered to obtain a punctual information. Hence, the limited dimension of the data set requires to resort to a spectral estimator able to reduce as much as possible both leakage and variance of the estimate also in presence of a small number of samples [6], [7]. Hence, for our application the use of classical spectral estimators, such as the periodogram obtained using Fourier-based techniques, does not represent a good solution. Conversely, the Capon estimator [6], [7] strongly reduces the above-mentioned negative effects and it is particularly well suited when facing short data records.

4.2.1 Capon estimator

The Capon estimator essentially performs a filtering which is customized for each frequency of interest and which is aimed to minimize the total power output, with the constraint that the gain at the frequency of interest is unity [6], [7], [8]. In particular, in the power law case the sidelobes of the filter are adjusted in order to avoid leakage from low frequency components. In order to evaluate the power spectrum, the Capon method requires the evaluation of an estimate of the autocorrelation matrix. In this paper we use the covariance method, which provides an unbiased and consistent estimator [8]. According to this method the elements of the autocorrelation matrix relevant to a one-dimensional range cut of our SAR image, *I*, of which *N* samples are available, can be estimated as:

$$\left[\hat{R}_I\right]_{ij} = \frac{1}{2(N-p)}\left[\sum_{n=p}^{N-1} I[n-i]I[n-j] + \sum_{n=0}^{N-1-p} I[n+i]I[n-j]\right]. \quad (4.1)$$

The Capon estimate of the spectrum of interest can be then computed as:

$$\hat{S}_p(k_y) = \frac{p\Delta y}{\mathbf{e}^* \hat{R}_I^{-1} \mathbf{e}}, \quad (4.2)$$

wherein p is the dimension of the autocorrelation matrix, Δy is the ground range resolution of the SAR image, * stands for conjugate transpose and

$$\mathbf{e} = \left[1 \quad e^{j2\pi k_y \Delta y} \quad e^{j4\pi k_y \Delta y} \quad \ldots \quad e^{j2\pi(p-1)k_y \Delta y}\right]^T. \quad (4.3)$$

The bias of the Capon estimator is independent of *N*, but it is dependent on *p*. An increase in *p* determines a decrease in the bias at

the expense of an increased variance. Indeed, note that $p\Delta y$ is the longest lag for which the autocorrelation is estimated and, obviously, the range of p is constrained by N. For this estimator the region of high accuracy for the estimated spectra is $1/(2p\Delta y) < k_y < 1/(2\Delta y)$. Different values of p will be tested in Section 4.3 in order to analyze the behavior of the obtained spectral estimates as a function of this parameter.

However, also the aliasing, due to the fact that the imaged surface will generally have frequency components at spatial frequencies above the Nyquist frequency, $f_s = 1/(2\Delta y)$ should be considered. Hence, according to the literature on the subject [6], the values of the spectral estimate computed for normalized wavenumbers greater than $f_s/2$, are discarded.

4.2.2 Range and azimuth PSD estimation

In order to compare the theoretical PSDs of a range and an azimuth cut of the image evaluated in Section 3.4 (Eq. (3.44) and (3.45), respectively) with those estimated from the SAR image, it must be taken into account that the theoretical spectra are averaged spectra. Hence, for each direction, starting from the SAR image, several cuts, sufficiently spaced one from each other to be considered uncorrelated, are performed. The spectra of these profiles are estimated using the Capon estimator and, finally, these spectra are averaged in order to obtain the estimated mean PSD. Initially, for the sake of the theoretical comparison, 1000 samples profiles are considered and the length of the Capon filter is set equal to 250 (a quarter of the total number of samples, as suggested in the literature on the subject [8]).

As an example, in Fig. 4.5, a non-filtered PSD is shown where the vertical axes enclose the range of wavenumbers used for estimation. In this figure the image estimated spectrum (continuous line) is compared with the theoretical one (dash-dot-dot line) computed substituting H=0.8 in Eq. (3.23) and the dashed and dash-dot lines mark the limit theoretical spectra, i.e. those presenting H=0.999 and H=0.001, respectively. Note that, beyond the range of values of H equal to]0,1[the surface is not a fractal surface, as stated in Chapter 2 when the fBm process was introduced.

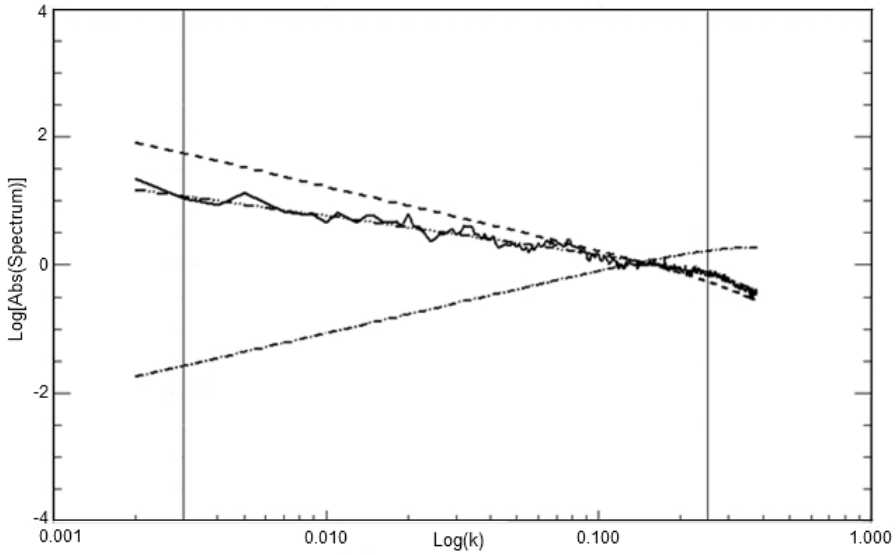

Fig. 4.5: Mean PSD of range cut of the image before applying the Capon filtering (continuous line) compared with the theoretical one (dash-dot-dot line) for a fractal surface with H=0.8, s=0.1 [$m^{0.2}$]. The theoretical spectra for H=0.999 (dashed line) and H=0.001 (dash-dot line), which represent the limit of H for which a surface holds a fractal behavior, are reported. The two vertical axes mark the wavenumbers beyond which the spectrum is cut.

In Fig. 4.6 - 4.10 significant results relevant to comparisons between range and azimuth theoretical and estimated and filtered spectra for the values of s and H reported in the corresponding captions are presented. The theoretical spectra for H=0.999 (dashed line) and H=0.001 (dash-dot line), which represent the limit of H for which a surface holds a fractal behavior, are also reported in each figure in order to clarify the range of slopes inside which the spectrum is fractal.

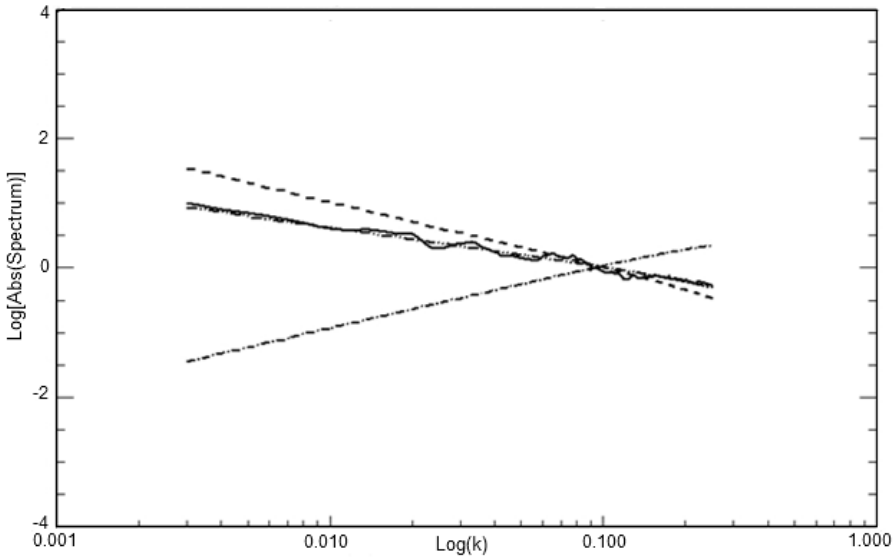

Fig. 4.6: Mean PSD of range cut of the image after the application of the Capon filter (continuous line) compared with the theoretical one (dash-dot-dot line) for a fractal surface with H=0.8, s=0.1 [$m^{0.2}$].

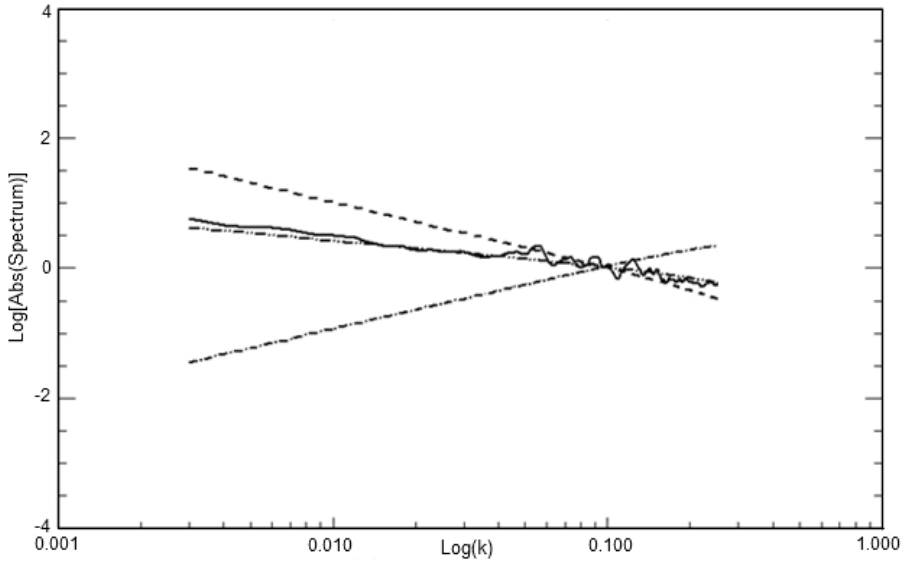

Fig. 4.7: Mean PSD of range cut of the image after the application of the Capon filter (continuous line) compared with the theoretical one (dash-dot-dot line) for a fractal surface with H=0.7, s=0.1 [$m^{0.3}$].

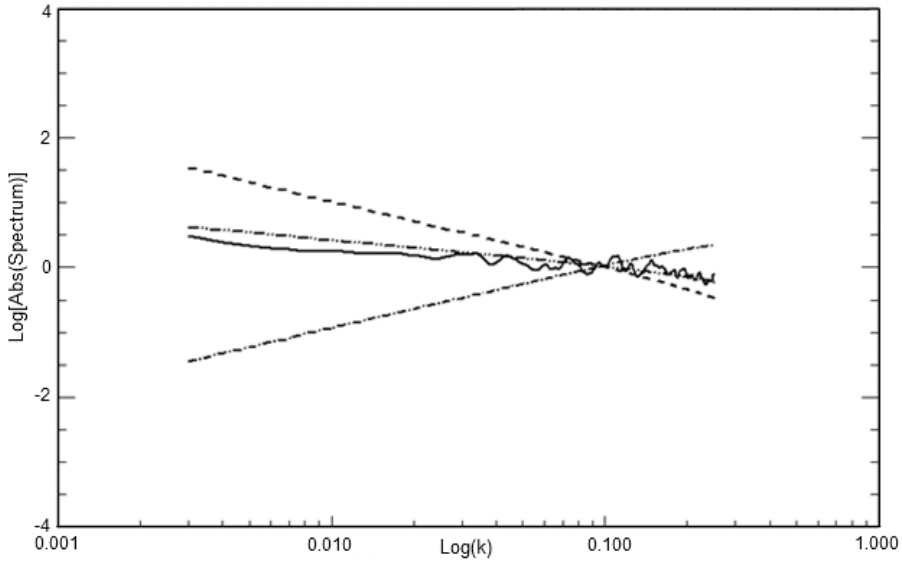

Fig. 4.8: Mean PSD of range cut of the image after the application of the Capon filter (continuous line) compared with the theoretical one (dash-dot-dot line) for a fractal surface with H=0.6, s=0.1 [$m^{0.4}$].

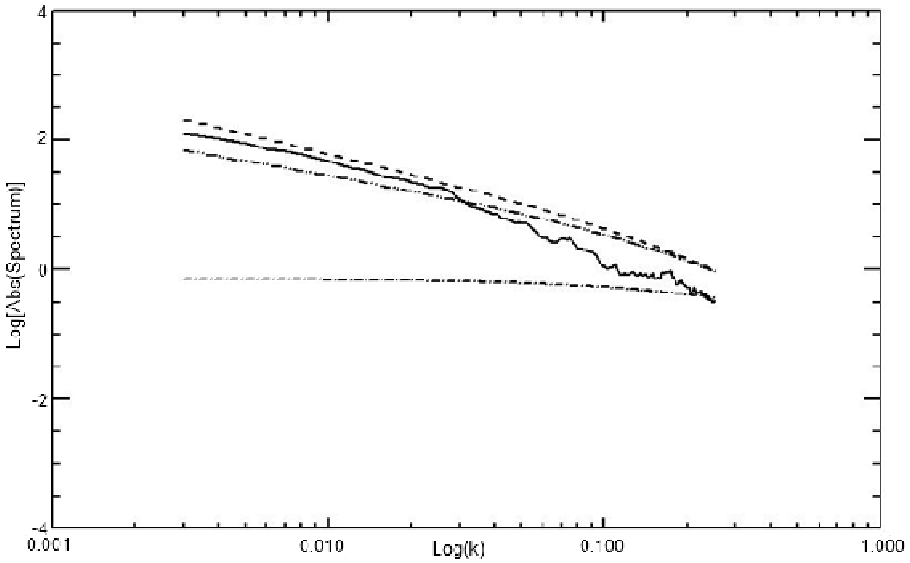

Fig. 4.9: Mean PSD of azimuth cut of the image after the application of the Capon filter (continuous line) compared with the theoretical one (dash-dot-dot line) for a fractal surface with H=0.8, s=0.1[$m^{0.2}$].

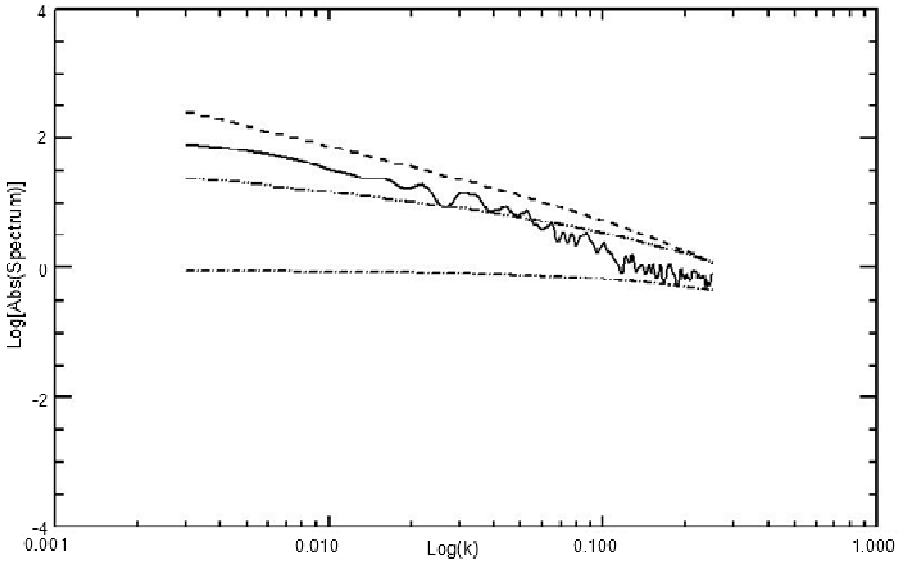

Fig. 4.10: Mean PSD of azimuth cut of the image after the application of the Capon filter (continuous line) compared with the theoretical one (dash-dot-dot line) for a fractal surface with H=0.6, s=0.1[$m^{0..42}$].

It is worth stressing that, in the presented cases, the estimation is performed on profiles of 1000 samples, so that low frequency components can be easily estimated. This is not always the case when the analysis of actual SAR images is in order: in fact, in actual images, we may not have so many samples over an area presenting the same fractal parameters. This issue is handled in the next chapter.

References

[1] B. B. Mandelbrot, J. W. Van Ness, “Fractional Brownian motions, fractional noises and applications”, *SIAM Rev.*, vol. 10, no. 4, pp. 422-437, Oct. 1968.

[2] Berry, M. V., and Z. V. Lewis. 1980. “On the Weierstrass-Mandelbrot Fractal Function.” Proc R Soc London, Sect A 370:459–484.

[3] G. Franceschetti, M. Migliaccio, D. Riccio, G. Schirinzi, "SARAS: a SAR Raw Signal Simulator", *IEEE Trans. Geosci. Remote Sens.*, vol. 30, no. 1, pp. 110-123, Jan.1992.

[4] G. Franceschetti, D. Riccio, *Scattering, Natural Surfaces and Fractals*. Academic Press, Burlington (MA), USA, 2007.

[5] G. Franceschetti, A. Iodice, and D. Riccio, “Fractal models for scattering from natural surfaces,” in *Scattering*, R. Pike and P. Sabatier, Eds. London, U.K.: Academic, Sep. 2001, pp. 467–485.

[6] A. Papoulis, *Probability, Random Variables and Stochastic Processes*, McGraw-Hill, New York, USA, 1991

[7] S. M. Kay, Modern Spectral Estimation. Englewood Cliffs, NJ: Prentice- Hall, 1988.

[8] T. Austin, A. W. England, G. H. Wakefield, “Special problems in the estimation of power-law spectra as applied to topographical modeling”, IEEE Trans. Geosci. Remote Sens., vol. 32, no. 4, pp. 928-939, July 1994.

Chapter 5

Fractal parameters estimation

In this chapter the extraction of the fractal parameters univocally representing an fBm surface, the fractal dimension *D* and the increment standard deviation *s*, directly from a SAR image is treated [1], [2]. In Chapter 3 and 4 the theoretical evaluation and the spectral estimation of the PSDs of range and azimuth cuts of the image have been discussed. In particular, it has been shown that the spectrum of a SAR image range cut, in an appropriate range of spatial frequencies, presents a power-law behavior. Hence, in a logarithmic plane, the image range spectrum holds a linear behavior with a slope related to the fractal dimension (equivalently the Hurst coefficient) of the imaged surface (cf. Section 3.4), thus allowing linear regression techniques for its retrieving. A large numerical setup on the subject, that shows the goodness of the implemented method, is provided

Furthermore, preliminary results relevant to the increment standard deviation *s* extraction are discussed in this chapter. The *s* retrieving is not a trivial task as it is linked to the amplitude of the log – log spectrum of a SAR image range cut that depends on several parameters besides *s*. A theoretic treatment directed to the separation of *s* from the other parameters is hereafter presented, together with the corresponding experimental results [3].

In the second part of this chapter an algorithm providing the fractal dimension map, i.e. the map of the point by point *D* estimated starting from a single SAR image is presented. Also in this case a wide numerical setup, carried out using simulated SAR images for validation purposes, is provided.

5.1 Fractal dimension estimation

Taking into account the results presented in Section 3 and 4 pertaining to the range cut PSD of a SAR image, the fractal dimension retrieving comes as a consequence. As a matter of fact, being this spectrum linear in a logarithmic plane, with a slope related to the fractal dimension of the imaged surface (see section 3.4), the latter can be estimated via linear regression techniques on the spectrum estimated starting from the SAR image [1]. In the following subsection, a parametric study directed to the analysis of the best setting of the Capon filtering ([4], [5]) for the fractal dimension estimation, both for 1000 samples-cuts and 50 samples-cut (i.e. very small data segment) is provided.

5.1.1 Capon filtering analysis for *D* estimation

Starting from the consideration about the spectral estimation of Section 4.2.1, in this subsection, a parametric study directed to the analysis of the better length p, to be used for the Capon filtering, is performed [6].
A key point of the spectral estimation is the dimension of the data segment on which the estimation is performed. First, 1000 pixel-cuts are used for the D extraction. Depending on the chosen Capon filter length, a different number of the original available samples is used, so this case allows us to understand which is the optimal value for the parameter p.
In the following, significant results relevant to the fractal dimension extraction from simulated SAR images (simulated via SARAS simulator [7]) of fractal surfaces with the same value of s=0.1 [m^{1-H}] and different values of the Hurst coefficient: D=2.3, D=2.2, D=2.1, is shown. For all the three cases the results relevant to the application of the Capon spectral estimation in the case of:

— no filtering (Tab. 5.1)
— length of filtering = 0.3**N* (Tab. 5.2)
— length of filtering = 0.1**N* (Tab. 5.3)

are presented, where N is the number of samples of the range cut of the image. In all cases an anti-aliasing filtering is performed on the estimated spectra, that consists in discarding the frequencies greater than $f_s/2$.

Furthermore, two different linear regression techniques have been investigated:

— *linfit*: minimization of the chi-square error statistic

— *ladfit*: "robust" least absolute deviation method

in order to compare the performances. Just for the sake of brevity, only the results relevant to the *linfit* case, which is the one that perform the better estimation in all the cases, are presented. Besides, the *linfit* procedure allows the evaluation of the unreduced chi-square goodness-of-fit statistic, whose values are also reported in Tab. 5.1-5.3. The obtained estimated samples of the spectra are shown in Fig. 5.1(A-I) compared with the theoretical ones.

TABLE 5.1
NO FILTERING CASE APPLIED TO A 1000 PIXELS SAR IMAGE

	s [m^{1-H}]	D	estimated D	chi-square
Fig. 5 (A)	0.1	2.3	2.27	3.87
Fig. 5 (B)	0.1	2.2	2.17	2.60
Fig. 5 (C)	0.1	2.1	2.11	1.74

TABLE 5.2
CAPON FILTERING OF LENGTH 0.3**N* (LENGTH=300 SAMPLES)

	s [m^{1-H}]	D	estimated D	chi-square
Fig. 5 (D)	0.1	2.3	2.27	2.5
Fig. 5 (E)	0.1	2.2	2.17	1.71
Fig. 5 (F)	0.1	2.1	2.1	1.32

TABLE 5.3
CAPON FILTERING OF LENGTH 0.1**N* (LENGTH=100 SAMPLES)

	s [m^{1-H}]	D	estimated D	chi-square
Fig. 5 (G)	0.1	2.3	2.25	1.22
Fig. 5 (H)	0.1	2.2	2.15	0.73
Fig. 5 (I)	0.1	2.1	2.08	0.69

(A)

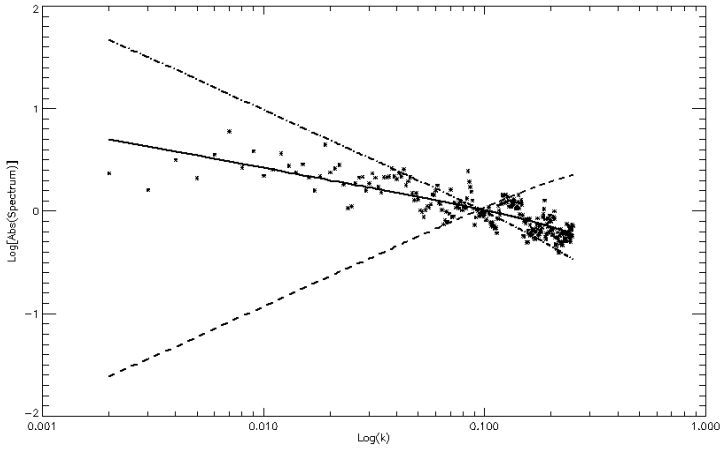
Log[Abs(Spectrum)]
Log(k)
2
1
0
−1
−2
0.001
0.010
0.100
1.000

(B)

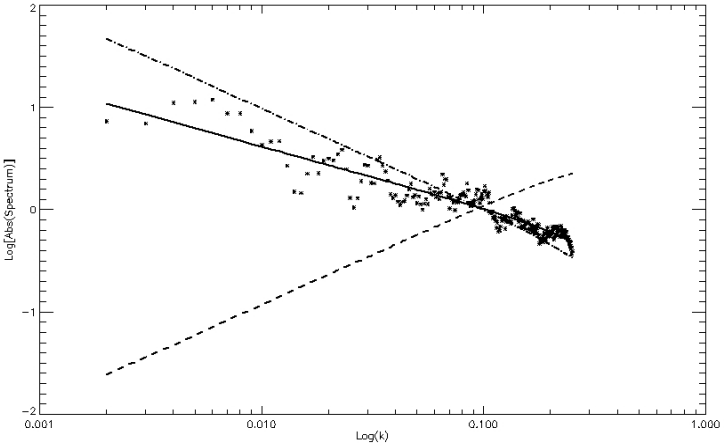
Log[Abs(Spectrum)]
Log(k)
2
1
0
−1
−2
0.001
0.010
0.100
1.000

(C)

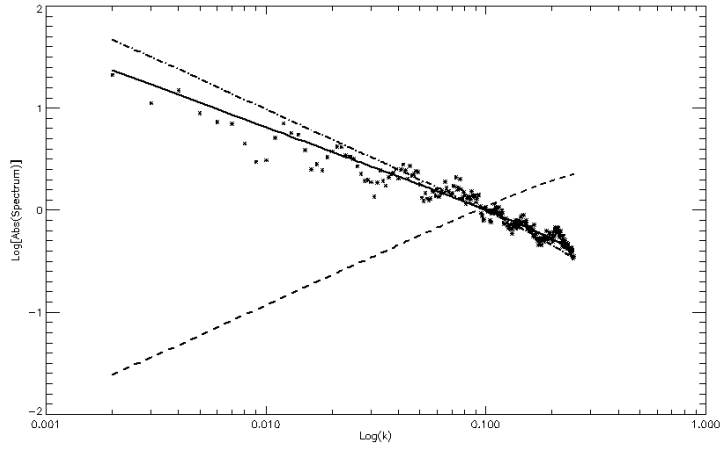
Log[Abs(Spectrum)]
Log(k)
2
1
0
−1
−2
0.001
0.010
0.100
1.000

(D)

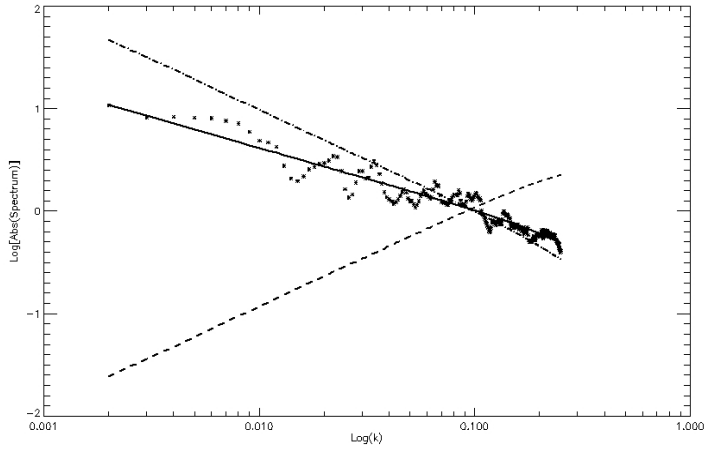
Log[Abs(Spectrum)]
Log(k)
2
1
0
−1
−2
0.001
0.010
0.100
1.000

(E)

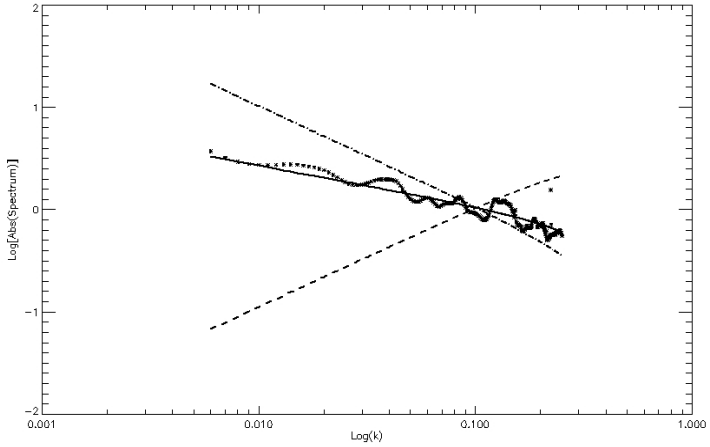
Log[Abs(Spectrum)]
Log(k)
2
1
0
−1
−2
0.001
0.010
0.100
1.000

(F)

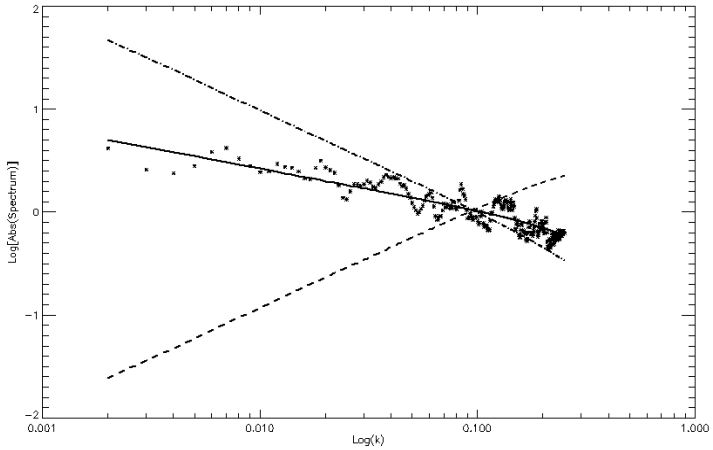
Log[Abs(Spectrum)]
Log(k)
2
1
0
−1
−2
0.001
0.010
0.100
1.000

(G)

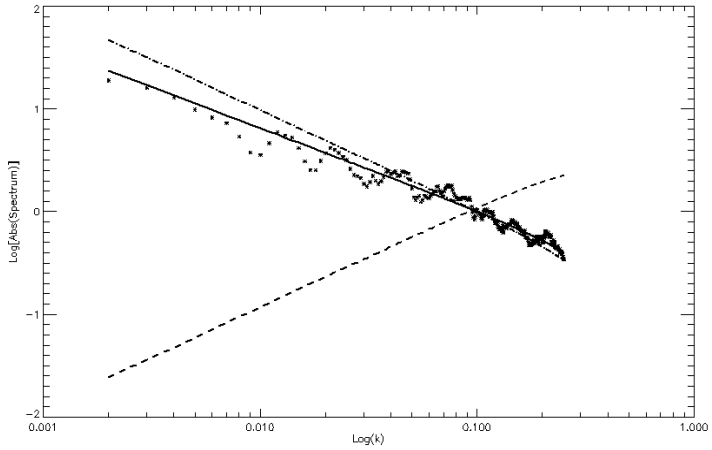

(H)

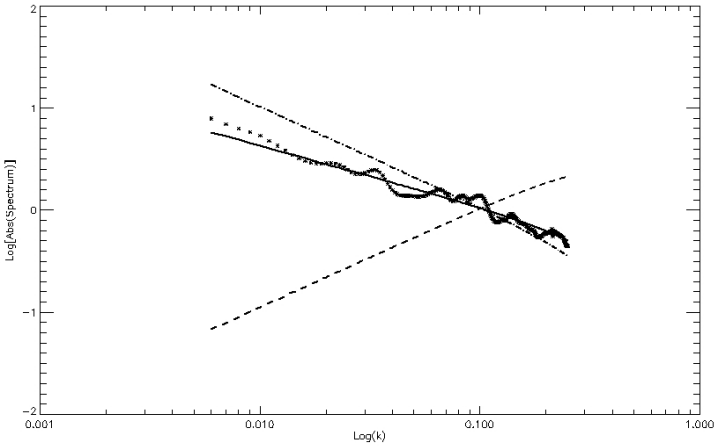

(I)

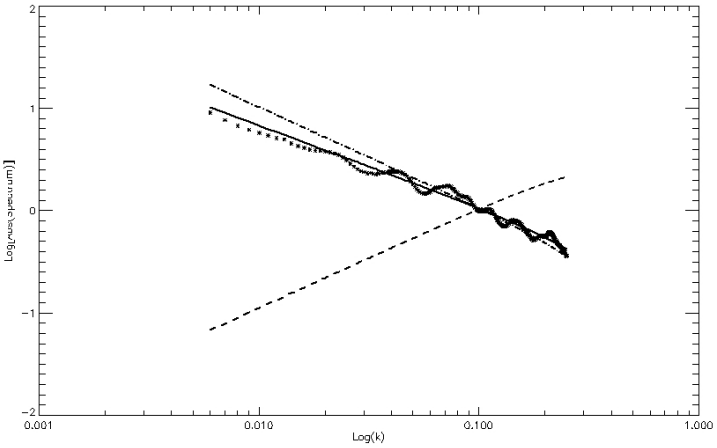

Fig. 5.1: Estimated (samples) and theoretical (continue lines) PSDs of a 1000

pixels range cut of a SAR image of a surface whose fractal parameters are given in Tab.5.1-5.3. The dashed lines delimit the range of slopes of a fractal.

From the results in Tab. 5.1-5.3, it can be deduced that the best estimation is performed when the Capon estimator is applied with a filter length equal to 0.3**N*. Besides, it is worth stressing that, even if the chi-square is reduced when the filter length decreases, the bias increases and so the estimate worsens.
The analysis of these results shows that, as far as the hypothesis of small slopes of the surface is valid, the performance of the retrieving technique is definitely good, while it starts to get worse when the aforementioned hypothesis begins to fail. More precisely, the retrieving techniques are efficient because the estimated *D* values are so close to the actual ones to allow the discrimination of slightly different (in terms of *D*) surfaces from their radar images.

5.1.2 Capon filtering analysis for the fractal dimension estimation in case of small data segments.

In order to implement the fractal dimension extraction starting from actual SAR images, the problem of analyzing very small areas in which the fractal parameters can be considered constant must be investigated [6]. Hence, in this subsection, the linear regression is applied to range cuts of 50 pixels of the SAR images considered in the previous sub-section. Obviously, in this case, there are very few samples available to perform the spectrum estimation, so the results of the retrieving technique are not so good as in the previous case. In Tab. 5.4-5.6 the results relevant to the estimation performed without the Capon filtering, with a Capon filtering with p=0.3**N* (filter length=15 samples) and with p=0.1**N* (filter length=5 samples) are shown, with N=50. Note that the estimated values in Tab. 5.4-5.6 are averaged on several elaboration windows taken from different areas of each simulated image.

TABLE 5.4
NO FILTERING CASE APPLIED TO A 50 PIXELS SAR IMAGE CUT-OUT

s [m^{1-H}]	D	estimated D	chi-square
0.1	2.3	2.26	0.17
0.1	2.2	2.15	0.14
0.1	2.1	2.14	0.18

TABLE 5.5
CAPON FILTERING OF LENGTH 0.3**N* (LENGTH=15 SAMPLES)

	s [m^{1-H}]	D	estimated D	chi-square
Fig. 5.2 (A)	0.1	2.3	2.26	0.06
Fig. 5.2 (B)	0.1	2.2	2.16	0.05
Fig. 5.2 (C)	0.1	2.1	2.08	0.08

TABLE 5.6
CAPON FILTERING OF LENGTH 0.1**N* (LENGTH=5 SAMPLES)

s [m^{1-H}]	D	estimated D	chi-square
0.1	2.3	2.19	0.002
0.1	2.2	2.13	0.002
0.1	2.1	2.07	0.001

For the sake of brevity, hereafter only the plots of the range cut PSDs relevant to the case of the best filtering, i.e. p=0.3**N*, are presented. It is worth stressing that, due to the Capon filtering and then to the antialiasing filtering performed on an already short data segment, the number of samples on which the spectrum estimation is performed is significantly reduced. In Fig. 5.2, the PSDs relevant to the results in Tab. 5.5 are shown: in this case the number of samples used for the estimation is equal to 11.

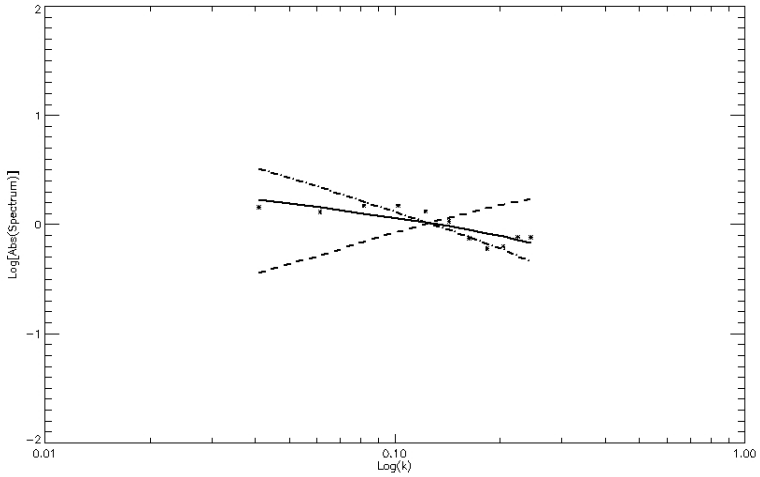
Log[Abs(Spectrum)]
2
1
0
−1
−2
0.01
0.10
1.00
Log(k)

(A)

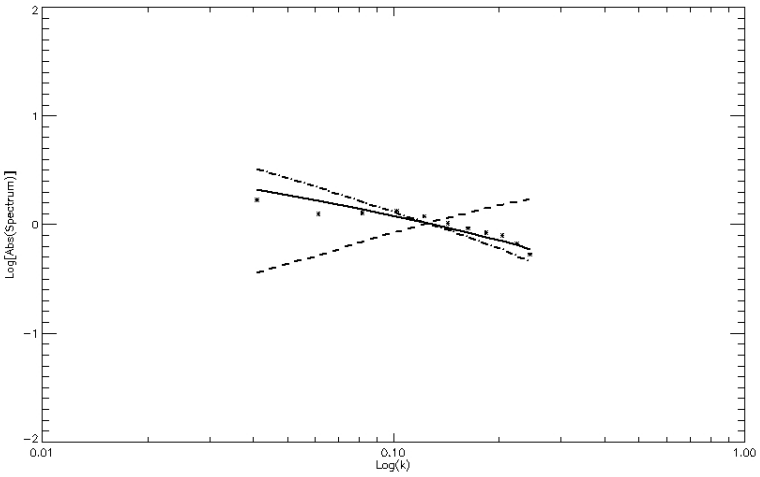
Log[Abs(Spectrum)]
2
1
0
−1
−2
0.01
0.10
1.00
Log(k)

(B)

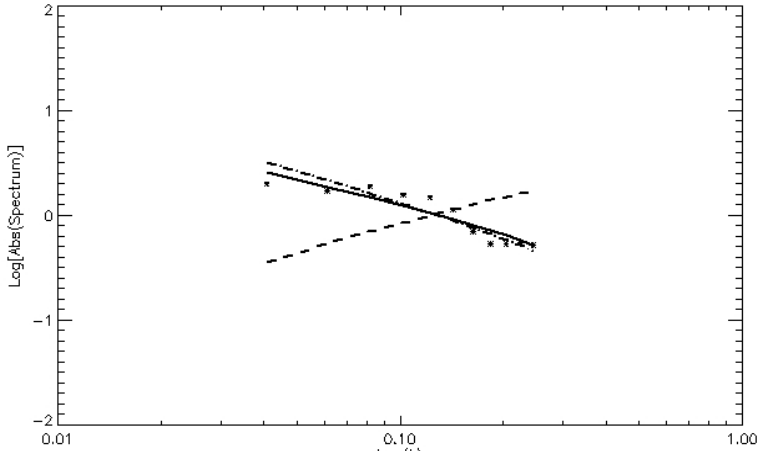

(C)

Fig. 5.2 (A-C): Estimated (samples) and theoretical (continue lines) PSDs of a range cut of a 50 pixels cut of a SAR image of a surface of fractal parameters given in Tab.5.5. The dashed lines delimit the range of slopes of a fractal.

Obviously, due to the small number of samples used for the estimation, the results relevant to small data segments (Tab. 5.4-5.6) are generally worse than the results of the previous section (Tab. 5.1-5.3). Nevertheless, also for small data segments, the best filter length is equal to 0.3**N*. Moreover, the trend of the results in Tab. 5.4-5.6 is the same of that in Tab. 5.1-5.3: the chi-square decreases if the filter length increase, but the bias increases too, so, for the cases at hand, it is not convenient to use a filter length smaller than 0.3**N*.

5.2 Relative standard increment deviation retrieving

The retrieving of the second fractal parameter, the increment standard deviation s [m^{1-H}] (cf. Section 2.3, [8], [9]) - starting from Eq. (3.44) and taking into account the asymptotical evaluation of the reflectivity spectrum in Eq. (3.24) - is more involved with respect to the fractal dimension case. Actually, in this case, if the linear regression is enforced to extract the s value, this value will be retrieved from the

intercept, i.e. from a single value extremely influenced by the spectrum slope estimate. Thus, the s estimate would be completely dependent on the goodness of the estimate of the other fractal parameter. Moreover, the SAR image power spectrum amplitude can depend not only on the amplitude coefficient of Eq. (3.44), but also on calibration parameters of the specific sensor that cannot be always known and controlled. For this reason, in the following preliminary analysis, the extraction of a relative value of *s,* that is retrieved considering the ratio of two SAR image power spectra according to the theoretical and analytical considerations of the following sections, is investigated [3].

5.2.1 Theoretical framework

Let us recall, in extended way, the expression of the PSD of the range cut of SAR images of fractal surfaces:

$$W_i(k_y) = a_1^2 s^2 \Gamma(1+2H) sen(\pi H) \frac{1}{|k_y|^{2H-1}} \text{rect}\left[\frac{\Delta y \sin^2\theta_0\, k_y}{\pi}\right] = S_0^i |k_y|^{-\alpha^i} \text{rect}\left[\frac{\Delta y \sin^2\theta_0\, k_y}{\pi}\right], \quad (5.1)$$

wherein a_1, as stated in Eq. (3.43), is:

$$a_1 = \sqrt{\frac{S_0 \kappa^{1-2H} |\beta_{mn}|^2}{2^{2H}}} \cos\theta_0 \sin^{-H}\theta_0 \times [2 + (1+H)\cos^2\theta_0 \sin^{-2}\theta_0]. \quad (5.2)$$

with S_0 given in Eq. (2.20). As Eq. (5.1) and (5.2) show, the spectral amplitude of the range cut SAR image PSD, S_0^i, depends on several parameters; including θ_0 and κ that are known and depend on the sensor characteristics, k_y that depends on the spatial frequencies and is calculable and *H,* the Hurst coefficient, that can be preliminarily estimated with the linear regression discussed in the previous paragraph. Further incidental calibration coefficients that modify the

spectral amplitude are assumed to be constant for SAR images acquired by the same sensor. According to these considerations it can be considered the ratio between two SAR image PSDs. Substituting Eq. (5.2) and Eq. (2.20) in Eq. (5.1), it turns out:

$$\frac{W_{i1}(k_y)}{W_{i2}(k_y)} = \frac{{s_1}^4 2{\kappa_1}^{1-2H_1}\Gamma^2(1+H_1)\sin^2(\pi H_1)}{{s_2}^4 2{\kappa_2}^{1-2H_2}\Gamma^2(1+H_2)\sin^2(\pi H_2)} \times$$

$$\frac{\cos^2\theta_{01}\,\sin^{-2H_1}\theta_{01}[2+(1+H_1)\cos^2\theta_{01}\,\sin^{-2}\theta_{01}]^2\,\dfrac{1}{|k_y|^{2H_1-1}}}{\cos^2\theta_{02}\,\sin^{-2H_2}\theta_{02}[2+(1+H_2)\cos^2\theta_{02}\,\sin^{-2}\theta_{02}]^2\,\dfrac{1}{|k_y|^{2H_2-1}}} =$$

$$= \frac{{s_1}^4}{{s_2}^4} \cdot \mathrm{M}(\kappa_1, \kappa_2, H_1, H_2, \theta_{01}, \theta_{02}, k_y) \qquad (5.3)$$

wherein $M(\cdot)$ is a multiplicative function. If we are considering power spectra of SAR images acquired by the same sensor (or of different cuts of the same SAR image) the sensor parameters and the wavenumber κ are the same, so Eq. (5.3) turns into:

$$\frac{W_{i1}(k_y)}{W_{i2}(k_y)} = \frac{{s_1}^4}{{s_2}^4} \cdot \mathrm{M}(\kappa, \theta_0, k_y, H_1, H_2) \qquad (5.4)$$

Therefore the estimation of the increment standard deviation *s,* in relative, with respect to a controlled value of *s*, can be performed after estimating the PSDs of the SAR image of the region of interest and after estimating, trough the last ones, the Hurst coefficients $H_1$and H_2, as follows:

$$s_1 = s_2 \left(\frac{W_{i1}(k_y)}{W_{i1}(k_y)} \cdot \frac{1}{\mathrm{M}(\kappa, \theta_0, k_y, H_1, H_2)} \right)^{\frac{1}{4}}$$

5.2.2 Numerical setup

In order to validate the theoretical analysis presented in the previous section, the *s* parameter extraction is performed, as done for the *D*, on couple of canonical SAR images obtained starting from synthesized fractal surface of known and different fractal parameters (cf. Section 4.1, [7]). The spectra $W_{i1}(k_y)$ and $W_{i2}(k_y)$ are estimated using the Capon estimator widely discussed in Sections 4.2 and 5.1 [5]. Then, performing a linear regression on these PSDs, the Hurst coefficient *H* of the SAR image is retrieved. Therefore, the multiplicative factor of Eq. (5.4) can be calculated and - through Eq. (5.5) - the ratio of the increment standard deviations of two SAR images of constant and controlled fractal parameters can be evaluated and compared with the theoretical one. Note that, in order to make the estimate more robust, the abovementioned operations (evaluation of the multiplicative factor *M* and calculation of the PSDs ratio) are implemented on the PSDs integrals, so averaging on all the estimated spectra points.
In Figures 5.3-5.6 the theoretical and estimated range cuts PSDs ((A) and (B) respectively) of SAR images of natural surfaces with several fractal parameters are represented. The starting SAR iamges have 1000x1000 pixels dimensions and the same fractal parameters at all scales of interest. In particular, cases of SAR images of fractal surfaces having:

- same Hurst coefficient and different increment standard deviations (Fig. 5.3)
- same increment standard deviation and different Hurst coefficients (Fig. 5.4)
- different Hurst coefficients and different increment standard deviations (Fig. 5.5, 5.6)

are considered. The results relevant to the fractal parameters *s* and *H* estimations are given in Table 5.7.

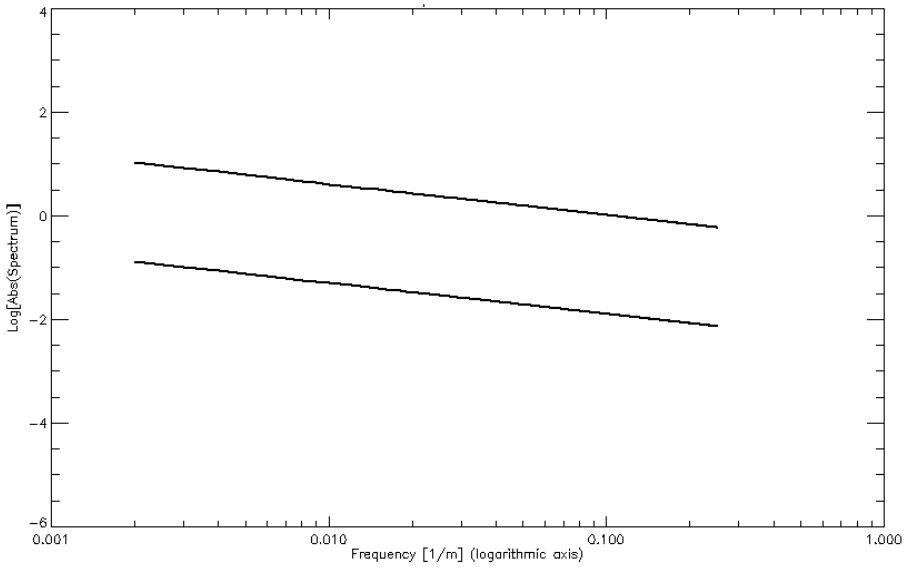

(A)

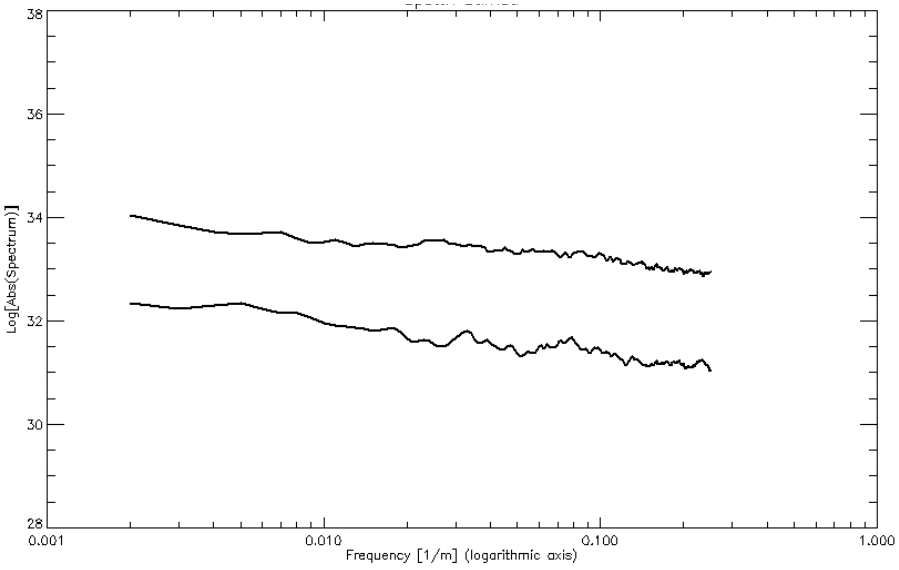

(B)

Figure 5.3. Theoretical (A) and estimated (B) spectra relevant to SAR Images of surfaces having the following fractal parameters: $H_1 = H_2 = 0.8$, $s_1 = 0.3\ m^{0.2}$, $s_2 = 0.1\ m^{0.2}$

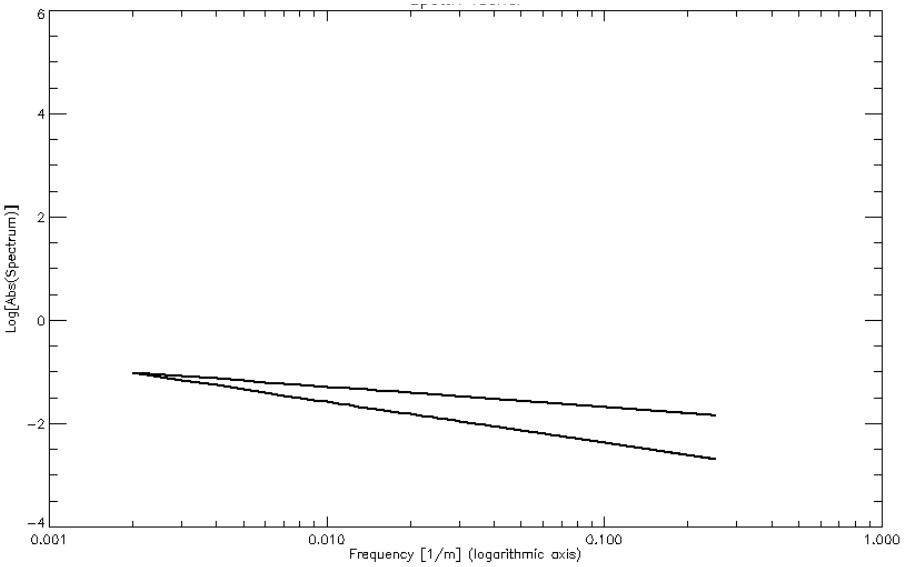

(A)

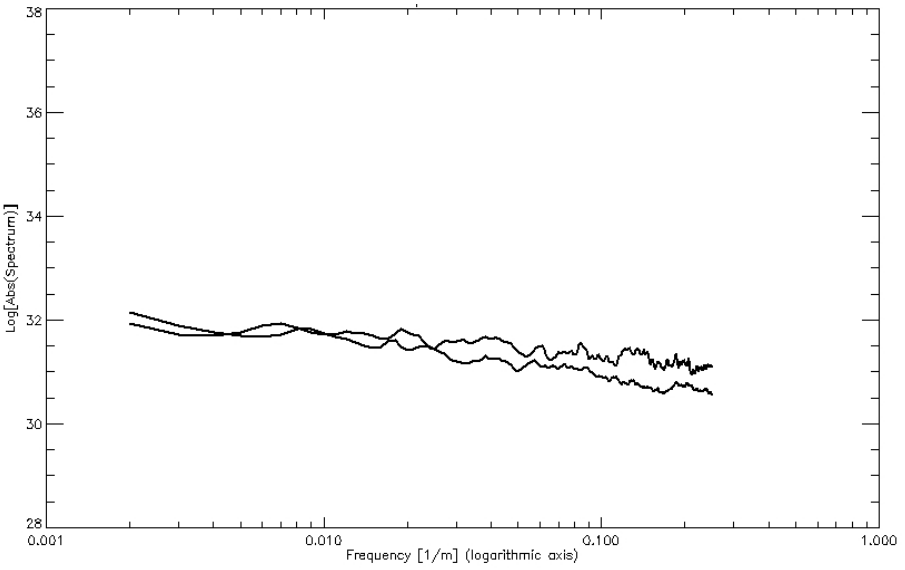

(B)

Figure 5.4: Theoretical (A) and estimated (B) spectra relevant to SAR Images of surfaces having the following fractal parameters: $H_1 = 0.9$, $H_2 = 0.7$, $s_1 = 0.1\ m^{0.1}$, $s_2 = 0.1\ m^{0.3}$

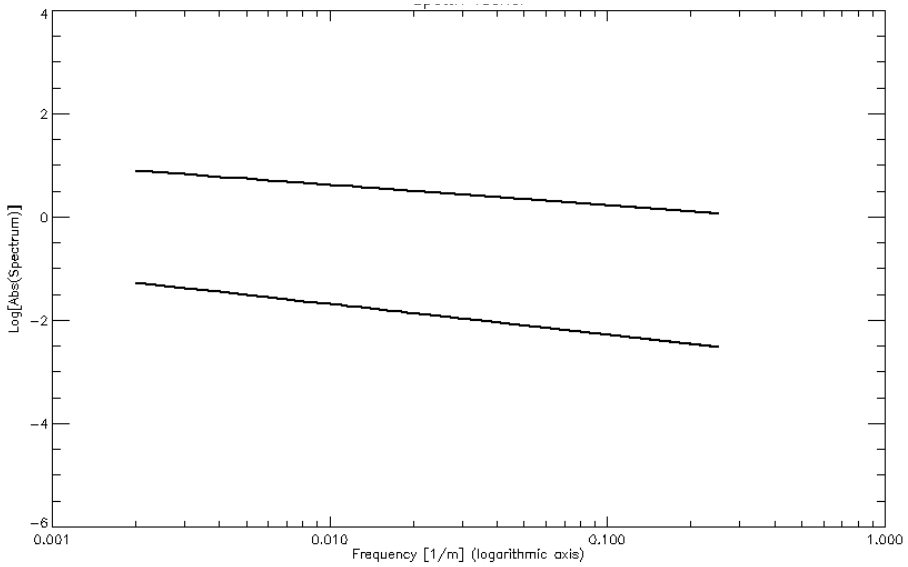

(A)

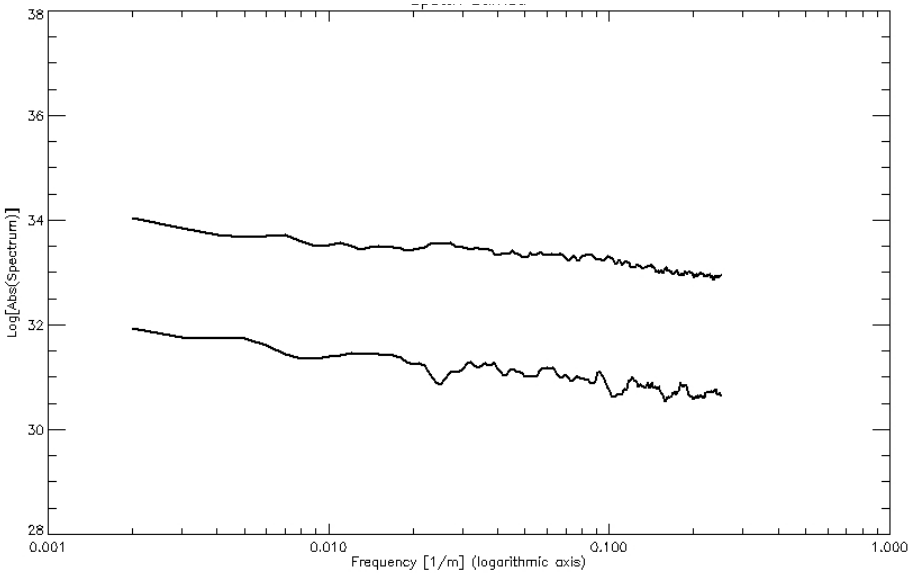

(B)

Figure 5.5: Theoretical (A) and estimated (B) spectra relevant to SAR Images of surfaces having the following fractal parameters: $H_1 = 0.7$, $H_2 = 0.8$, $s_1 = 0.3\ m^{0.3}$, $s_2 = 0.08\ m^{0.2}$

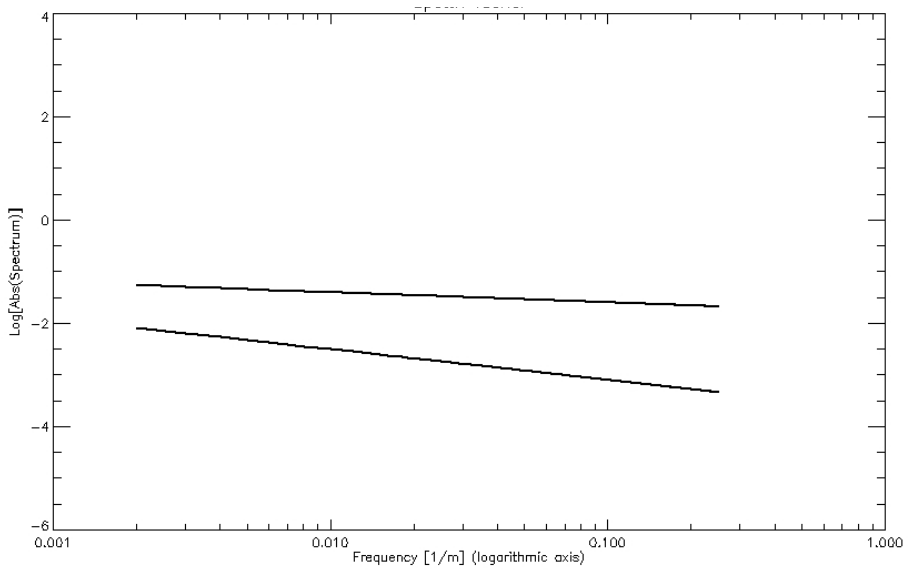

(A)

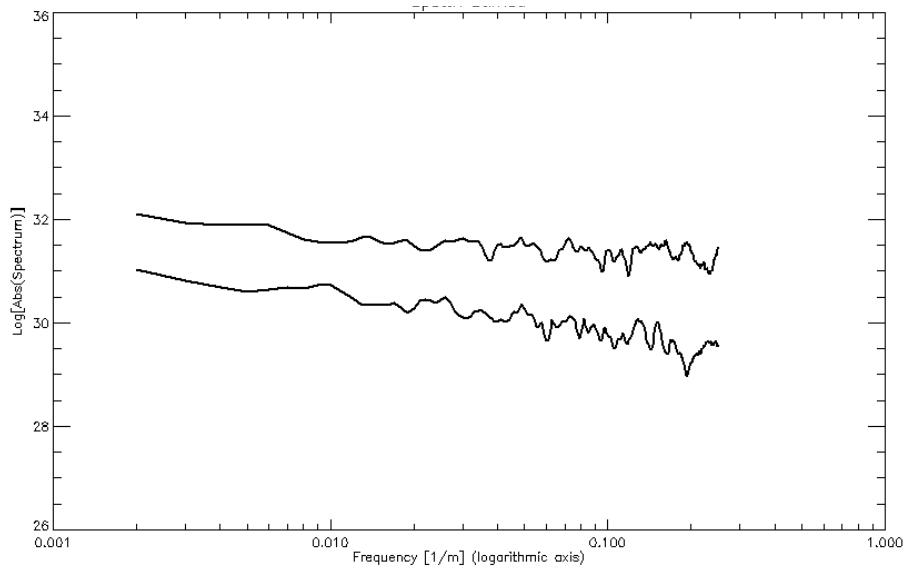

(B)

Figure 5.6. Theoretical (A) and estimated (B) spectra relevant to SAR images of surfaces having the following fractal parameters: $H_1 = 0.6$, $H_2 = 0.8$, $s_1 = 0.1\ m^{0.4}$, $s_2 = 0.05\ m^{0.2}$

Table 5.7
Theoretical and estimated fractal parameters relevant to the PSDs in Fig. 5.3-5.6

		theoretical *s* [m^{1-H}]	**theoretical *H***	**estimated H**	**theoretical *s* ratio [m$^{H_2-H_1}$]**	**estimated *s* ratio [m$^{H_2-H_1}$]**
Fig.5.3	PSD 1	0.3	0.8	0.797	3.000	2.754
	PSD 2	0.1	0.8	0.800		
Fig.5.4	PSD 1	0.1	0.9	0.889	1.000	1.062
	PSD 2	0.1	0.7	0.754		
Fig.5.5	PSD 1	0.3	0.7	0.776	3.750	3.636
	PSD 2	0.08	0.8	0.801		
Fig.5.6	PSD 1	0.1	0.6	0.654	2.000	1.787
	PSD 2	0.05	0.8	0.864		

Besides the presented results, some consideration on the fractal parameters estimation are in order. The *D* (equivalently *H*) retrieving is a very delicate issue as its accuracy is strongly influenced by the number of samples used for the estimation of the spectrum (in the presented cases 1000x1000 sample range profile have been used to validate the theoretical analysis) and as the model goes out of the hypotesis of small slopes regime the *H* estimate becomes worse. The *s* relative estimation, instead, is more robust both with respect to the number of samples used for the spectrum estimation and for the validity limits of the theoretical model. Moreover, and this is a non slight result, the godness of the *s* estimate is not significantly affected by the accuracy of the *H* estimation: also in cases in which the *H* estimation is less accurate (see Fig. 5.4 PSD 2, Fig. 5.5 PSD 1, Fig 5.6 PSD 1, 2) the results on the relative *s* are comparable with the others

5.3 SAR image post-processing for the fractal dimension map generation

In order to apply on actual SAR images the fractal retrieving techniques described in the previous section, some considerations about the extent of the imaged area and so on the number of samples which can be used for the spectrum estimation are required.
In Section 4.2, in order to validate the theoretical results, simulated profiles of 1000 samples, holding the same fractal dimension at all scales, have been considered. Obviously, an actual SAR image of a natural area can present appreciable variations of the fractal dimension over the observed scene. Indeed, the fractal dimension is a local characteristic of the surface and an effective technique for the its retrieving should work on small homogeneous patches of the image. Therefore, in order to obtain a map of the fractal dimension starting from a SAR image, i.e. a matrix of the point by point estimated *D* of the observed scene, a specific algorithm, based on the inversion and estimation logic described in the previous section, has been implemented [1], [2], [10]. The proposed algorithm makes use of a sliding window which, spanning the entire image, performs in each iteration the retrieving of *D* as described in the previous Sub-sections 5.1. The choice both of the sliding window dimensions and of the number of range cut spectra averaged in each window in order to obtain the mean PSD, depends on the specific needs of the user and results from a trade-off between estimation accuracy, computational time and resolution of the output fractal dimension map. As a matter of fact the choice of a larger window allows obtaining a more accurate estimate of the fractal dimension (depending on the number of samples drawn in the range direction) but makes the resolution of the final fractal map worse and increases the computational time. Concerning the number of range cut spectra averaged in each window, the larger this number the better the PSD estimation, even if the computational time increases: in particular, this is true if we assume that all the considered range cuts in the window pertain to the same type of terrain.

5.3.1 Application to simulated SAR images of canonical fractal surfaces

In order to evaluate the performance of this algorithm a test on a canonical fractal case is presented: the algorithm has been applied to a simulated (canonical) speckle-free (corresponding to an infinite number of looks) SAR image obtained as described in the previous section (i.e. providing as input to the simulator a DEM of a surface holding the same fractal parameters at all scales) with several dimensions of the elaboration window. In Fig.5.7 the simulated Envisat image of 1000x1000 pixels of a natural surface with fractal parameters D=2.2, s=0.1 $m^{0.2}$ is shown. In Fig. 5.8, 5.9 and 5.10 the corresponding fractal maps obtained using windows of 51x51 pixels, 35x35 pixels, 21x21 pixels, respectively, are presented. In Table 5.8 the statistics of these fractal maps are summarized: in particular, the mean and the standard deviation of the estimated fractal dimension are provided.

Fig. 5.7: Simulated SAR Image of a canonical surface fractal parameters s=0.1, D=2.2

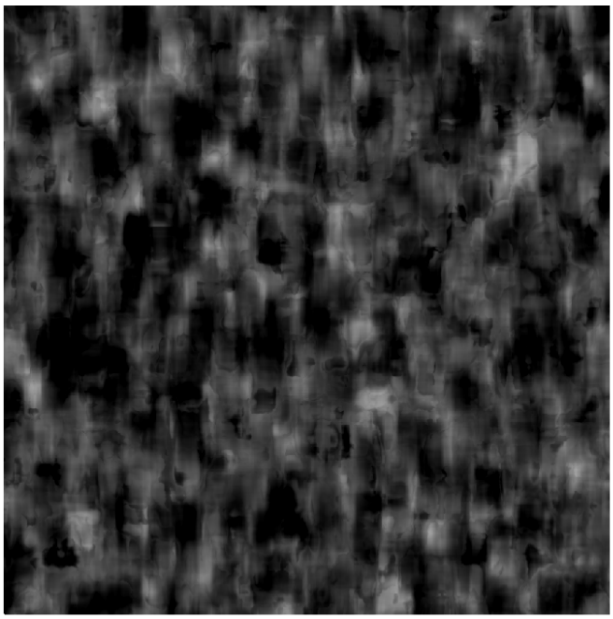

Fig. 5.8: Fractal map relevant to the SAR image in Fig.5.7 obtained with a sliding window of dimension 51x51 pixels

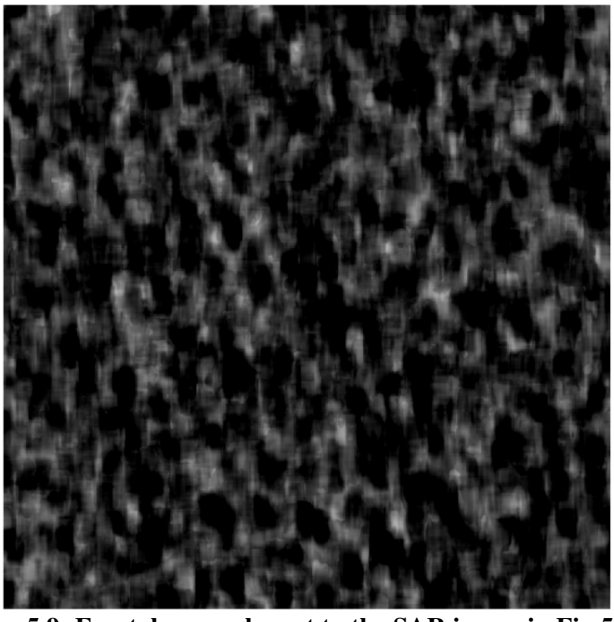

Fig. 5.9: Fractal map relevant to the SAR image in Fig.5.7 obtained with a sliding window of dimension 35x35 pixels

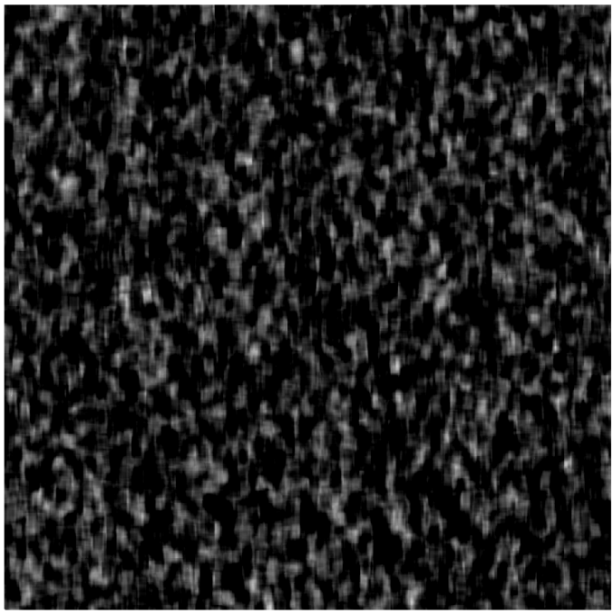

Fig. 5.10: Fractal map relevant to the SAR image in Fig.5.7 obtained with a sliding window of dimension 21x21 pixels

Table 5.8
STATISTICS OF THE FRACTAL MAPS (SPECKLE FREE CASE)

Figure number	Sliding window dimensions	*D* mean	*D* standard deviation
Fig. 5.8	51x51 pixels	2.19	0.13
Fig. 5.9	35x35 pixels	2.11	0.16
Fig.5.10	21x21 pixels	2.06	0.19

Furthermore, in order to evaluate the performance of this type of post-processing on SAR images affected by the speckle phenomenon, the algorithm has been applied to simulated SAR images generated by the SARAS ([7]) and taking into account the speckle effect (cf. Section 1.2, [11], [12]). In this case, a sliding window of 51x51 pixels has been used. As shown in Figs. 5.11-5.14 and summarized in Table 5.9, the presence of speckle does not significantly invalidate the effectiveness of the estimation for the considered cases: in particular, four simulated SAR images have been considered, for which the observed surface presents different values of D and s, as summarized in Table 5.9. As a matter of fact, the presented spectrum estimation

technique performs a sort of intrinsic speckle filtering. First of all, averaging several spectra relevant to range cuts sufficiently spaced in the azimuth direction to be considered uncorrelated, implies a significant mitigation of the speckle effect. Besides, as a result of the anti-aliasing filtering, which consists in discarding the high frequencies components of the spectrum (see Section 4.2.2), the range of frequencies mostly affected by the speckle is discarded.

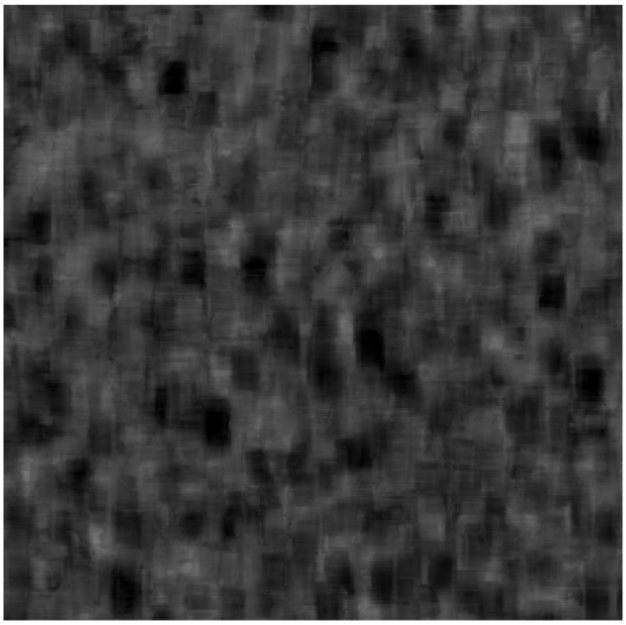

Fig. 5.11: Fractal map relevant to a SAR Image of fractal parameters specified in Table 5.9 in presence of speckle.

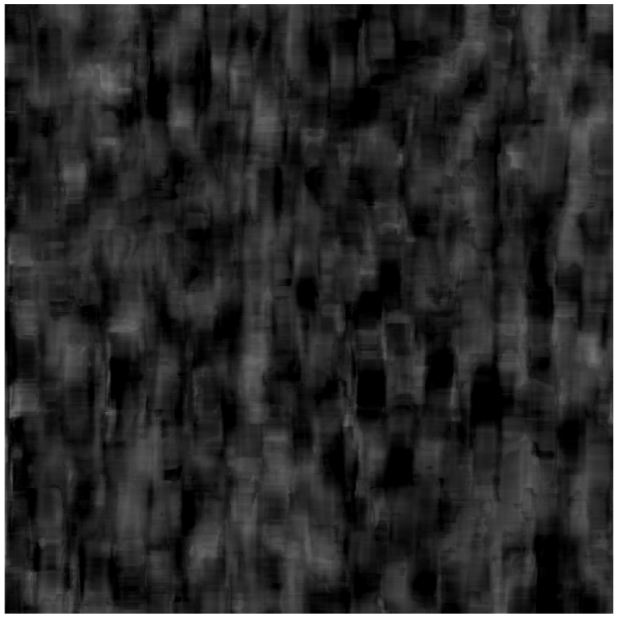

Fig. 5.12: Fractal map relevant to a SAR Image of fractal parameters specified in Table 5.9 in presence of speckle.

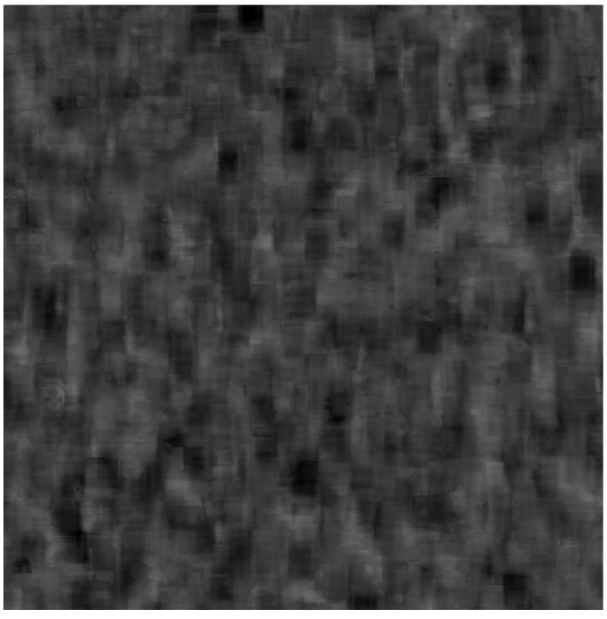

Fig. 5.13: Fractal map relevant to a SAR Image of fractal parameters specified in Table 5.9 in presence of speckle.

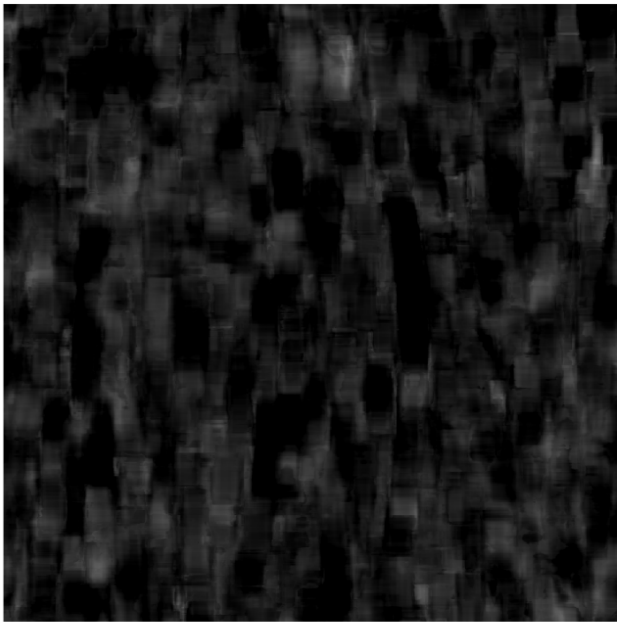

Fig. 5.14: Fractal map relevant to a SAR Image of fractal parameters specified in Table 5.9 in presence of speckle.

Table 5.9
STATISTICS OF THE FRACTAL MAPS (SPECKLE CASE)

Figure number	s [m^{1-H}] of the imaged surface	D of the imaged surface	D mean	D standard deviation
Fig. 5.11	0.3	2.3	2.22	0.07
Fig. 5.12	0.3	2.1	2.14	0.08
Fig. 5.13	0.5	2.3	2.23	0.06
Fig. 5.14	0.5	2.1	2.08	0.08

5.3.2 Behavior in presence of man-made structures

Contrary to natural surfaces that can be effectively described using fractal models, ([8], [9]), man-made objects does not show a fractal behavior, at least at scales ranging from the sensor resolution one and

that of the microwave electromagnetic field wavelength. Thus, a geometric description in the context of Euclidean geometry is in order [13]. From a fractal point of view this means that they show a non-fractional dimension and, hence, at least in principle, they should be clearly separable from fractal objects in SAR images.

In this subsection the behavior of the SAR image fractal processing described in the previous one, in presence of urban features is investigated [14]. These latter produce the appearance on the image of very bright characteristics, determining strong discontinuities in the radar signal. This is due to the presence of multiple scattering contributions, mainly generated by the dihedral configuration of soil and building walls [13]. The presence of discontinuities affects strongly the behavior of the fractal processing, whose rationale is based on the evaluation of the image spectrum.

To investigate the behavior of the fractal filter in presence of multiple reflection contributions, SAR images simulated (by means of SARAS simulator [7]) superimposing to the reflectivity relevant to a fractal DEM, with prescribed fractal parameters, three fifty-pixels-long bright lines and one bright point, presenting all the same intensity (Fig. 5.15).

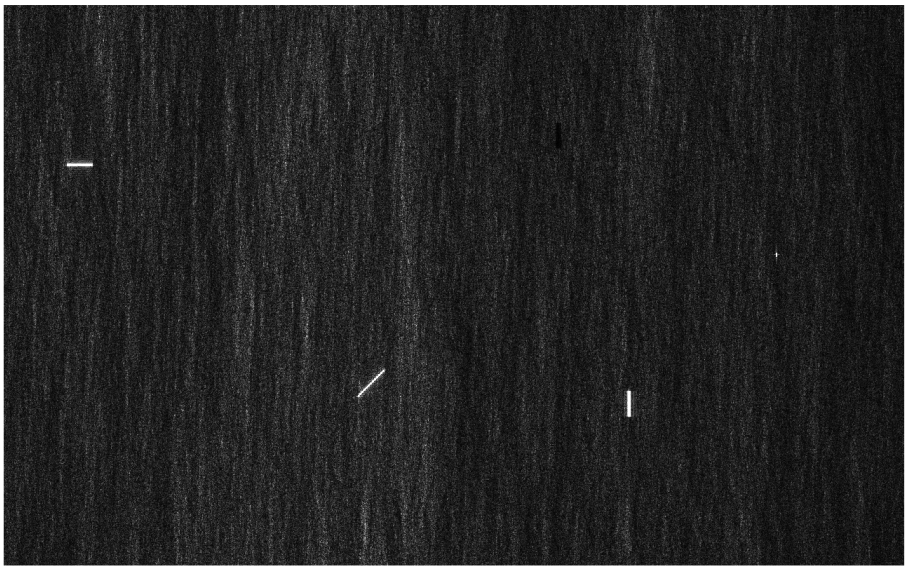

Figure 5.15: Simulated SAR image.

In Fig. 5.16 and 5.17 two filtered versions of the test image, obtained with elaboration windows of dimensions 35x35 pixels and 71x71pixels respectively, are shown. First of all, it is evident that the dimensions of the geometric features relevant to the bright objects depend on the sliding window dimension. Some quantitative considerations are in order. In both Fig. 5.16 and 5.17, the presence of the isolated bright point does not significantly affect the fractal map. At the right side of the figures there is a square window of the same dimension of the elaboration window presenting a constant fractal dimension. Such a phenomenon depends on the fact that the level of spectrum distortion due to the presence of a single non fractal point in a whole range line (whose length depends on the range-sliding window dimension) that is also averaged with a number of fractal spectra (the number of these spectra depending on the azimuth-sliding window dimension), does not significantly alter the fractality of the area covered by the window. The vertical bright line produces in both cases a rectangle showing a width equal to that of the used sliding window, and a length equal to that of the line summed to the length of the sliding window. The rectangle turns out to be dark with respect to the background, in fact it presents quite constant values of fractal dimension lower than 2: in this case a brilliant point is present in several range lines in the same sliding windows, so the averaged spectrum is finally non-fractal. As a matter of fact, the algorithm perfectly retrieves the non fractal object, and its length can be exactly deduced. A very similar effect is that produced by the oblique line. In both Fig. 5.16 and 5.17 we can see an hexagon due to the dragging of a window (whose dimensions are those of the elaboration window) for all the length of the starting oblique line The most evident difference between the two images is due to the processing of the horizontal bright line, which, anyway, cannot be related to double reflection contributions, but shows an interesting behavior of the filtering. In Fig 5.16 the filtering produces two side by side square windows having the same dimension of the sliding window, spaced out 15 pixels. This phenomenon depends on the fact that a sliding window smaller than the line in the range direction has been used. This implies that, for a distance equal to the length of the horizontal bright line minus the range dimension of the sliding window, during the processing, there is a constant bright line spanning all the elaboration window extension, whose spectrum, averaged with those of the other range lines present in the windows, does not produce

any distortion. This effect does not occur in Fig.5.17, where the size of the elaboration window is greater than that of the bright line. In this case, we have a 71 pixels-long and 121-pixels wide rectangle (the range dimension is given by the sum of the window size and of the bright line length).

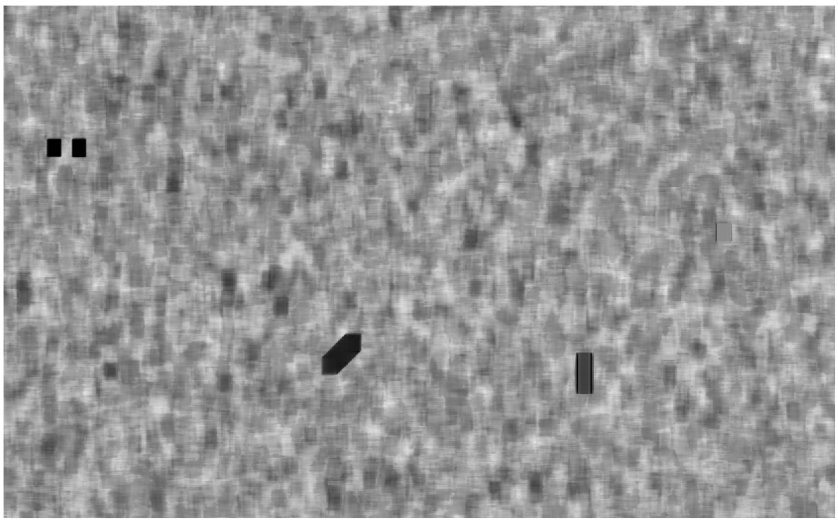

Figure 5.16: Fractal map relevant to the SAR image in Fig. 5.15 obtained using a 35x35 pixels sliding window

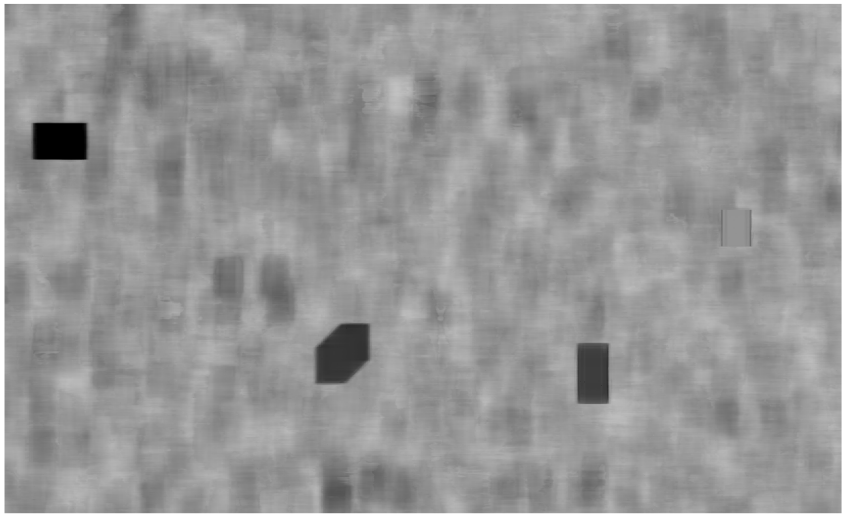

Figure 5.17: Fractal map relevant to the SAR image in Fig. 5.15 obtained using a 71x71 pixels sliding window

In conclusion, the above presented test simulation shows how the fractal processing, operating on a single (amplitude) SAR image, recognizes automatically non-fractal features and how it is possible to retrieve the dimension of such objects taking into account the sliding window dimensions [14].

References

[1] G. Di Martino, D. Riccio and I. Zinno, "SAR Imaging of Fractal Surfaces", IEEE Trans. Geosci. Remote Sens., in print, available on IEEE Early Access.

[2] G. Di Martino, A. Iodice, D. Riccio, G. Ruello and I. Zinno, "Fractal Based Filtering of SAR Images", Proceedings IGARSS 2010, Honolulu (USA), July 2010, pp. 2984-2987.

[3] D. Riccio, I. Zinno, G. Di Martino and G. Ruello, "SAR image post-processing for the estimation of fractal parameters", Proceedings SPIE 2011, Prague (Czech Republic), September 2011, accepted for publication.

[4] S. M. Kay, *Modern Spectral Estimation*. Englewood Cliffs, NJ: Prentice- Hall, 1988.

[5] T. Austin, A. W. England, G. H. Wakefield, "Special problems in

the estimation of power-law spectra as applied to topographical modeling", IEEE Trans. Geosci. Remote Sens., vol. 32, no. 4, pp. 928-939, July 1994.

[6] G. Di Martino, G. Franceschetti, D. Riccio and I. Zinno, "Spectral processing for the extraction of fractal parameters from SAR data", Proceedings of Digital Signal Processing 2011, Corfu (Greece), July 2011, accepted for publication.

[7] G. Franceschetti, M. Migliaccio, D. Riccio, G. Schirinzi, "SARAS: a SAR Raw Signal Simulator", *IEEE Trans. Geosci. Remote Sens.*, vol. 30, no. 1, pp. 110-123, Jan.1992.

[8] B. B. Mandelbrot, J. W. Van Ness, "Fractional Brownian motions, fractional noises and applications", *SIAM Rev.*, vol. 10, no. 4, pp. 422-437, Oct. 1968.

[9] G. Franceschetti, D. Riccio, Scattering, *Natural Surfaces and Fractals*. Academic Press, Burlington (MA), USA, 2007

[10] I. Zinno, G. Di Martino, A. Iodice, G. Ruello and D. Riccio, "Estimation of natural surfaces parameters from TerraSAR data", Proceedings 4th TerraSAR-X Science Team Meeting, Munich (Germany), February 2011, pp 1-7.

[11] G.Franceschetti and R.Lanari; *Synthetic Aperture Radar Processing*, CRC PRESS, New York, 1999.

[12] C. Oliver, S. Quegan, *Understanding Synthetic Aperture Radar Images*, Scitech Publishing Inc., Reileigh (USA), 2004

[13] G. Franceschetti, A. Iodice, D. Riccio, G. Ruello, "SAR Raw Signal Simulation for Urban Structures", IEEE Trans. Geosci. Remote Sens.,vol.41, n.9, pp. 1986-1995, September 2003.

[14] G. Di Martino, A. Iodice, D. Riccio, G. Ruello and I. Zinno, "Fractal Filtering Applied to SAR Images of Urban Areas", Proceedings of Joint Urban Remote Sensing Event 2011, Munich (Germany), April 2011, pp. 261-264.

Chapter 6

Fractal processing of actual SAR images

In this chapter some significant study cases relevant to the application of the fractal processing [1] described in Section 5.3 to actual SAR images are presented. Depending on the objective of the specific application at issue, fractal maps of SAR images can be used for different types of analysis of the scene observed by the sensor. The automatic separation between urban objects and natural areas, the interpretation of geomorphologic features of geological formations, the detection of changes from SAR images of the same area acquired in different times are examples of the possible analysis to perform. In this chapter, four different study cases are investigated, that not only exemplify diverse types of applications, but also illustrate the goodness of the processing operation on different types of SAR images (acquiring sensor, operational mode, resolution).

In the first section the fractal processing is used in order to distinguish - in a complete automatic way, working on a single SAR image - urban areas from natural ones.

In Section 6.2 the fractal processing is applied to a TerraSAR-X stripmap image of the Somma - Vesuvius volcanic complex and the relevant results are compared with those obtained starting from a Digital Elevation Model (DEM) of the scene at issue [2].

In Section 6.3 a fractal-based analysis for the seismic damage estimation in urban areas, performed working on COSMO-SkyMed spotlight (very high resolution) images is presented. Finally, in Section 6.4, preliminary results on the application of the fractal processing for the relative standard increment deviation s [m^{1-H}] retrieving are shown.

6.1 Fractal analysis of SAR images: the case of Somma-Vesuvius volcanic complex

In this section the results of the application of the processing described in Section 5.3 to a SAR image of the Somma - Vesuvius volcanic complex (close to Naples in Italy) are presented, together with the comparison with the relevant ground truth [2]. This second task is not a trivial one: as a matter of fact, the geometrical differences (resolution and scene orientation) between the SAR image and the DEM of the area of interest should be taken into account. Furthermore, the presence of artifacts in the DEM, probably due to the particular interpolation technique used for its generation, significantly complicates the analysis.

6.1.1 Fractal analysis of the SAR image

First of all, the fractal SAR image post-processing is applied to a TerraSAR-X stripmap image of the Somma - Vesuvius volcanic complex area.
The characteristics of the starting image (Fig. 6.1) are the following: dimensions 3251x2820, resolution 3mx3m, VV polarization. As said in the previous chapter, the choice of the sliding window dimension used for the spectral estimation comes from a trade-off between the resolution of the final map, the accuracy of the fractal dimension (D) estimation and the computational complexity. In this case, being the resolution of the TerraSAR image high, the sliding window dimension is set equal to 51x51 pixel, i.e. not very small, in order to guarantee the accuracy of the estimation of D [1], [2].

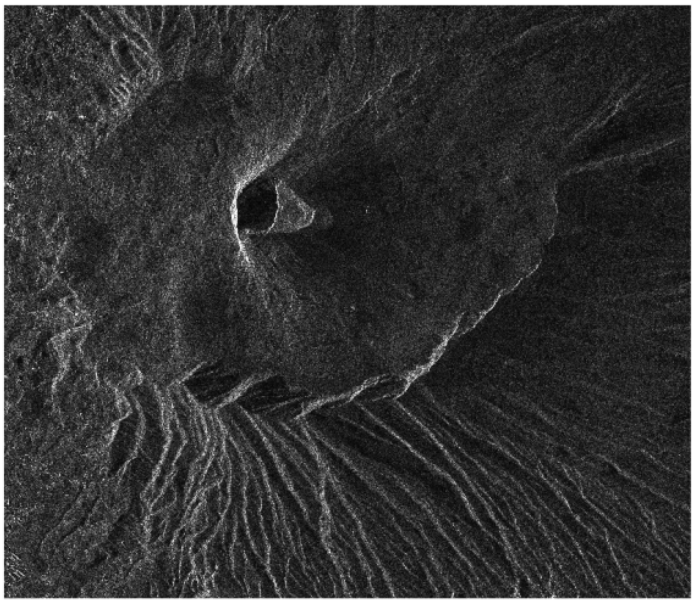

Fig. 6.1: TerraSAR-X stripmap image of the Somma-Vesuvius volcano

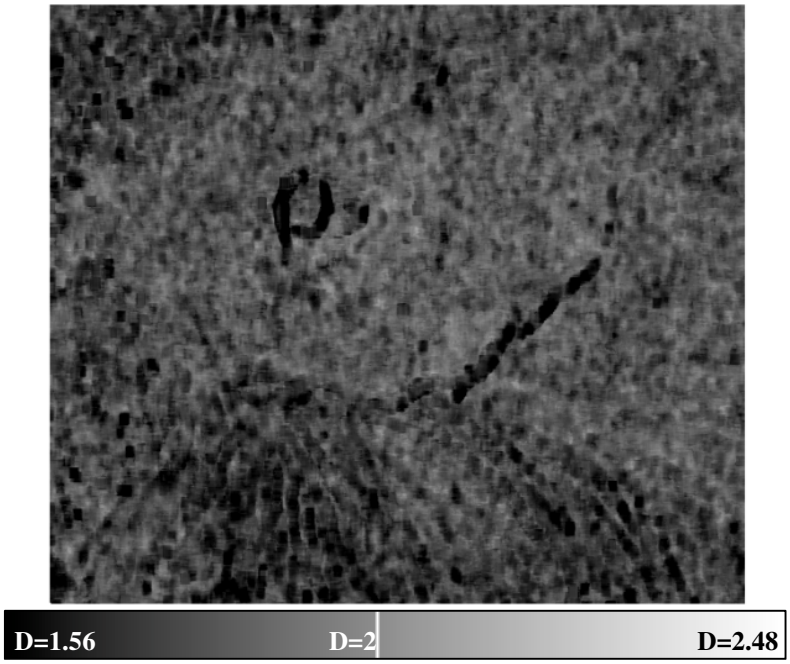

Figure 6.2: Fractal Map relevant to the SAR image in fig. 6.1

Some considerations about the obtained fractal map (Fig. 6.2) are in order. It contains the point by point estimated D values. The fractal map present a range of values of the fractal dimension equal to $1.56 < D < 2.48$ and a mean value equal to $D_{mean}= 2.2$ with a standard deviation equal to 0.08. As seen in the first section, a fractal object has a fractal dimension D: $2 < D < 3$, but natural surfaces usually show a persistent behavior that is $2 < D < 2.5$ [3]-[5]. Therefore, the estimation of D is consistent with the theoretical assumptions. Concerning the inferior limit, in some areas of the fractal map D presents values smaller than 2 (in the grey level palette of Fig. 6.2 the grey levels associated from the minimum D value to the maximum D value are reported and a white line is set in correspondence to D=2). This can be explained considering that, as we can see in Fig. 6.1, some layover effects are present in the TerraSAR image. Obviously, this phenomenon generates non-fractal features on the amplitude image, and, accordingly, in these zones the algorithm recognizes non fractal areas. Moreover, at the left upper corner of the fractal map, also some buildings, that in the SAR image appear as brilliant points, are identifiable as dark spots on the fractal map. In other cases, the areas where the fractal dimension D is less or equal to 2 could be also interpreted as the surface signature of particular tectonic processes as faulting or caldera structural formation. So, the occurrence of different fractal dimensions could be used as an indicator in order to discriminate the presence of different geodynamic processes during the natural evolution of a volcanic complex [6].

6.1.2 Comparison with the ground-truth

In order to compare the fractal map obtained from the TerraSAR image with the ground truth relevant to the scene under survey, a Digital Elevation Model (DEM) of the Somma - Vesuvius volcanic complex area is used.
The DEM, obtained through aerophotogrammetry, has a resolution of 5mx5m and is a mosaic of 4 pieces with dimensions 711x564 pixel.
The first task consists in matching the TerraSAR image and the DEM. To this end, the TerraSAR image (already cut out so that the covered geographic area is the same) must be rotated and resampled. The

rotation is deduced from the geographic coordinates, while for the sampling is used the nearest neighbor method, as other interpolation algorithms could significantly invalidate the fractal features of the image. Finally, the modified SAR image has the same resolution of the DEM. To this one, our post-processing is applied first with the same statements of the previous case (same sliding window dimensions and same filtering) in order to compare the results and then with a smaller sliding window in order to obtain a finer resolution for the fractal map.

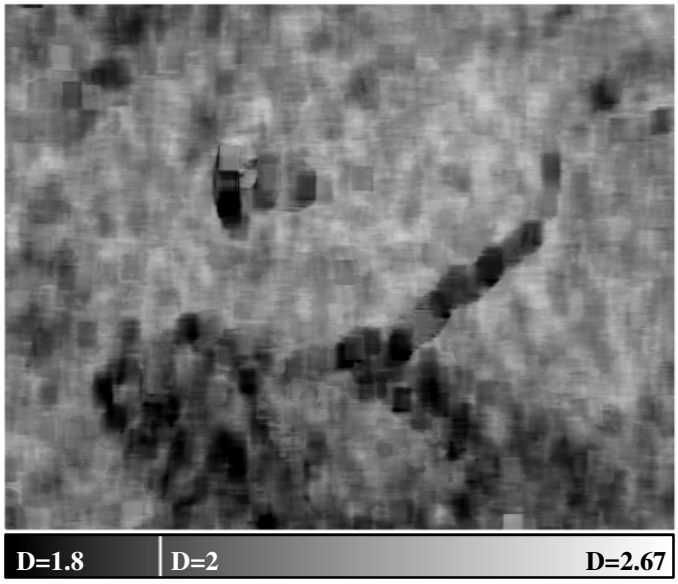

Figure 6.3: Fractal map relevant to the resampled SAR image of Fig. 6.1 obtained with a sliding window of 51x51 pixel

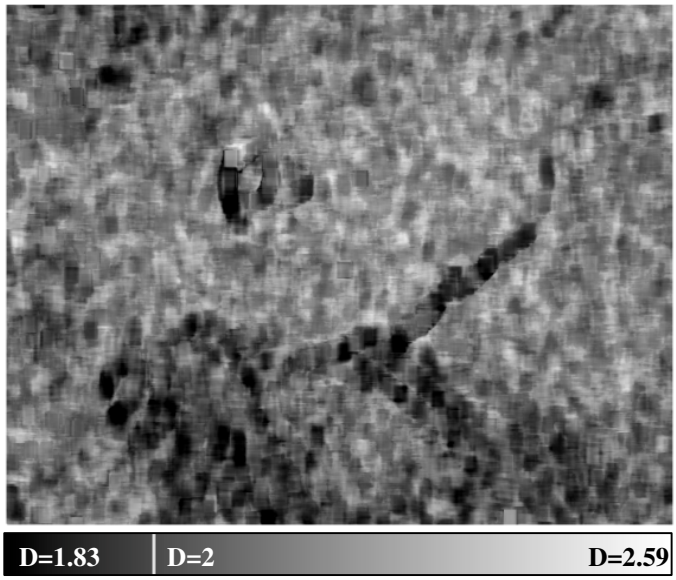

Figure 6.3: Fractal map relevant to the resampled SAR image of Fig. 6.1 obtained with a sliding window of 35x35 pixel

The fractal statistics of the map in Fig. 6.3 are: $1.8 < D < 2.67$, D_{mean}=2.3, *standard deviation* equal to 0.1. Comparing the last ones with those of the previous case, it can be deduced that a small variation of the fractal features of the SAR image is present, because of the geometrical transformation carried out. In Fig. 6.4 the fractal map obtained using a smaller sliding window (35x35 pixels) is shown. As the resolution is better and the fractal statistics remain essentially the same ($1.83 < D < 2.59$, D_{mean}=2.3, *standard deviation* equal to 0.1), this last dimension of the sliding window is chosen for the comparison with the ground truth.

The presented fractal dimension estimation algorithm is applied to the DEM, taking into account that the regression in this case is done on the spectrum of cuts of the surface (cf. Eq. 3.12). Hereafter, the obtained fractal map of the DEM is presented together with some considerations.

Fig. 6.5: DEM of the Somma-Vesuvius volcanic complex

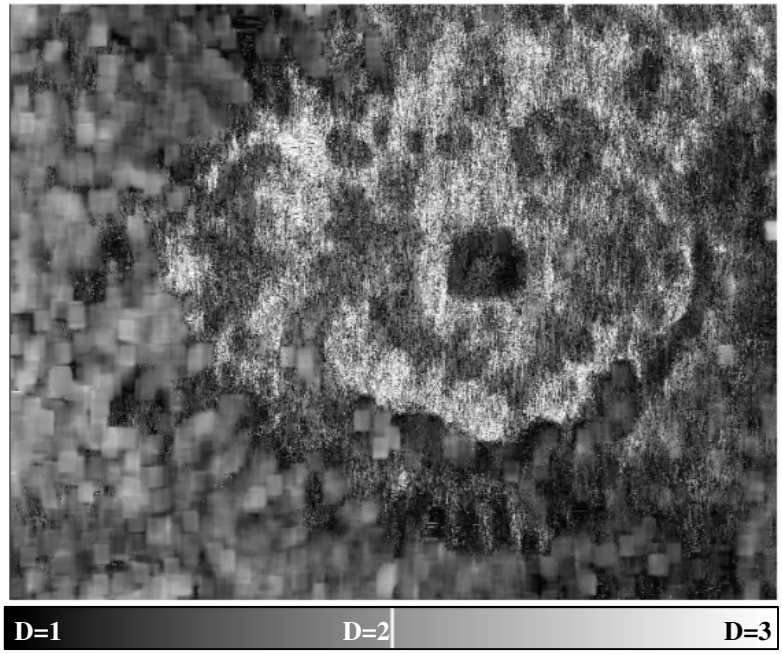

Fig. 6.6: Fractal map relevant to the previous DEM

The fractal map shown in Fig. 6.6 presents, in some points, characteristics rather different from those obtained from the SAR image and from those that it would have if the DEM were perfectly fractal. This can be explained considering that the DEM is not fractal everywhere: the interpolation used in the DEM generation process is not known, but several artifacts (perfectly flat areas) are clearly recognizable. In particular, especially in the areas of large height variations, the fractal map in Fig. 6.6 presents an anomalous dotted effect, whereas the variation of D should be smoother. Viewing the spectra relevant to those points, they appear definitely non fractals and the estimation seems to be strongly unstable. This confirms the presence of artificial features in the DEM.
The range of values of the fractal dimension of the DEM fractal map is: $-0.7 < D < 3.5$. In Fig. 6.6 is shown the relevant map with values set between: $1 < D < 3$. The mean value of the map of Fig. 6.6 is D_{mean}=1.7 and the *standard deviation* is equal to 0.4. This confirms that the non-fractal characteristics of the DEM significantly alter the retrieved fractal statistic.

6.2 Automatic detection of urban objects

The SAR image fractal processing presented in section 5.3, whenever applied to SAR images of partially rural and partially urban areas, works as automatic detector of natural rather than man-made structures. As a matter of fact, as widely discussed in Chapter 2, fractal objects hold an Hurst coefficient H included in $]0,1[$, i.e. a fractal dimension D included in $]2,3[$ ([3]-[5]); hence, by simply estimating the point by point fractal dimension of the imaged scene, objects presenting a D out of the fractal range can be identified. Hereafter the SAR image post processing is run on a TerraSAR stripmap image of an area close to L'Aquila (Abruzzo, Italy) having a resolution of 3mx3m (Fig. 6.7). The single look complex-ampiltude image captures a scene presenting partly natural elements and partly the urban area. In Fig. 6.8, the relevant fractal map is shown. The map is obtained via a sliding window of 51x51 pixels.

Fig. 6.7: TerraSAR stripmap image of L'Aquila surroundings, partly urban and partly rural

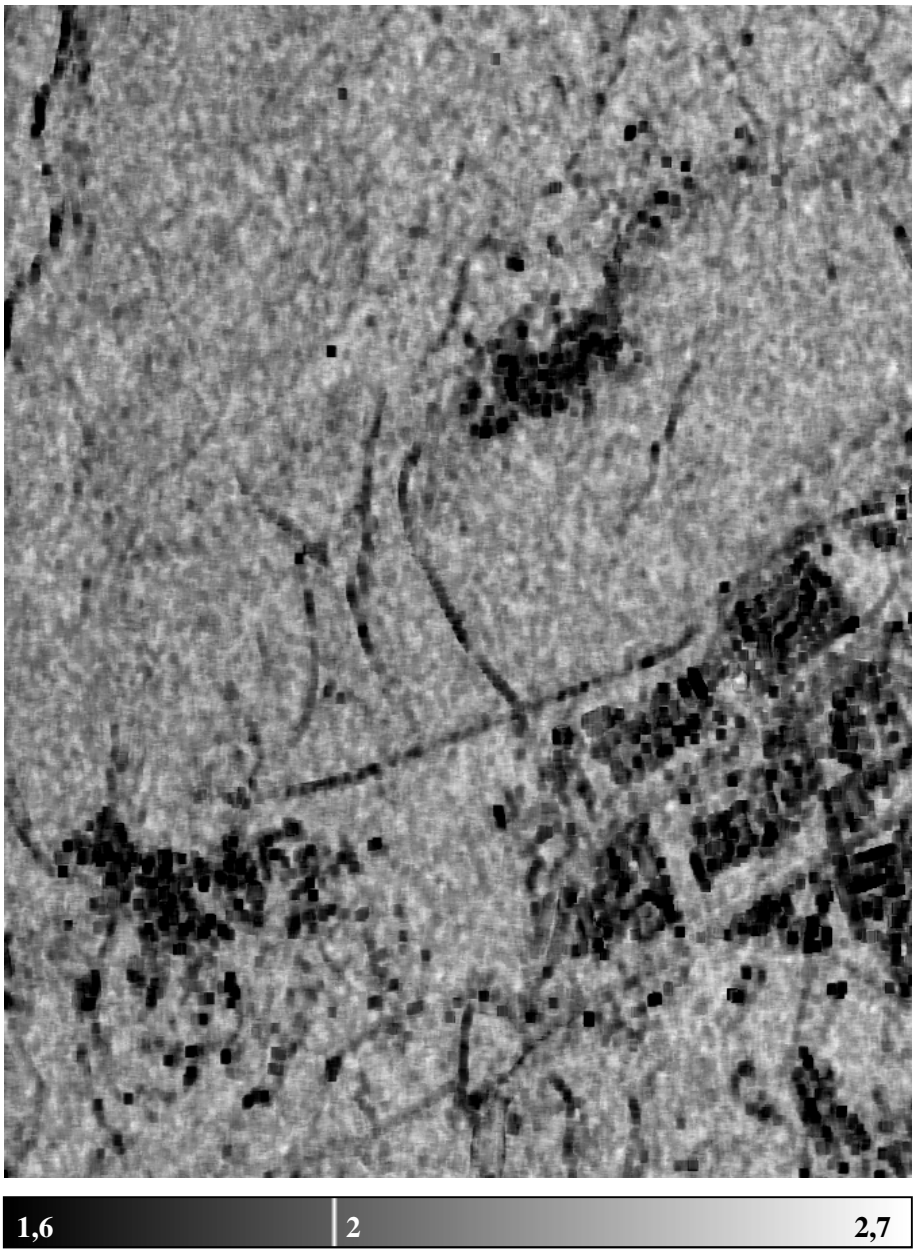

Fig. 6.8: Fractal map relevant to the previous SAR image obtained with a sliding window of 51x51 pixels.

The range of retrieved values for the fractal dimension is $1{,}6 < D < 2{,}7$, the grey-level bar placed below the figure shows the correspondence of values to the shades of grey, pointing out where the value "2", i.e. the limit between what is fractal or not, is set. It is easily visible that all the non-fractal objects as buildings or roads are present as dark features in the map and are clearly separable from the natural areas. Furthermore, it is worth noting that also some image distortion as the layover effect (cf. Section 1.2, [7]) present at the centre and on the upper left corner is detected as non fractal.
In order to exactly compare the non fractal points of the map in Fig. 6.8 with the correspondent points of the SAR image, the former have been superimposed, in red color, to the image. This gives an impressive view of the detection performance of the proposed algorithm.

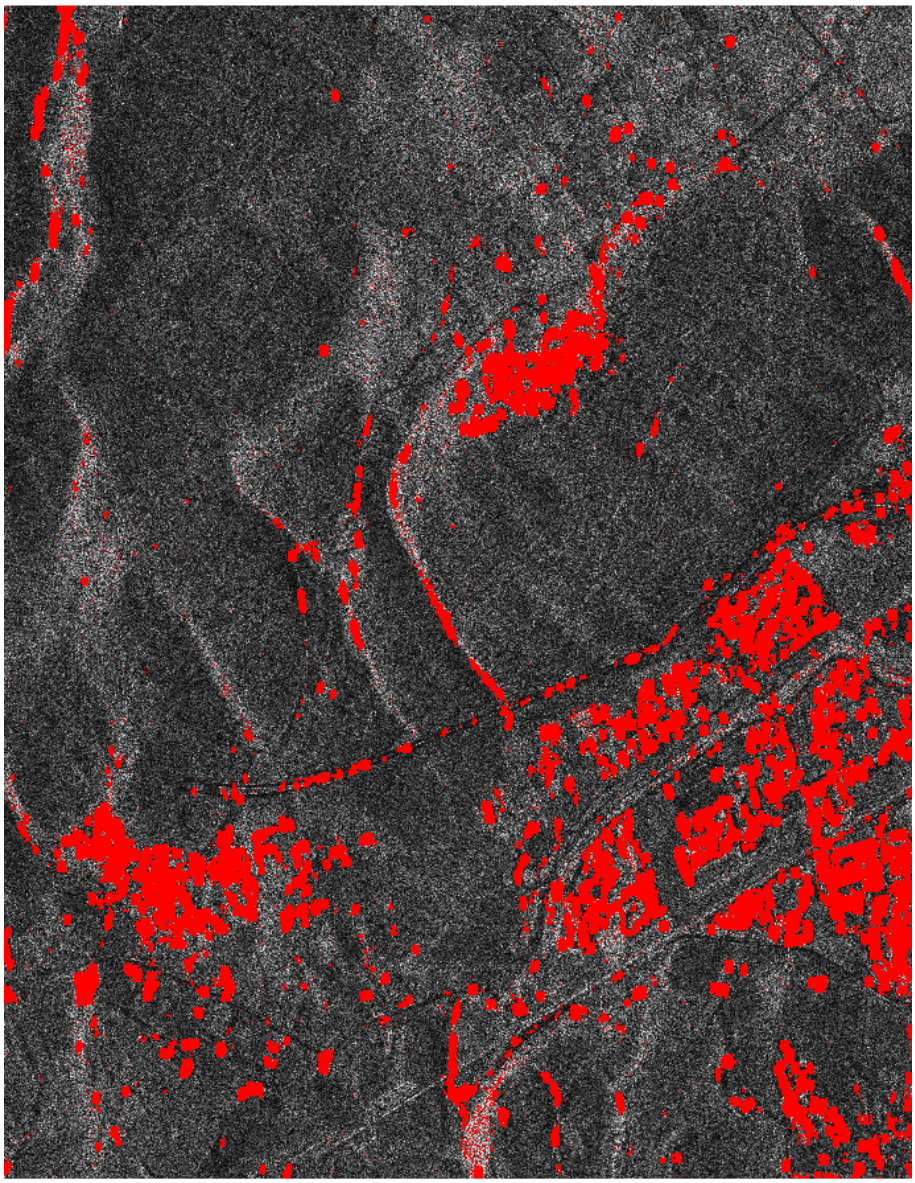

Fig. 6.9: Superimposition of non fractal points to the starting SAR image

6.3 Pre-post event fractal analysis: L'Aquila earthquake

In this section the SAR image fractal processing presented in Section 5.3 is exploited in order to perform an analysis directed to the detection of the changes occurred in urban areas owing to seismic events. In particular, the area of L'Aquila (Abruzzo, Italy) is considered and the objective is the seismic damage estimation relevant to the earthquake occurred in 2009. To perform such an analysis, a couple of COSMO-SkyMed spotlight images, acquired before and after the earthquake, have been used; the corresponding fractal maps have been generated and made comparable. The objective is the automatic detection of the areas presenting the bigger changes in pre and post-event images, via the fractal dimension estimation. The images, shown in Fig. 6.10 and 6.11, present a high resolution of 1mx1m and they have dimension of 9228 x 6411 pixels.

Fig. 6.10: COSMO-SkyMed pre-earthquake image of L'Aquila area

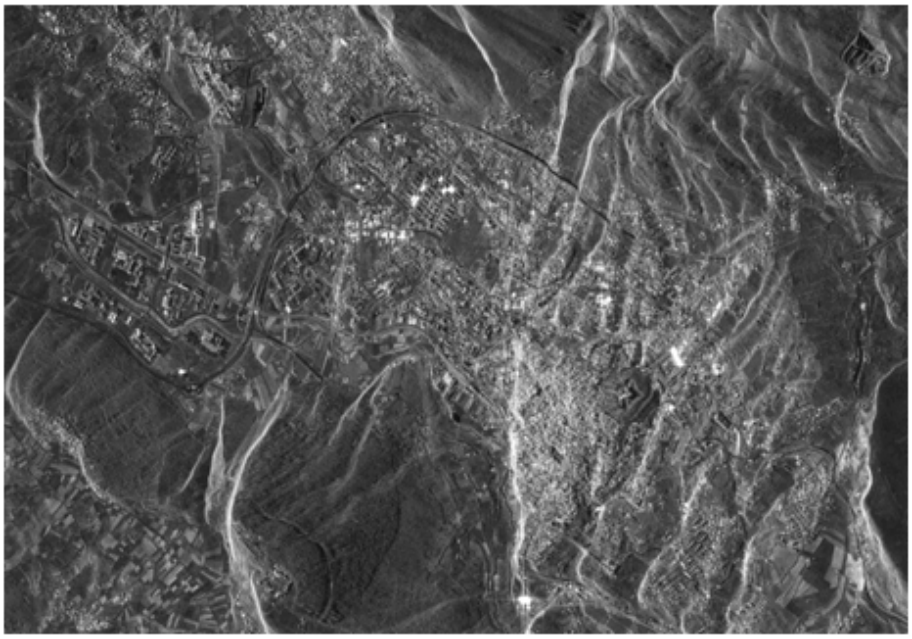

Fig. 6.11: COSMO-SkyMed post-earthquake image of L'Aquila area

In Fig. 6.12 and 6.13 the fractal dimension map relevant to the COSMO-SkyMed images in Fig. 6.10 and 6.11 are reported. For their generation a sliding window of 51x51 pixels is used, thus allowing a good accuracy of the fractal dimension estimation. Moreover, in Table 6.1, the statistics of the fractal maps are reported; these turn out, true to form, very similar for the pre-and post-event cases, being the scene observed by the sensor essentially the same except for the damaged areas.

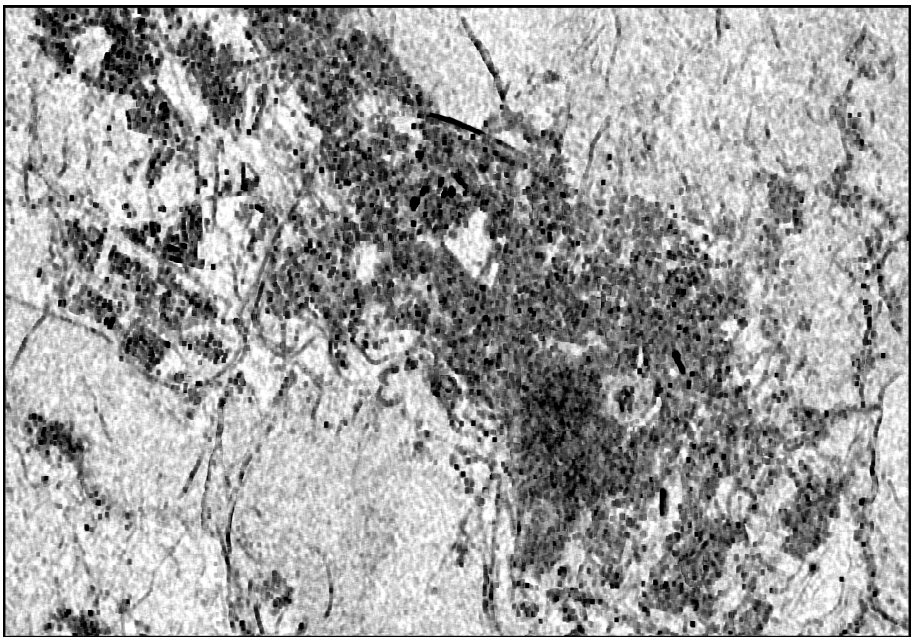

Fig. 6.12: Fractal map relevant to the SAR image in Fig. 6.7

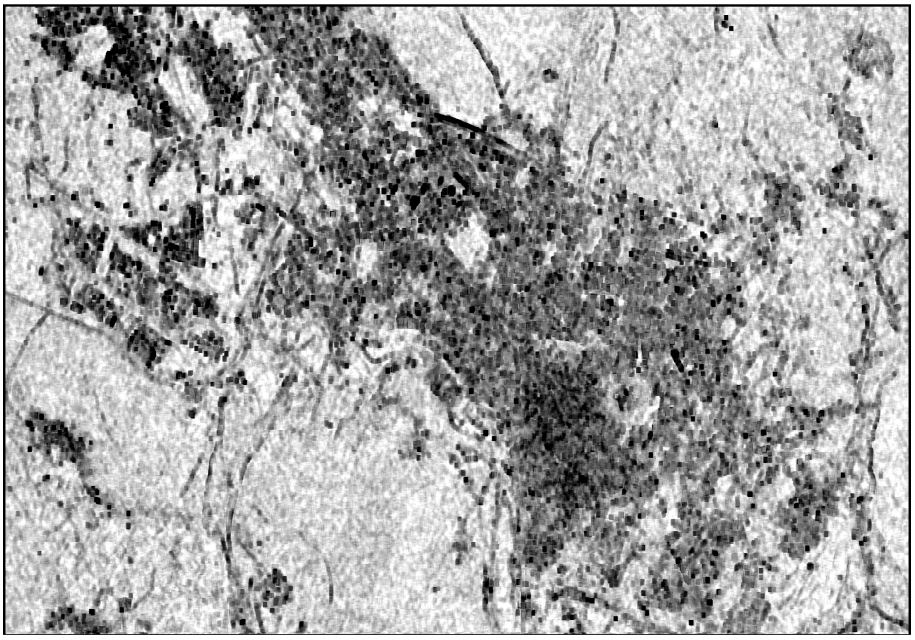

Fig. 6.13: Fractal map relevant to the SAR image in Fig. 6.8

Table 6.1
STATISTICS OF THE FRACTAL MAPS IN FIG.6.9 AND 6.10

	D min	D max	D mean	D stdev
Fig. 6.12	1.12	2.77	2.25	0.14
Fig. 6.13	1.1	2.6	2.24	0.14

In order to detect the more damaged areas, the map of the difference of the point by point fractal dimension between the pre and post SAR image is evaluated. To this aim, the two fractal maps must be firstly coregistered to be perfectly superimposable. The coregistration problem is not a trivial one as, if the coregistration is performed on the starting SAR images (as in the usual applications), it could alter the results on the fractal dimension estimation. The fractal processing seems to be very sensitive to any further elaboration performed on a single look complex SAR image. Hence, concerning geocoding, coregistration or any other projection-processing, it is more suitable to perform them on the fractal maps, i.e. after the fractal processing, rather than on the starting SAR images.
In our case the coregistration is performed selecting an ensemble of *ground control points* (GCP) from the COSMO-SkyMed single look complex images and applying the operation of coregistration on the relevant final fractal maps via the selected GCP. This is obviously done because the resolution of the final fractal maps is worse than that of the starting image (it depends on the sliding-window dimension) and so the GCPs can be pick out much more precisely starting from the image.
In Fig. 6.14 the map of the fractal dimension difference between the fractal maps in Fig. 6.12 and 6.13 (after the coregistration operation) is presented, together with the relevant statistics reported in Table 6.2.
True to form, the mean value of this difference appears very small, as we are considering the difference between fractal maps of the same geographic area, at a distance of just one month, so the biggest changes (lighter points on the map) occur in the urban zone and reveal the damaged objects.

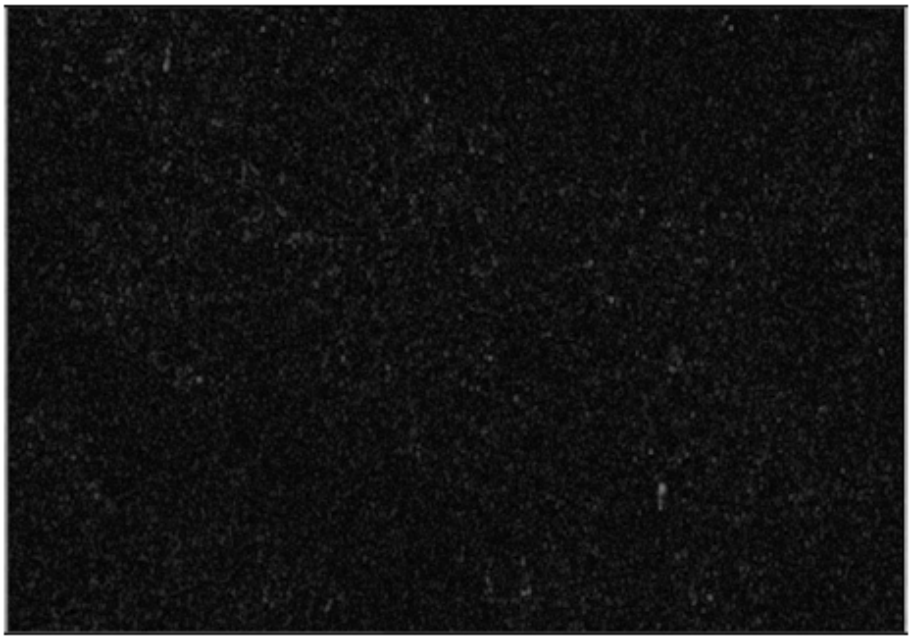

Fig. 6.14: Map of the point by point fractal dimension difference between fractal maps in Fig. 6.9 and 6.10

6.4 Preliminary results on the relative increment standard deviation map generation

In this final section a case study regarding the generation of the fractal maps of both the fractal parameters *D* and *s* [m^{1-H}] for a COSMO-SkyMed stripmap image of an area of Burkina Faso (West-Africa) is presented [8]. The map of the relative increment standard deviation *s* is generated by an algorithm based on the same rational of that used for the fractal dimension map generation. It extracts the local *s* of the imaged surface - according to the operations described in Section 5.2.2 - working on patches of the SAR image and iterating the procedure on the whole image, through a moving window. For the s estimation, first of all, a reference PSD is evaluated starting from an homogeneous area of the SAR image presenting the sliding window dimension; then, with regard to this spectrum, in each window the relative *s* estimation is performed.

In Fig. 6.16 and 6.17 the fractal maps of both the point by point fractal dimension and the relative increment standard deviation, retrieved from the SAR image shown in Fig. 6.15, are presented. The starting SAR image is a 9277x9192 pixel image with a resolution of 3mx3m.

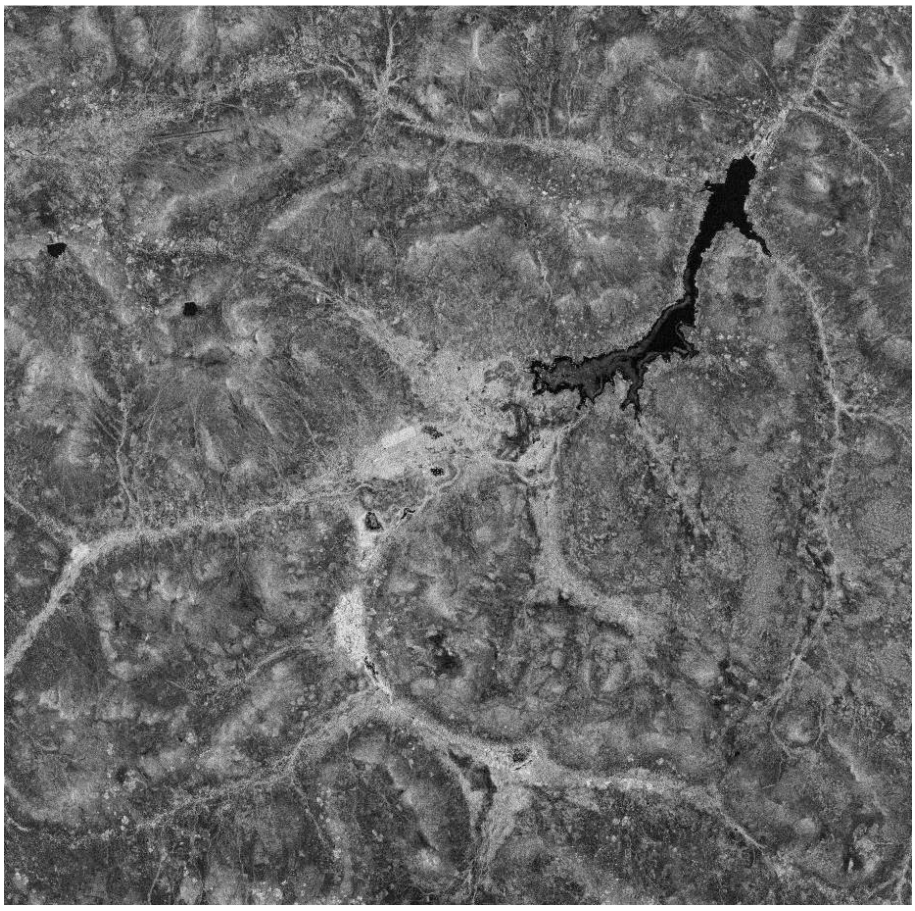

Figure 6.15: COSMO-SkyMed Stripmap image of a rural area of Burkina (Africa).

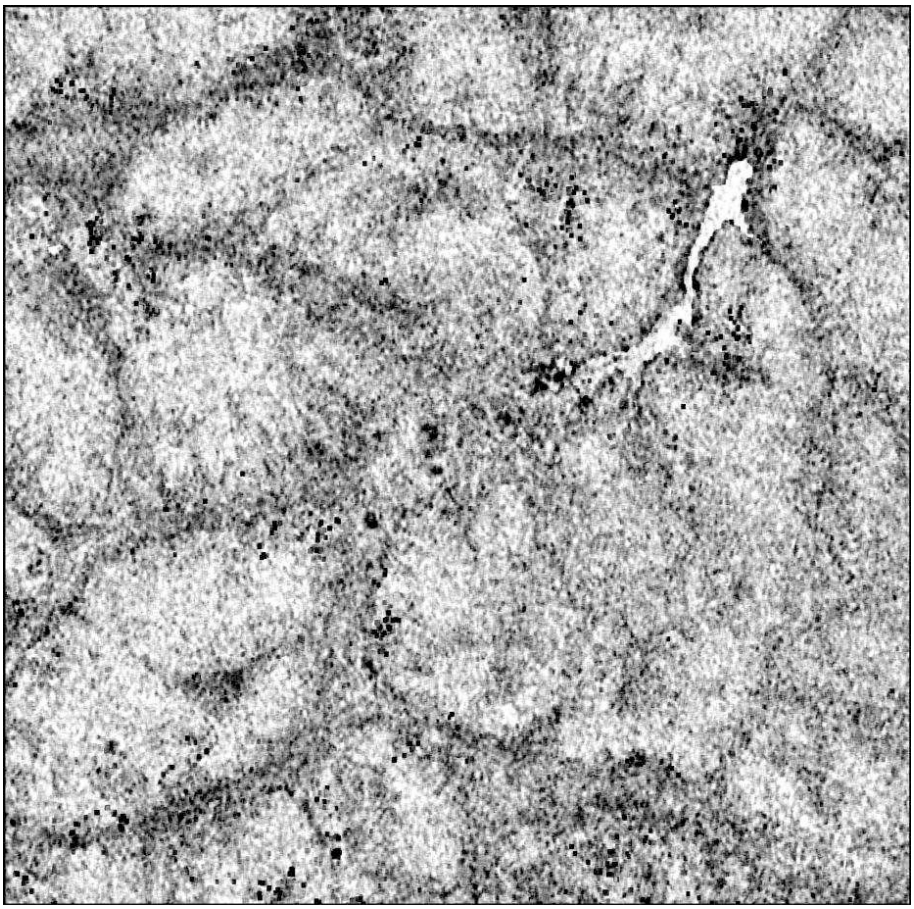

Figure 6.16: Fractal dimension (*D*) map relevant to the SAR image in Fig. 6.15

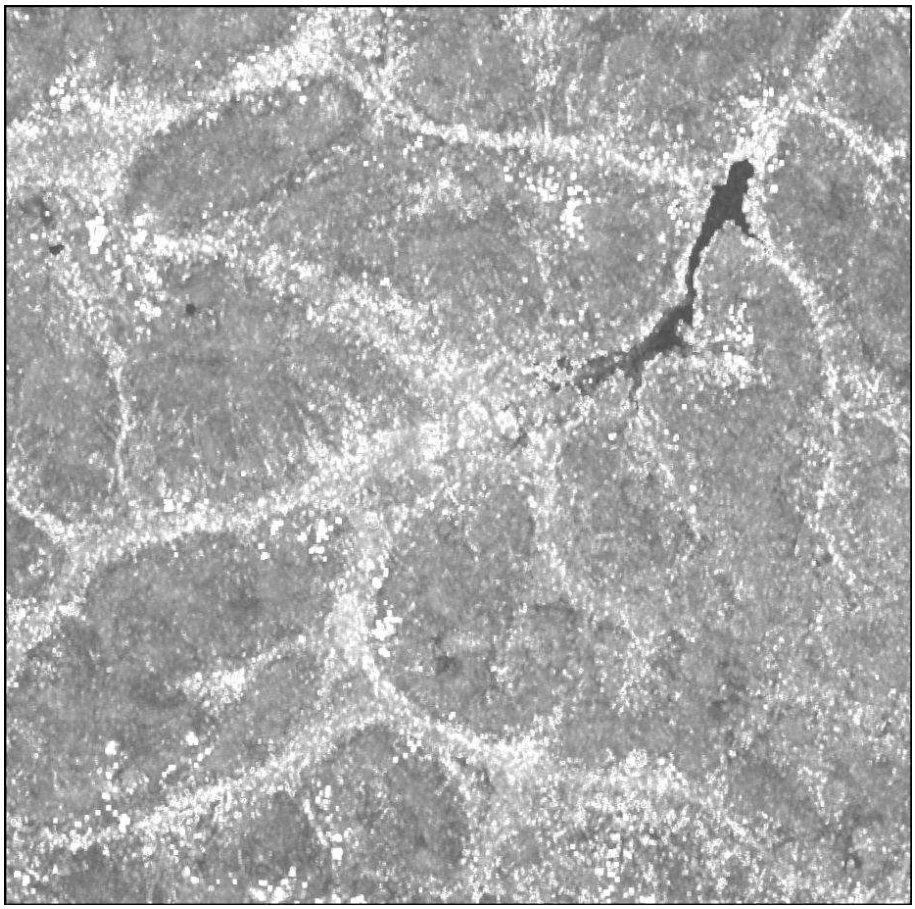

Figure 6.17. Increment standard deviation (*s*) map relevant to the SAR image in Fig. 6.15

The statistics of the fractal maps in Figures 6.16, 6.17 are given in Table 6.2

Table 6.2
STATISTICS OF THE FRACTAL MAPS IN FIG.6.16 AND 6.17

	Minimum	**Maximum**	**Mean**	**Standard Deviation**
***D* map** (Fig. 6.16)	1.32	2.49	2.20	0.07
relative *s* map [$m^{0.82-Hstim}$] (Figure 6.17)	0.38	313.12		

Concerning the fractal dimension map, it can be observed that the *D* mean is a value typical for natural surfaces.
Regarding the increment standard deviation map, there is a large variation range between minimum and maximum but so high values for the relative *s* occur only for very few points in which probably the starting SAR image presents features that alter the spectrum estimation. The reference spectrum used is represented in Figure 6.18 and presents an estimated value of *D* equal to 2.18.
It is important to note that the increment standard deviation map in Fig. 6.17 makes sense only if read together with the relevant fractal dimension map, in fact the parameter *s* has a dimension unit that depends on *H* (equivalently *D*) [9], [10]. That is why in table 6.2 the mean and the standard deviation of *s* have been omitted: each point of the *s* map has a different dimensional unit depending on the *D* value of the corresponding point in the *D* map.
As Fig. 6.16 and 6.17 show, the information content of the maps of the fractal parameters *D* and *s* is rather different. The *s* map is somehow proportional to the SAR image intensity, as a matter of fact the information on the s parameter is held in the spectral amplitude. Conversely, the fractal dimension map is completely independent on the image intensity, being *D* related to the correlation properties of the image through the spectral slope. Hence a jointly use of these different but complementary types of information is one of the most important future developments of this work.

References

[1] G. Di Martino, D. Riccio and I. Zinno, "SAR Imaging of Fractal Surfaces", IEEE Trans. Geosci. Remote Sens., in print, available on IEEE Early Access.

[2] G. Di Martino, A. Iodice, D. Riccio, G. Ruello, I. Zinno, “On the fractal nature of volcanoes morphology detected via SAR images analysis: the case of Somma – Vesuvius Volcanic Complex”, accepted for publication on the special issue of The Italian Journal of Remote Sensing, 2011.

[3] B.B. Mandelbrot, 1983, The Fractal Geometry of Nature. New York: Freeman, 1983

[4] Peitgen H.O.and Saupe D. (1988), The Science of Fractal images. Springer Verlag (pp:1 312)

[5] Yokoya N., Yamamoto K., Funakubo N. (1989) - Fractal-based Analysis and Interpolation of 3D Natural Surface Shapes and Their Application to Terrain Modeling, Computer Vision, Graphics, and Image Processing, 46: 284-302

[6] Turcotte D.L., Fractals and Chaos in Geology and Geophysics (second edition) Cambridge University Press (pp:1-385), 1997

[7] G.Franceschetti and R.Lanari; Synthetic Aperture Radar Processing, CRC PRESS, New York, 1999.

[8] D. Riccio, I. Zinno, G. Di Martino and G. Ruello, "SAR image post-processing for the estimation of fractal parameters", Proceedings SPIE 2011, Prague (Czech Republic), September 2011, accepted for publication.

[9] G. Franceschetti, D. Riccio, Scattering, *Natural Surfaces and Fractals*. Academic Press, Burlington (MA), USA, 2007

[10] Falconer K. (1990) - *Fractal Geometry*, Chichester: John Wiley & Sons.

Conclusions

In this thesis a complete direct model of the SAR imaging process for fractal surfaces has been presented. Furthermore a SAR image post-processing, based on this model's inversion, allowing the extraction of fractal parameters representing the scene observed by the sensor – starting from a single SAR image – is provided.
The proposed model, which is in turn based on sound radar, electromagnetic and geometrical models, links, in an analytical way, the SAR image of a natural surface to the parameters that quantitatively describe the surface of interest. In particular, due to the fact that a natural surface presents an inherent stochastic behavior, it has been computed in closed form, under the hypothesis of small slopes of the surface, the statistical characterization of the acquired image, that depends on the parameters used for the surface characterization. For the description of the natural scenes fractal models have been used, as they are widely recognized in literature as the best ones representing the roughness of this type of areas. Moreover, in order to deal with the scattering problem, fractal models that take into account the interaction of the electromagnetic field with a fractal surface, have been used too. Therefore the framework of the presented SAR imaging model is, for the first time, completely fractal based.
The main theoretical results presented in this thesis can be summarized as follows:

- it has been demonstrated that the reflectivity of the imaged natural scene linearly depends, in the hypothesis of small slopes, only on the partial derivative along the range direction of the two-dimensional surface;
- after adequately evaluating the range derivative process of the surface, the two-dimensional autocorrelation function of the reflectivity and of the SAR image have been computed in closed form;
- starting from the two-dimensional autocorrelation function, the Power Spectral Densities of a range and an azimuth cut of the

image have been computed in closed form; the range and azimuth PSDs show very different behaviors, analytically highlighting the intrinsic asymmetry of a SAR image: in particular, neither of them is rigorously fractal but the range one, in an appropriate range of wavenumbers, presents a power-law behavior with a slope related to the fractal dimension of the observed surface;

- performing linear regression techniques on the PSD of range cuts of the SAR image the fractal dimension D of the observed natural surface can be retrieved.

In order to validate the theoretical results a complete numerical setup has been presented as well. First of all, a complete simulation chain allowing the generation of a SAR image of a fractal surface of known parameters has been implemented. On the simulated image an algorithm performing the inversion of the theoretical model has been applied: the PSDs of range and azimuth cuts of the image have been estimated and then compared with the theoretical ones. The problem of spectral estimation of power-law spectra of short data segments of SAR images has been taken into account; hence the Capon estimator has been used as it minimizes the variance and compensates for leakage effect.

The fractal parameters estimation from single SAR images has been, then, treated. Performing linear regression techniques on the SAR image range spectrum, the fractal dimension of the imaged surface has been estimated. A large numerical setup has been provided in order to test the retrieving algorithm. Furthermore, preliminary results on the extraction of the second fractal parameter, the increment standard deviation, have been presented.

Finally, an innovative post-processing of the SAR image providing a map of the point by point fractal dimension of the scene observed by the sensor has been implemented. At first, for validation purpose, it has been applied to simulated SAR images of canonical fractal surfaces both without and with the speckle effect. Afterwards, some study cases relevant to the application of the SAR image post-processing to actual SAR images have been presented, in order to show the potentialities of such a tool.

The fractal analysis instruments - theoretical and numerical - presented in this thesis allow carrying out a wide range of applications regarding prevention and monitoring of environmental disasters,

geodynamic processes interpretation, land classification (extraction of geomorphologic features, land use etc.), rural and urban planning, and so on.

Bisogna avere il caos in sé
per partorire una stella che danzi.
Friedrich Nietzsche